1. AGENCY USE ONLY (Leave blank)	2. REPORT DATE 25 Oct 00	3. REPORT TYPE AND DATES COVERED Ph.D Dissertation 1996–2000

4. TITLE AND SUBTITLE Transient Coherent Effects in Semiconductor Three-State Systems	5. FUNDING NUMBERS

6. AUTHOR(S)

Michael E. Donovan

7. PERFORMING ORGANIZATION NAME(S) AND ADDRESS(ES) Optical Sciences Center University of Arizona Tucson, AZ 85721	8. PERFORMING ORGANIZATION REPORT NUMBER N/A

9. SPONSORING/MONITORING AGENCY NAME(S) AND ADDRESS(ES) U.S. Army	10. SPONSORING/MONITORING AGENCY REPORT NUMBER N/A

11. SUPPLEMENTARY NOTES

~~Works~~ Work performed under a research grant by ARO.

12a. DISTRIBUTION/AVAILABILITY STATEMENT General distribution **DISTRIBUTION STATEMENT A** Approved for Public Release Distribution Unlimited	12b. DISTRIBUTION CODE

13. ABSTRACT (Maximum 200 words)

The coherent response of a semiconductor three-state system to one or two intense light pulses is investigated experimentally on a 100 fs time scale. Three experiments constitute this dissertation: observation of excitonic Rabi oscillations, measurement of two-exciton coupled Stark shifting, and an attempt to observe dark states. Basic concepts of time-resolved ultrafast semiconductor spectroscopy are explained, followed by an analysis of semiconductor two- and three-state systems. Pure two- and three-state dynamics are derived from first principles, followed by the development of the appropriate semiconductor Bloch equations (SBE). Two-color pump-probe, two-color pump-pump, and pump-pump-probe techniques are explained in the context of three-state semiconductor experiments. The experimental setup is explained in detail.

20001120 005

14. SUBJECT TERMS	15. NUMBER OF PAGES 181
	16. PRICE CODE

17. SECURITY CLASSIFICATION OF REPORT UNCLAS	18. SECURITY CLASSIFICATION OF THIS PAGE UNCLAS	19. SECURITY CLASSIFICATION OF ABSTRACT UNCLAS	20. LIMITATION OF ABSTRACT None/Unlimited

TRANSIENT COHERENT EFFECTS IN SEMICONDUCTOR THREE-STATE SYSTEMS

by

Michael Edward Donovan

A Dissertation Submitted to the Faculty of the

COMMITTEE ON OPTICAL SCIENCES (GRADUATE)

In Partial Fulfillment of the Requirements

For the Degree of

DOCTOR OF PHILOSOPHY

In the Graduate College

THE UNIVERSITY OF ARIZONA

2 0 0 0

STATEMENT BY AUTHOR

This dissertation has been submitted in partial fulfillment of requirements for an advanced degree at The University of Arizona and is deposited in the University Library to be made available to borrowers under rules of the Library.

Brief quotations from this dissertation are allowable without special permission, provided that accurate acknowledgment of source is made. Requests for permission for extended quotation from or reproduction of this manuscript in whole or in part may be granted by the head of the major department or the Dean of the Graduate College when in his or her judgment the proposed use of the material is in the interests of scholarship. In all other instances, however, permission must be obtained from the author.

SIGNED: _Mich l'E Donor_

ACKNOWLEDGEMENTS

This dissertation would not have been written without the selfless contributions of many friends. I am truly amazed at how lucky I am to have been associated with so many exceptional individuals.

Formost is Axel Schülzgen, whose talents as a scientist created results from confusion. He guided me every step of the way, but his assistance in setting up the final experiments and in writing the last paper went far beyond the call of duty. Especially for his efforts in the last six months I am eternally grateful.

The last ten weeks of lab work stretched the limits of my patience and endurance. I would not have lasted without the energy, enthusiasm, and friendship of Jane Lee. It has been an honor to work with such an unselfish person.

I have also been priviliged to know and work with Kai Wundke, whose contributions to the lab were critical. Kai always made time for my questions and taught me much by his example.

I am grateful to Ronald Reagan and Mikael Gorbachev for creating the political conditions that allowed Axel, Kai, and Christine to come to the University of Arizona.

My wife Ok Kyom, my son James, and my daughter Charlene have been very supportive. Ok Kyom particularly has run the household singlehandedly the last five months (no exaggeration) and allowed me to concentrate on this work. I have a lot to make up for now.

The Optical Sciences Center has a wonderful student body, faculty, and administrative staff (nobody left out on purpose). I would like to particularly express my gratitude for various reasons, but especially for friendship, to the following people (in alphabetical order): Jason Auxier, Rolf Binder, Pierre Blanche, Kit-Iu Cheong, Claudia Ell, Monica Escher, Kyle Ferrio, Josh Haddock, Oliver Henning, Jon Herlocker, Bor-Chyuan Hwang, Ghassan Jabbour, Poul Jessen, Shibin Jiang, Bernard Kippelen, J. P. Laine, Didi Lawson, Tao Luo, Mike Morrell, Sierk Pötting, Gabriel Ramos, Christine Spiegelberg, and last but not least, Robert Upton. There are probably some others I should have included, but my memory is not what it used to be.

To my advisor, Nasser Peyghambarian, I would like to express my appreciation for being assigned to the right lab. I do not think my experience in any other work would have been as fun and educational. The really rewarding experiences don't come easy.

DEDICATION

Dedicated to Emma Scott Donovan

1898–1999

TABLE OF CONTENTS

TABLE OF CONTENTS – *Continued*

TABLE OF CONTENTS – *Continued*

TABLE OF CONTENTS – *Continued*

LIST OF FIGURES

LIST OF FIGURES – *Continued*

LIST OF FIGURES – *Continued*

ABSTRACT

The coherent response of a semiconductor three-state system to one or two intense light pulses is investigated experimentally on a 100 fs time scale. Three experiments constitute this dissertation: observation of excitonic Rabi oscillations, measurement of two-exciton coupled Stark shifting, and an attempt to observe dark states. Basic concepts of time-resolved ultrafast semiconductor spectroscopy are explained, followed by an analysis of semiconductor two- and three-state systems. Pure two- and three-state dynamics are derived from first principles, followed by the development of the appropriate semiconductor Bloch equations (SBE). Two-color pump-probe, two-color pump-pump, and pump-pump-probe techniques are explained in the context of three-state semiconductor experiments. The experimental setup is explained in detail.

Resonant two-color pump-probe measurements resulted in the first observation of multiple excitonic Rabi oscillations. The common conduction band shared by the light-hole and heavy-hole excitons of an InGaAs multiple quantum well allowed us to measure hh-exciton density (Rabi) oscillations by probing lh-exciton absorption. By studying the intensity dependence of the Rabi frequency, we showed the important role of many-body effects in renormalizing the dipole energy.

The shared conduction band also causes the lh-exciton resonance to Stark shift when the hh-exciton is Stark shifted. We measured a transient Stark shifting of both resonances due to virtual hh transitions. We observed that the ratio of the hh-exciton shift to lh-exciton shift was 2:1 at large pump-exciton detuning, as predicted from a simple three-state dressed exciton picture. For smaller detunings we saw an increase in the ratio and a redshift of the non-dipole coupled exciton state. Both of these observations are consistent with the most recent theories and experiments on excitonic Stark shifting.

For strong near-resonant pumping of both *lh*- and *hh*-exciton transitions, an intervalence-band Raman-type coherence follows from the SBE that results in a transparent eigenstate (dark state) when both pumps are equally detuned from resonance. The existence of this coherence is well-known in atomic–optical systems, but has been elusive in semiconductors. Our inconclusive experimental result is presented along with an evaluation of experimental shortcomings. In brief, the expected change is absorption was too small to see.

CHAPTER 1

COHERENT SEMICONDUCTOR SPECTROSCOPY

In 1880, not long after Maxwell wrote his famous equations (1873) and before the Bohr atom (1913), Rutherford's nuclear model of the atom (1911), Planck's quantum hypothesis (1900), and even before the first observation of atomic spectra (Balmer, 1885), H. A. Lorentz hypothesized that an electron in an atom was bound by an elastic force, and from this derived a remarkably accurate model of optical absorption and anomalous dispersion.[1] Using (1) the quantum mechanics that sprung from Plank's blackbody radiation theory, (2) an understanding that atomic electrons were bound to massive nuclei, and (3) the concept of discreet energy levels for bound particles, the next generation of physicists approached the light-matter interaction from a modern physics perspective. They derived the oscillator model that Lorentz had assumed, but they had a quantitative explanation for the oscillator strength and added the concept of the inversion. In the pre-laser era, the inversion, or probability of an atom being excited minus the probability of remaining in the ground state, was always reasonably approximated as -1, which explains the success of the Lorentz model. When driven by high intensity laser light, however, the modern atomic oscillator exhibits a nonlinear response with some amazing electron dynamics. Whether the response corresponds to absorptive or dispersive effects, the response is at least theoretically measureable in the transmitted light.

So long as a collection of atoms (e.g., a gas or a beam) maintains a definite phase relationship, or coherence, the net response of the collection mimics the single atom response. This is what is called the coherent regime. In reality, the coherence decays at a characteristic time called T_2 that is typically on the order of tens to hundreds

---

[1]The date of 1880 comes from reference [1, p. 30], while reference [2, p. 32] places the atomic oscillator hypothesis circa 1900.

of nanoseconds for atomic gasses. Nonlinear effects that can only be seen so long as atomic coherence is maintained have come to be known as coherent transients. The genesis of the study of coherent transients was actually in the spin vector formalism of F. Bloch whose Bloch equations were developed for magnetic resonance. Effects that were first seen in magnetic resonance were later seen in optically driven atomic systems whose dynamics were essentially two-state. These include Rabi oscillations (or optical nutation), free-induction decay, self-induced transparency, and photon echoes. Transient coherent effects can also occur with off-resonant excitation so that only virtual transitions are induced, and the dynamic optical Stark effect is the prototype for this interaction.

The successful demonstration of coherent transients in atomic two-state systems (mid 1960s to mid 1970s) was soon followed up by the theoretical and experimental study of three-state systems (mid 1970s to date). Most interest in three-state systems has focused on the destructive interference of two probability amplitudes that leads to the cancellation of absorption. This creation of "dark states" has resulted in coherent population trapping, electromagnetically induced transparency, amplification without inversion, and refractive index enhancement.

This dissertation presents an experimental study of transient coherent effects not in atoms but in semiconductors. Specifically, three semiconductor phenomena are studied: excitonic optical Rabi oscillations, coupled dynamic Stark shifting, and the creation of dark states. This opening chapter explains some of the basics concepts of ultrafast spectroscopy, explains why two- and three-state semiconductor models are useful, develops the concept of the exciton, and introduces the experiments.

1.1 Ultrafast time-resolved spectroscopy

The most serious obstacle to measuring transient coherent effects in semiconductors is the rapid decay of the coherence. At room temperature the decay is likely too fast for any known measurement technique. To reduce the dephasing rate, all coherent semiconductor experiments are done at low temperatures, usually 4.2 K (liquid He) or 1.8 K (superfluid liquid He). Even so the dephasing rate is on the order of 100's

of femtoseconds to a few picoseconds.

No existing electronic detectors can resolve changes that occur faster than the decay of the semiconductor coherence. In order to measure on the ultrafast (sub-picosecond) time scale, scientists use the overlap of sub-picosecond light pulses to substitute for direct optoelectronic detection. In the Rabi oscillation and coupled Stark shifting experiments we used a temporally short, low intensity "probe" pulse to time-gate the interaction of a temporally longer, strong "pump" pulse. By changing the relative delay, we time-resolved the nonlinear light-matter interaction by observing how pump-induced material changes affected probe transmission. For the dark states interaction, both pulses were high intensity and participated equally in the interaction. The simultaneous presence of both pulses was to create a coherence between two otherwise uncoupled states, the light-hole and heavy-hole exciton states. As mentioned above, coherent effects decay at a characteristic time T_2, so changing the pulse overlap helps one to distinguish coherent effects from more persistent nonlinearities. Furthermore, in a two-pump interaction the strength of the coupling between the two transitions varies with pulse overlap, which should be observable in the response.

The Fourier transform (time-bandwidth) relationship between the pulse duration and the spectrum of a light pulse is of central importance in forming and using ultrashort pulses. For ultrashort pulse production, one needs a broad spectrum of light correctly assembled for a short pulse. The rule for correctly assembly is the result of the Fourier transform relationship; the Fourier components must have the same phase at some point in space and time.

The time-bandwidth relationship also presents challenges in creating the desired light-semiconductor interaction. We excite two semiconductor resonances split by between 9.4 nm and 18.5 nm, depending on the sample. To uniquely excite a single resonance with a single pulse, the bandwidth is clearly limited (see Figure 1.1). Let us, for example, limit the pulse spectral width to $\Delta\lambda = 9$ nm. Assuming a Gaussian pulse shape and a mean wavelength of 830 nm, Fourier theory sets a minimum pulse duration of $\tau_p \geq 0.44/\Delta\nu_p \approx 0.44\lambda^2/(c\Delta\lambda) = 110$ fs. We have included pulse

shapers in our experiment so that we can vary the spectral width, and hence the pulse duration. Incidentally, the Fourier transform relationship can alternatively be considered as a form of the energy-time uncertainty relation $\Delta(\hbar\omega_p)\tau_p \geq \hbar/2$ [3, pp. 133–134]
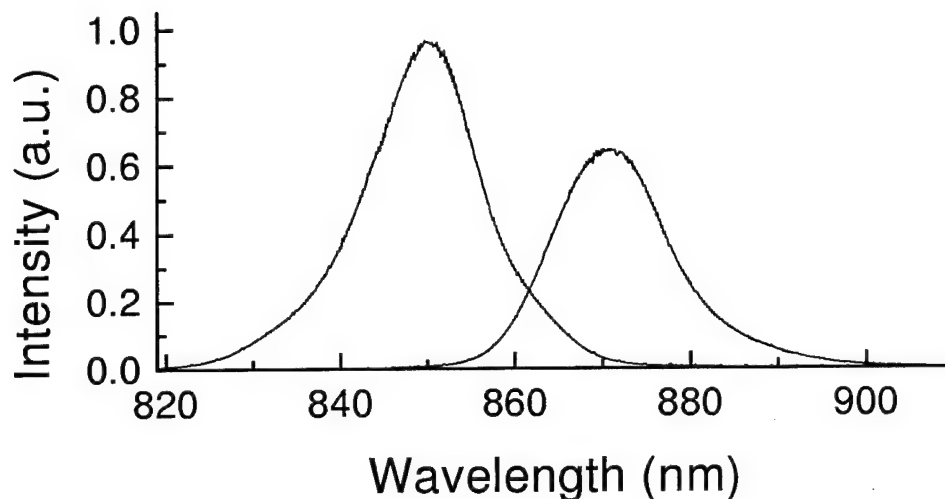
Figure 1.1: The spectra of two pulses separated by 20.8 nm (34.8 meV), which is somewhat more than the splitting of the two resonances in any of our samples. Neither pulse has gone through a pulse shaper; they are bandwidth limited at near 75 fs in duration (FWHM). To be useful for more closely separated resonances, the spectra would need to be narrowed so that they would not overlap as much.

1.2   Two- and three-state semiconductors

For semiconductors, the two- and three-state models suffer some real limitations. Bound electrons exhibit discreet energy levels, which is why atomic vapors exhibit spectral lines. In a (dilute) vapor, the atoms are widely enough separated on average that the spectrum of the whole is nearly the same as the spectrum or the individual atom.[2] In condensed matter, like the semiconductor, the energy levels become energy bands, actually discreet but very close levels that form a quasi-continuum.[3]

---

[2]There is actually some broadening of the spectral lines due to the Doppler effect and collisions.

[3]The formation of energy bands is a standard topic in all basic texts on condensed matter physics. Elementary discussions concerning semiconductors are found in References [4, pp.23–36], and [5, pp. 4–48]. More advances approaches concerning solids are found in Reference [6, pp. 131–210].

Every energy band has a number of orbital states equal to the number of elementary unit cells in the crystal, which we can estimate by Avagadro's number 6×10^{23} [5, p. 28].

While we appear to be incredibly far from a two- or three-state model, the discreet momentum carried by photons improves the situation substantially. Since band energy varies with the Bloch wave vector $\mathbf{k}$ (see Figure 1.2), conservation of momentum limits light induced transitions to what are called "vertical transitions," meaning the Bloch wave vector changes by a negligable amount.[4] If we neglect the Coulomb interaction between carriers (electrons and holes), transitions induced in two energetically isolated bands (the so-called two-band approximation) become a collection of two-level transitions [7, p. 74].
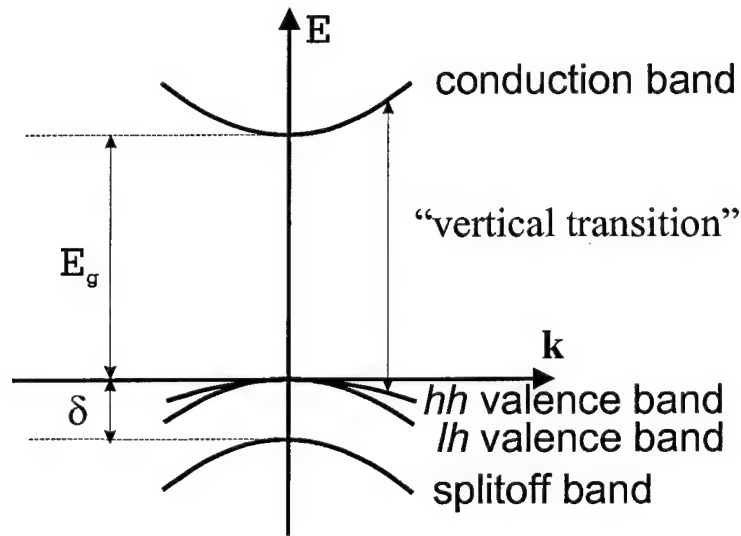
Figure 1.2: A representation of a so-called "vertical transition" induced by light. Since light carries negligable momentum, the electron will remain near the same $\mathbf{k}$ after a transition. This limits the states accessible in the optical interaction. The bandstucture shown here is for a bulk zinc-blende structure, such as GaAs. In low temperature bulk GaAs the bandgap energy, labeled E_g, is 1.52 eV , and the spin-orbit splitoff band is $\delta = 0.341$eV below the light hole and heavy hole valence bands at the Γ-point ($\mathbf{k} = 0$)[4, p. 171–172].

---

[4]An 800 nm wavelength photon has a momentum amplitude of $|\mathbf{p}| = \hbar|\mathbf{k}| = 8 \times 10^{-28}$ kg·m/s, while the first Brillouin zone extends to about $\hbar|\mathbf{k}| \approx \hbar\pi/a \approx 3 \times 10^{-24}$ kg·m/s, assuming a lattice constant, a, of 1 Å. For this reason the photon momentum is often neglected in interactions between light and solids.

1.3   Excitons

In an accurate semiconductor model, one must include the Coulomb interaction between carriers, and the two-level transitions become coupled. Furthermore, the Coulomb interaction creates discreet (Wannier) excitons which are mathematically similar to hydrogen atoms. The attractive force between electrons and holes results in discreet resonances that lie below the energy required to transition between two bands (see Figure 1.3). These are our experimental (quasi) two-state systems with additional Coulomb interaction features caused by the presence of many excitons.
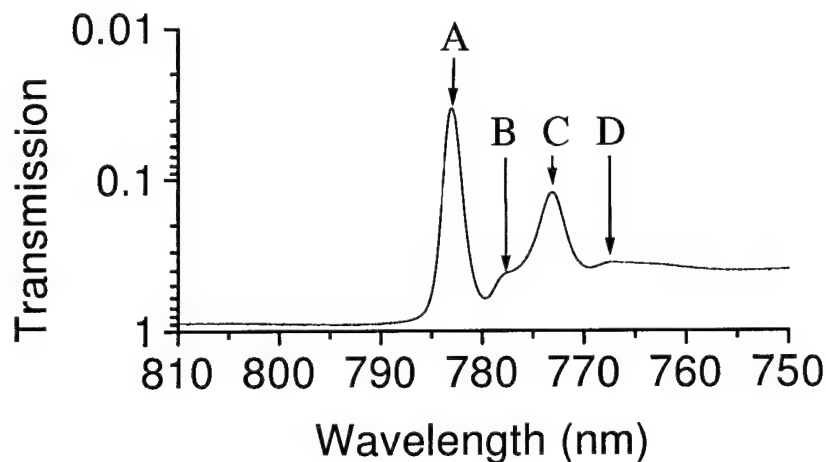
Figure 1.3: Linear spectrum of a GaAs multiple quantum well. Transmission is plotted on an inverted log scale which approximately gives the absorption spectrum. On the left, at low energies, the sample is nearly transparent. The heavy hole exciton, labeled "A," is below the bandgap energy "B" by the binding energy of the exciton. Beyond "B" is a continuum of absorption resulting from hh band to conduction band transitions. "C" and "D" are the light hole exciton and the onset of lh band to conduction band transitions. Unlike the bandstructure of Figure 1.2, the lh and hh valence bands are split in a quantum well.

Two two-state systems that share a common ground state are collectively called a three-state "V" system (see Figure 1.4). In semiconductors with a "p-like" valence band and an "s-like" conduction band[5] we can create such a system. The semiconductor considerations are the same as apply to the two-state discussion above.

---

[5]The "s" and "p" refer to $l = 0$ and $l = 1$ orbitals in isolated atoms.
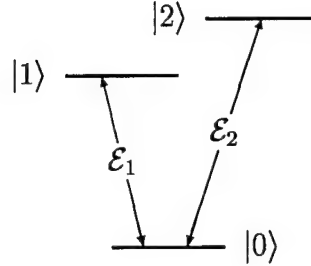
Figure 1.4: A schematic representation of a "V" system showing the energy levels of the states and the fields coupling the states. In a structure like the multiple quantum well of Figure 1.3, the ground state can be considered to be the unexcited state, with the two excited states being the *lh* and *hh* excitons. We are ignoring the continuum states that accompany each exciton transition.

We now take a simple approach to the formation of Wannier excitions adopted from Reference [4, pp. 138–144]. This will be shown in Chapter 2 to be equivalent to a more rigorous many-body approach in the low-excitation limit. We start by examining the energy eigenvalues of a single electron-hole pair. Since we so not consider interaction between excitons, we are assuming that the light field does not excite too great a density of excitons. The time independent Schrödinger equation for an electron at $\mathbf{r}_e$ and a hole at $\mathbf{r}_h$, interacting through the Coulomb potential $V^C(\mathbf{r}_e - \mathbf{r}_h) = V^C(\mathbf{r})$ is

$$\left(-\frac{\hbar^2}{2m_e}\nabla_e^2 - \frac{\hbar^2}{2m_h}\nabla_h^2 + V^C(\mathbf{r}) \right) \Phi(\mathbf{r}_e, \mathbf{r}_h) = \mathsf{E}\Phi(\mathbf{r}_e, \mathbf{r}_h). \tag{1.1}$$

The masses m_e and m_h are effective masses that derive from the periodic potential of the crystal. We take them to be constants (the effective mass approximation) which limits us to transitions near the bandgap energy of a direct gap semiconductor.[6] We look for wavefuntions $\Phi(\mathbf{r}_e, \mathbf{r}_h)$ that can be written as a linear superposition of the

---

[6]The effective mass approximation assumes parabolic energy bands, which corresponds to keeping the lowest order dispersive term in a Taylor series expansion at a local extremum in the band structure. Away from the extremum the approximation breaks down [4, pp. 34–36]. Phonon assistance must be added for indirect transitions.

single particle Bloch wavefunctions,[7]

$$\Phi(\mathbf{r}_e, \mathbf{r}_h) = \sum_{\mathbf{k}_e, \mathbf{k}_h} \tilde{\Psi}(\mathbf{k}_e, \mathbf{k}_h) \left[e^{i\mathbf{k}_e \cdot \mathbf{r}_e} u_{\nu_e \mathbf{k}_e}(\mathbf{r}_e) \right] \left[e^{i\mathbf{k}_h \cdot \mathbf{r}_h} u_{\nu_h \mathbf{k}_h}(\mathbf{r}_h) \right], \qquad (1.2)$$

using $\tilde{\Psi}(\mathbf{k}_e, \mathbf{k}_h)$ as the expansion coefficients. We will assume that the atomic character of the Bloch wavefunctions, represented by $u_{\nu_i \mathbf{k}_i}(\mathbf{r_i})$ with $i = e, h$, is well localized compared to the exciton wavefunction. With this assumption we can ignore the dispersions of $u_{\nu_i \mathbf{k}_i}(\mathbf{r_i})$ and take their values at $\mathbf{k}_i = 0$. Most II-VI, III-V, and column IV semiconductors meet this condition, which is the condition for Wannier excitons [4, p.137]. We are therefore neglecting excitons with a Bohr radius on the order of the single particle atomic wavefunctions; these Frenkel excitons are associated with wide gap semiconductors and insulators and with some organic materials [4, p. 137]. For Wannier excitons, we can now write the wavefunction as

$$\Phi(\mathbf{r}_e, \mathbf{r}_h) \approx u_{\nu_e 0}(\mathbf{r}_e) u_{\nu_h 0}(\mathbf{r}_h) \Psi(\mathbf{r}_e, \mathbf{r}_h) \qquad (1.3)$$

by using an exciton envelope function

$$\Psi(\mathbf{r}_e, \mathbf{r}_h) = \sum_{\mathbf{k}_e, \mathbf{k}_h} \tilde{\Psi}(\mathbf{k}_e, \mathbf{k}_h) e^{i\mathbf{k}_e \cdot \mathbf{r}_e} e^{i\mathbf{k}_h \cdot \mathbf{r}_h}. \qquad (1.4)$$

Now, the variation on the scale of the lattice constant is undoubtedly large and complicated, but we are interested in the electron-hole pair energy on a larger scale, the scale of the exciton envelope function. In the same way we average over atomic scale variations in the classical theory of electromagnetism in matter, we will average over the atomic functions $u_{\nu_i 0}(\mathbf{r}_i)$ on a scale large compared to their own variations yet small compared to the relative electron-hole coordinate. Replacing $u_{\nu_i 0}(\mathbf{r}_i)$ by its average $\frac{1}{V} \int_V d^3 r \, u_{\nu_i 0}(\mathbf{r}_i) \equiv u_{\nu_i 0}$, we can transform to center-of-mass coordinates

---

[7]Bloch proved that the single particle wavefunction in an infinite periodic lattice has the form $\phi_{\nu\mathbf{k}}(\mathbf{r}) = e^{i\mathbf{k}\cdot\mathbf{r}} u_{\nu\mathbf{k}}(\mathbf{r})$ (band index ν and wavevector $\mathbf{k}$) [6, pp.133–135].

and separate variables.

$$\left(-\frac{\hbar^2}{2M}\nabla_R^2 - \frac{\hbar^2}{2m_r}\nabla_r^2 + V^C(\mathbf{r})\right)\Phi(\mathbf{R},\mathbf{r}) = \mathsf{E}\Phi(\mathbf{R},\mathbf{r}) \tag{1.5}$$

$$\left(-\frac{\hbar^2}{2M}\nabla_R^2 - \frac{\hbar^2}{2m_r}\nabla_r^2 + V^C(\mathbf{r})\right)u_{\nu_e 0}u_{\nu_h 0}\Psi(\mathbf{R},\mathbf{r}) = \mathsf{E}u_{\nu_e 0}u_{\nu_h 0}\Psi(\mathbf{R},\mathbf{r}) \tag{1.6}$$

$$-\frac{\hbar^2}{2M}\nabla_R^2\Xi_{\mathbf{K}_c}(\mathbf{R}) = \mathsf{E}_{\mathbf{K}_c}\Xi_{\mathbf{K}_c}(\mathbf{R}) \tag{1.7}$$

$$\left(-\frac{\hbar^2}{2m_r}\nabla_r^2 + V^C(\mathbf{r})\right)\psi_n(\mathbf{r}) = \mathsf{E}_n\psi_n(\mathbf{r}). \tag{1.8}$$

In these equations, we have made the standard center-of-mass transformation: $\mathbf{R}$ is the center-of-mass coordinate, $\mathbf{r}$ is the distance between the electron and hole, M is the sum of the electron and hole masses, m_r is the reduced mass, and the total energy E is the sum of the center-of-mass energy $\mathsf{E}_{\mathbf{K}_c}$ and the relative coordinate energy E_n. The total wavefunction is the product $\Phi(\mathbf{R},\mathbf{r}) = u_{\nu_e 0}u_{\nu_h 0}\Psi(\mathbf{R},\mathbf{r}) = u_{\nu_e 0}u_{\nu_h 0}\Xi_{\mathbf{K}_c}(\mathbf{R})\psi_n(\mathbf{r})$.

The center of mass equation (1.7) gives us travelling wave solutions for the exciton center of mass that are similar to a free electron of mass M,

$$\Xi_{\mathbf{K}_c}(\mathbf{R}) = e^{i\mathbf{K}_c\cdot\mathbf{R}}, \tag{1.9}$$

with the center of mass wave number given by $\mathbf{K}_c = \sqrt{2M\mathsf{E}_{\mathbf{K}_c}/\hbar^2}$. Equation 1.8 is called the Wannier equation; it is identical in form to the nonrelativistic time-independent Schrödinger equation for a hydrogen atom. This means that the eigenenergies E_n of the exciton are those of the hydrogen atom, with a Rydberg energy and a background dielectric constant (ϵ_b/ϵ_0) appropriate to the semiconductor. When we excite transitions between the ground state and an exciton state, we see that the resonance is below the bandgap energy E_g by the (absolute value of the) energy of the exciton state. For the 2-D exciton

$$\mathsf{E}_g^{(2d)} + \mathsf{E}_n = \mathsf{E}_g^{(2d)} - \frac{\mathsf{E}_B}{(n-\frac{1}{2})^2}, \tag{1.10}$$

where the exciton Rydberg energy is given by [4, p.141]

$$\mathsf{E}_B = \left(\frac{1}{4\pi\epsilon_b}\right)^2\frac{m_r e^4}{2\hbar^2}. \tag{1.11}$$

A near-resonant low-intensity light field can create transitions to these bound exciton states. In an exciton state an electron-hole pair is bound together like a hydrogen atom. Since the photon has negligable momentum, the center-of-mass energy does not broaden the hydrogenic resonance to a band; conservation of momentum demands $\mathbf{K}_c \approx 0$. The absorption of light is governed by selection rules and matrix elements that arise from the interaction Hamiltonian, which will be the focus of much of this work.

1.4 Rabi oscillations, coupled Stark shifting, and dark states

The three experiments presented in this dissertation are transient coherent effects—transient meaning that they disappear with the decay of the material coherence or earlier. In the context of this work, Rabi oscillations are essentially two-state phenomena that were measured using a three-state system, coupled Stark shifting is a single pump three-state phenomenon, and dark states arise from a double-pumped three-state system.

When a two-state quantum system is subject to resonant sinusoidal external forces, the probability of occupying a particular state varies in time as $\sin^2(\Omega_R t/2)$ at an angular frequency proportional to the interaction energy. These oscillations are often called Rabi oscillations after I. I. Rabi who treated the problem both theoretically and experimentally in the context of magnetic resonance [8, 9]. Quasimonochromatic light can provide the resonant sinusoidal forces to drive electrons between quantum states in an ensemble of atoms, or in our case a semiconductor. Ω_R is called the Rabi frequency, and for electric dipole interactions is proportional to the electric field amplitude and the dipole matrix element. Because of fast dephasing and many-body effects, Rabi oscillations have been much more difficult to measure in condensed matter as compared to atomic systems.

Stark shifting results from a change in the eigenenergies of a two-level system due to an optical electric dipole interaction. The observable result is a shift in the optical absorption resonance (ω_{12}) that depends on the pump detuning Δ and the Rabi frequency: $\omega'_{12} = \omega_{12} + \sqrt{\Delta^2 + \Omega_R^2} - \Delta$ [7, p. 28]. For an ideal two-state

system, the energy levels shift away from each other by an equal amount. If a third state shares one of the energy levels, its resonance energy too will be shifted, and this is the basis of coupled Stark shifting. In the case of the semiconductor, many-body effects alter the response, and it is a prime goal of semiconductor theory to predict and explain those alterations.

The "dark state" is the name given to a particular dressed eigenstate of a three-state system which does not interact with an electromagnetic field.[8] It can arise with the simultaneous excitation of two energy transitions that share a common level as in Figure 1.4. The basis of the non-interaction with light is the destructive interference of the probability amplitudes associated with the original unexcited states. As with any interference effect, there must be a degree of coherence between the transitions to observe the interference. In the case of the dressed three-state system, this coherence is induced by so-called Raman-type or two-photon transitions between the two originally uncoupled states or, in a semiclassical picture, by the beating of the two light fields [12].

Dark states are distinguished by several effects that involve a decrease in light absorption: coherent trapping [12, 13, 14], electromagnetically induced transparency [15], lasing without inversion [16, 17], and refractive index enhancement via quantum coherence [18], to name the most common. These effects can be derived in a unified treatment, with the differences between effects due only to the initial conditions [10, pp. 241–244].

1.5 Notational conventions

We will use the following conventions in this dissertation:

---

[8]The theory of this effect is developed in Chapter 3. A coherent review (pardon the pun) of the phenomenon associated with the dark state is given in Reference [10, Chapter 7]. An interesting perspective considering the fields to be dressed by the atom is presented in Reference [11] along with a thorough discussion of other references.

electric field envelope notation

electric field	$\mathbf{E}(\mathbf{r},t) = \hat{\mathbf{e}}\mathcal{E}(\mathbf{r},t)e^{i[\mathbf{k}\cdot\mathbf{r}-\omega t]} + c.c.$
field polarization	$\hat{\mathbf{e}}$
right circular polarization	$\hat{\sigma}_- = \frac{1}{\sqrt{2}}\left[\hat{\mathbf{x}} - i\hat{\mathbf{y}}\right]$
left circular polarization	$\hat{\sigma}_+ = \frac{-1}{\sqrt{2}}\left[\hat{\mathbf{x}} + i\hat{\mathbf{y}}\right]$

dipole matrix elements

σ^+ transition	$\mathbf{d} = \mu\hat{\sigma}_-$
σ^- transition	$\mathbf{d} = \mu\hat{\sigma}_+$

quantities that follow from above definitions

Rabi frequency	$\Omega_R = \frac{2\mu}{\hbar}\mathcal{E}(t)$
pulse area	$\theta(t) = \frac{2\mu}{\hbar}\int_{-\infty}^{t}\mathcal{E}(t')dt'$
intensity (irradiance)	$I = cn\epsilon_0 \left\langle |\mathbf{E}(t)|^2 \right\rangle_{\text{optical cycle}}$
	$I = 2cn\epsilon_0|\mathcal{E}(t)|^2$

other conventions

charge of electron	$-e = -1.6 \times 10^{-19}$ C
system of units	S.I.
energies	E

CHAPTER 2

SEMICONDUCTORS AND THE TWO-STATE SYSTEM

Some of the most useful and peculiar predictions of nonrelativistic quantum mechanics stem from the study of two-state systems.[1] Otto Stern predicted in 1921 that a spatially inhomogeneous magnetic field would split a beam of silver atoms into two, based on the two eigenstates of the atoms' magnetic moments [19, p. 2]. This concept was demonstrated in the famous Stern-Gerlach experiment in 1922. An electric field gradient was similarly used to spatially separate the two parity-energy eigenstates of ammonia in the first stage of the ammonia maser [20, pp. 9.8–9.9].

Two-state time-dependent Hamiltonians have an even richer history, due in large part to the work of I. I. Rabi. By expressing the Hamiltonian in terms of the Pauli spin matrices, every two-state problem can be made analogous to the spin one-half particle in a magnetic field [20, p. 10.17]. This extends even to the decay of particle number, energy, and coherence in an ensemble of two-state systems. For spin one-half particles in a magnetic field, the quantum theory predicts and experiments confirm spin precession, energy splitting, inversion oscillation (spin nutation, Rabi flopping), spin magnetic resonance, and free-induction decay [21]. All of these have optical analogs for a configuration of atoms that can be considered uncoupled except for decay mechanisms, and hence can be treated as an ensemble of two-level systems.[2] Our research investigates the extension of two-level theory into the optical excitation of a semiconductor.

---

[1]Four Nobel prize winners have taken advantage of two-state resonances: Rabi (molecular beams and magnetic resonance); Bloch and Purcell (**B**-fields in atomic nuclei and nuclear magnetic moments); Townes, Basov, and Prochorov (masers, laser, and quantum optics); and Kastler (optical pumping) [19, p. 325].

[2]It is also necessary that two energy levels be isolated either through selection rules or the absence of nearby levels.

2.1 The two-state system

The classification of some collection of matter and energy as a two-state system is always an approximation. In essence, we must be able to neglect all but two states because of the environment of the experiment. For example, even though the silver atoms of the Stern-Gerlach experiment have a nucleus and 47 electrons, the nucleus and all but one of the electrons are ignored since no energy can be added or removed from the atoms by the magnetic field, the net angular momentum of the 46 core electrons is zero, and the nuclear spin coupling is weak compared to the electron spin coupling[3] [19, p. 2]. In analyzing the first stage of the ammonia maser, the ammonia molecule can be considered a two-state system with repect to the electrostatic field gradient. As Feynman pointed out, the many states of vibration, rotation, and translation must all be analyzed in terms of the parity states, and the apparatus is arranged so that parity alone determines the direction of the molecule [20, p. 10.1]. In this system, the parity states are inherently a two-state manifold, but the dynamics of the system are adequately explained by the parity states only to the extent that other interactions can be ignored.

The two-state approximation has been fruitfully applied to many systems in addition to the silver atom spin states and the ammonia parity states. It has been applied to the hydrogen molecular ion with respect to its electron-proton configurations, to the pion exchange of a proton-neutron pair, to the hydrogen molecule with respect to electron exchange and binding, to the bonding configurations of the benzene molecule, and to dyes with two chemical configurations [20, Chapter 10]. Of paramount interest to us, the two-state approximation is applied to the resonant electric dipole interaction that couples electronic, vibrational, and rotational energy levels in atoms and molecules, and to a lesser degree, certain condensed matter.

For light-matter interactions, it is the resonance condition that allows us to ignore nondegenerate energy levels, and selection rules that allow us to ignore de-

---

[3]It is not entirely true that we can ignore the extra electrons. In 1927, Phipps and Taylor did the Stern-Gerlach experiment with the better understood hydrogen atom. Only then did the quantitative results closely match theory [22].

generate levels. Unlike the Stern-Gerlach or ammonia molecule examples, there are always more electronic states than the two states characteristic of spin 1/2 or parity states. In a suitable system, we can ignore nonresonant coupling because it is very much weaker than near-resonant couping. For degenerate states, selection rules often dictate that certain interactions will occur so infrequently that they can be ignored. Rabi applied the resonance condition to define his two-state system in the earliest two-state experiments; although the fluorine isotope he used was spin 1/2, the lithium isotopes were not, so the two levels of interest were isolated through resonance. A detailed discussion of the two-state approximation applied to atomic energy levels is found in the classic *Optical Resonance and Two-Level Atoms* by Allen and Eberly [21, pp. 28–34].

As in the Stern-Gerlach experiment, we ignore certain aspects of the light–semiconductor system when we analyze measurements, such as higher order electric multipole interactions, sample inhomogeneities, and core electrons. For the two-state model to be adequate, the experiment must be contrived so that interactions outside of the two-state system have a negligable impact on the two-state system itself, or at least an effect that can be accounted for. Furthermore, the researcher must be able to separate two-state behavior from any other signal in the experimental data. In solids, it is not yet possible to predict with great quantitative accuracy the nonlinear optical response, so the final arbiter as to the oversimplification of a particular model is the agreement (or lack of agreement) between experiment and theory. Ultimately, a system can be described as a two-state system if the dynamics of the system can be predicted (to a subjective degree determined by the beholder) using the expansion of the state vector into two base kets,

$$|\psi\rangle = a_1 |1\rangle + a_2 |2\rangle, \tag{2.1}$$

and a suitable Hamiltonian.
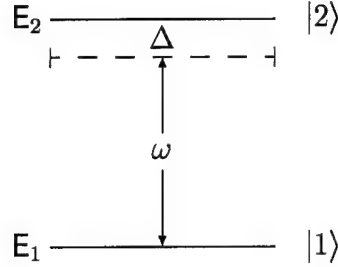
Figure 2.1: A schematic representation of a two-state system showing the energy levels of the states and the field coupling the states. The states are coupled by near resonant optical pulses with carrier frequency ω detuned from exact resonance by Δ.

2.2 Equations of motion for the two-state problem

For the general two-state problem, we will take as our basis the energy eigenstates of the non-interacting system. We write the Hamiltonian as

$$H = H_0 + V(t), \qquad (2.2)$$

where $H_0|1\rangle = E_1|1\rangle$ and $H_0|2\rangle = E_2|2\rangle$. In doing so we are considering $V(t)$ to be some possibly time dependent interaction potential that is not necessarily small.

We can write the matrix elements of this Hamiltonian as

$$H \doteq \begin{pmatrix} \langle 1|H_0|1\rangle & \langle 1|V(t)|2\rangle \\ \langle 2|V(t)|1\rangle & \langle 2|H_0|2\rangle \end{pmatrix} = \begin{pmatrix} E_1 & V_{12}(t) \\ V_{21}(t) & E_2 \end{pmatrix}. \qquad (2.3)$$

We have assumed $V_{11}(t) = V_{22}(t) = 0$ as is appropriate for states of definite parity and a potential that is odd in spatial coordinates.[4]

Using equations 2.1 and 2.2 in Schrödinger's equation,

$$i\hbar \frac{\partial}{\partial t}|\psi\rangle = H|\psi\rangle, \qquad (2.4)$$

---

[4]The product of an odd function (potential) with two even or two odd functions (wavefunction and its complex conjugate) integrated over symmetric limits vanishes.

yields the coupled equations

$$i\hbar\frac{d}{dt}a_1(t) = \mathsf{E}_1 a_1(t) + V_{12}(t)a_2(t) \tag{2.5}$$

$$i\hbar\frac{d}{dt}a_2(t) = \mathsf{E}_2 a_2(t) + V_{21}(t)a_1(t). \tag{2.6}$$

Without assuming something about the interaction potential, this is about as far as we can go.

The coupled equations 2.5 and 2.6 apply to a single two-state particle in the potential $V(t)$. We can extend the analysis to an ensemble of many coherent non-interacting particles just by multiplying by the number of particles. We must go to a density matrix formalism to include decay mechanisms such as spontaneous emission and collisions. Finally, we must adopt a new approach altogether to account for the crystal lattice and Coulomb interactions in a semiconductor. A detailed theoretical approach to the problem of the coherent light-semiconductor interactions is available in References [7] and [23]. Here we will solve the noninteracting problem in detail, introduce the density matrices, and sketch the solution to the semiconductor problem. We then make the connection between the semiconductor Bloch equations (two-band) and the optical Bloch equations (two-state).

2.3 Optical electric dipole interaction

The Hamiltonian for an electron (effective mass m_e, charge $-e$) in a crystal potential $W(\mathbf{r})$ subject to an external radiation field is [4, p. 115]

$$H(\mathbf{r},t) = \frac{1}{2m_e}\left[\mathbf{p} + e\mathbf{A}(\mathbf{r},t)\right]^2 + W(\mathbf{r}) - eU(\mathbf{r},t). \tag{2.7}$$

The electromagnetic vector potential is $\mathbf{A}(\mathbf{r},t)$ and the scalar potential is $U(\mathbf{r},t)$. We are oversimplifying the problem by ignoring the Coulomb interactions of the many electrons that exist in a real crystal. Furthermore, for the time being, we will assume discreet energies for the two states instead of including the actual banding of the states in a solid. We make these assumptions to get at the essence of the two-state electric dipole interaction, and will correct the shortcomings later.

Optical radiation has a wavelength of at least two orders of magnitude larger than a typical semiconductor lattice constant. Thus, to a good approximation, we can take the lowest order terms in the multipole expansion of the vector and scalar potentials.[5] This leads to a Hamiltonian

$$H(\mathbf{r}, t) = \frac{1}{2m_e} [\mathbf{p} + e\mathbf{A}(0, t)]^2 + W(\mathbf{r}) - e\mathbf{r} \cdot \nabla U(0, t). \tag{2.8}$$

To simplify the form of the Hamiltonian, we make the Göppert-Mayer gauge transformation

$$\mathbf{A}(\mathbf{r}, t) \quad \rightarrow \quad \mathbf{A}(\mathbf{r}, t) + \nabla[-\mathbf{r} \cdot \mathbf{A}(0, t)] \tag{2.9}$$

$$U(\mathbf{r}, t) \quad \rightarrow \quad U(\mathbf{r}, t) - \frac{\partial}{\partial t}[-\mathbf{r} \cdot \mathbf{A}(0, t)], \tag{2.10}$$

which yields

$$\mathbf{A}(0, t) \quad \rightarrow \quad 0 \tag{2.11}$$

$$\nabla U(0, t) \quad \rightarrow \quad \nabla U(0, t) + \frac{\partial}{\partial t}\mathbf{A}(0, t) = -\mathbf{E}(0, t). \tag{2.12}$$

Substituting equations 2.11 and 2.12 into equation 2.8 we get the familiar electric dipole interaction Hamiltonian

$$H(\mathbf{r}, t) = H_0 - \mathbf{d} \cdot \mathbf{E}(0, t), \tag{2.13}$$

using the Hamiltonian in the absence of the electric field $H_0 = \mathbf{p}^2/2m_e + W(\mathbf{r})$ and the electric dipole moment $\mathbf{d} \equiv e\mathbf{r}$.

2.3.1 The undamped optical two-state solution

Using equations 2.5 and 2.6 with the interaction Hamiltonian $V(\mathbf{r}, t) = -\mathbf{d} \cdot \mathbf{E}(0, t)$ derived above, we now solve the equations of motion for the two probability amplitudes $a_1(t)$ and $a_2(t)$. Note that we are still assuming discreet energy eigenvalues instead of energy bands. We will drop the explicit space dependence of the electric

---

[5]For details on the mathematics of this section, see Reference [24, pp.266–275] One must reconstruct the Lagrangian after the approximation or gauge transformation to determine the new Hamiltonian.

field because of the dipole approximation, and assume the field to be a circularly polarized classical field, consistent with our experiments.

We will furthermore specialize to the case of a p-orbital to s-orbital transition since it also corresponds to our experiments. This leads to some simplification of the mathematics, but the results are essentially the same as for any two-state system in a harmonic potential. For definiteness, we assume a right-circularly polarized light field, which induces a $m_j = 3/2$ (state $|1\rangle$) to $m_j = 1/2$ (state $|2\rangle$) transition. For the off-diagonal matrix elements we have

$$
\begin{aligned}
V_{21}(t) &= \langle 2|V(\mathbf{r}, t)|1\rangle & (2.14) \\
&= \langle 2|[-\mathbf{d} \cdot \mathbf{E}(t)]|1\rangle & (2.15) \\
&= -\mathbf{d}_{21} \cdot \mathbf{E}(t) & (2.16) \\
V_{12}(t) &= V_{21}^*(t) & (2.17)
\end{aligned}
$$

For an electon in a central potential, the dipole matrix element $\mathbf{d}_{21}$ for a $\Delta m_j = -1$ transition is proportional to the rotating unit vector $\hat{\sigma}_+ \equiv -(\hat{\mathbf{x}} + i\hat{\mathbf{y}})/\sqrt{2}$ [21, p. 35]. We will call the (real) proportionality constant μ. Writing the right circularly polarized electric field with a slowly varying (and real) pulse envelope as $\mathbf{E}(\mathbf{r}, t) = \hat{\sigma}_-\mathcal{E}(\mathbf{r}, t)e^{i[\mathbf{k}\cdot\mathbf{r}-\omega t]} + c.c.$, we have[6]

$$
\begin{aligned}
V_{21}(t) &= -\mu\hat{\sigma}_+ \cdot \left[\hat{\sigma}_-\mathcal{E}(t)e^{-i\omega t} + c.c.\right] & (2.18) \\
&= \mu\mathcal{E}(t)e^{-i\omega t} & (2.19)
\end{aligned}
$$

The other matrix element, $V_{12}(t)$, is the complex conjugate of $V_{21}(t)$ since the Hamiltonian is hermitian.

Equations 2.5 and 2.6 are exactly solvable with this interaction Hamiltonian for a constant electric field envelope. Assuming that $\mathcal{E}(t)$ varies slowly enough to ignore its time derivatives (a marginal assumption in some femtosecond experiments), and assuming that the system is in state $|1\rangle$ at $t = 0$, we get the following expressions

---

[6]Our choice of μ makes it positive, and it makes the Rabi frequency positive and real for a $\Delta m_j = -1$ transition. However, our definition of μ makes our Rabi frequency the negative of that usually found in the literature.

for the probability amplitudes:

$$a_1(t) = \left[\cos\left(\frac{\Omega_{gen}}{2}t\right) + i\frac{\Delta}{\Omega_{gen}}\sin\left(\frac{\Omega_{gen}}{2}t\right)\right]e^{-i\Delta t/2} \tag{2.20}$$

$$a_2(t) = -i\frac{\Omega_R}{\Omega_{gen}}\sin\left(\frac{\Omega_{gen}}{2}t\right)e^{-i\Delta t/2}e^{i\omega t}, \tag{2.21}$$

using the variables

detuning $\qquad\qquad\qquad\qquad\Delta = [(\mathsf{E}_2 - \mathsf{E}_1)/\hbar] - \omega$

Rabi frequency $\qquad\qquad\qquad\Omega_R = 2\mu\mathcal{E}(t)/\hbar$

generalized Rabi frequency $\quad\Omega_{gen} = \sqrt{\Delta^2 + \Omega_R^2}.$

At exact resonance ($\Delta = 0$), the probability of being in the upper state $|2\rangle$ oscillates between zero and one.

$$P_2(t) = |a_2|^2 = \sin^2\left(\frac{\Omega_R}{2}t\right) \tag{2.22}$$

Since we have no way for the electron to leave the two-state system, it must be in state $|1\rangle$ if not in state $|2\rangle$: $P_1 = 1 - P_2$. This oscillation between the two states of a two-state system is called Rabi oscillation or Rabi flopping. For an electric dipole interaction it is sometimes called optical nutation after spin nutation in a magnetic field. If detuning is not zero, the amplitudes of the oscillations decrease, and the system oscillates more quickly at the generalized Rabi frequency (see Figure 2.2). A one-electron system like the one just considered remains forever coherent. To include the loss of coherence, we go to a density matrix formalism.

2.3.2 Ensemble averaged density matrices and decay

We could arrive at the Bloch equations for a damped two-state system rather directly by writing the electric dipole Hamiltonian in terms of the Pauli spin matrices and solving the Heisenberg equations of motion for the ensemble averaged spin operators.[7] The ensemble averaged spin operators were the natural variables for the early two-state work which involved spins. When we write the electric dipole interaction Hamiltonian in terms of the spin operators, we gain a new perspective from the

---

[7]See, for example, Reference [21, pp.36–46]
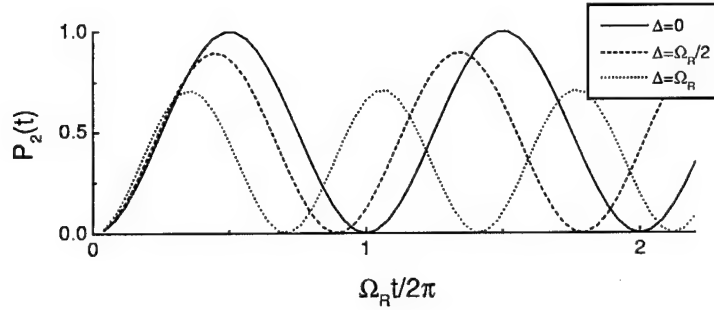
Figure 2.2: The probability of being in the upper state versus time for a two level optical interaction. On resonance, the system oscillates at the Rabi frequency between $P_2 = 0$ and $P_2 = 1$. With detuning, the frequency increases as $\sqrt{\Delta^2 + \Omega_R^2}$ and the oscillation amplitude decreases as $(\Omega_R/\Omega_{gen})^2$.

form of the new variables (transformed into a rotating frame) and their geometrical representation as a spinning top. But instead of doing this, we will introduce the density matrices to get at the problem, since the semiconductor Bloch equations are usually written in the density matrix form rather than using a pseudo-spin vector.

The density matrices are a useful tool to analyze many-body systems because they are statistically averaged over the set of particles (ensemble).[8] Measurements of light absorption or fluorescence in an atomic gas constitute ensemble averaged measurements since the detector collects the light without distinguishing between the atoms. The coherence of the members of an ensemble affects the measurement since it determines their ability to constructively interfere. For a two-state system the density matrix elements are:

$$\text{upper state population} \quad \rho_{22} = \overline{|a_2|^2} \tag{2.23}$$

$$\text{lower state population} \quad \rho_{11} = \overline{|a_1|^2} \tag{2.24}$$

$$\text{coherences} \quad \rho_{12} = \rho_{21}^* = \overline{a_1 a_2^*}. \tag{2.25}$$

The overbar represents an average over the ensemble. The meanings of the diagonal matrix elements ρ_{11} and ρ_{22} is clear enough (occupation probabilities), but the coherences are less clear. They are related to the expectation value of the electric

---

[8]A detailed discussion of density operators and density matrices involves discussion of pure and mixed states, properties of the operators, time evolution, etc., which are beyond the scope of this dissertation. See, for example, Reference [19, section 3.4].

dipole when averaged over the ensemble.

$$\overline{\langle \mathbf{d} \rangle} = \overline{[a_1^*\langle 1| + a_2^*\langle 2|]\mathbf{d}[a_1|1\rangle + a_2|2\rangle]} \tag{2.26}$$

$$= \overline{a_1^* a_2 \mathbf{d}_{12} + a_2^* a_1 \mathbf{d}_{21}} \tag{2.27}$$

$$= \rho_{21}\mathbf{d}_{12} + c.c. \tag{2.28}$$

If the dipoles have completely random phases, the coherence will be zero, meaning both the density matrix element and the correlation of the atomic oscillations.

The density matrix equations of motion can be derived from equations 2.5 and 2.6 using the matrix elements V_{12} and V_{21} (equation 2.19). By making E_1 the zero point energy and using the definitions for the Rabi frequency and detuning, one can write the probability amplitude equations of motion as

$$\frac{d}{dt}a_1(t) = -\frac{i}{2}\Omega_R e^{i\omega t} a_2(t) \tag{2.29}$$

$$\frac{d}{dt}a_2(t) = -i(\omega + \Delta)a_2(t) - \frac{i}{2}\Omega_R e^{-i\omega t} a_1(t). \tag{2.30}$$

Using these, it is straightforward to derive the density matrix equations of motion (without relaxation) from the definitions given in equations 2.23 through 2.25. These equations are

$$\frac{d}{dt}\rho_{22}(t) = \frac{i}{2}\Omega_R \left[\rho_{21}(t)e^{i\omega t} - c.c.\right] \tag{2.31}$$

$$\frac{d}{dt}\rho_{11}(t) = -\frac{d}{dt}\rho_{22}(t) \tag{2.32}$$

$$\left(\frac{d}{dt} + i\Delta\right)\rho_{21}(t)e^{i\omega t} = \frac{i}{2}\Omega_R \left[\rho_{22}(t) - \rho_{11}(t)\right] \tag{2.33}$$

$$\frac{d}{dt}\rho_{12}(t) = \frac{d}{dt}\rho_{21}^*(t) \tag{2.34}$$

One of the more useful aspects of the density matrix equations of motion is that damping mechanisms such as collisions are easily included. One can either add terms to the Hamiltonian to account for decay and dephasing, or simply add phenomenological decay and dephasing terms.[9] We take the latter approach, which

---

[9]For a theoretical approach to collision terms resulting in the Boltzmann collision rates see Reference [7, Section 12-3].

can be accounted for symbolically by adding a term $d\rho_{ij}/dt|_{col}$ to the right hand side of the equation for the "coherence" density matrix element ρ_{ij}. Note that the decay of this matrix element results in the diminution of the ensemble averaged dipole, and thus in the coherent behavior of the collection of two-state systems. Once the coherence is lost, if one dipole is absorbing a photon another is as likely to be emitting a photon, and the system displays a steady state behavior.

2.3.3 The Bloch sphere and pulse area theorem

An insightful geometrical approach [25, 26] is based on transforming the density matrix variables (or electric dipole Hamiltonian) into variables appropriate for a spin 1/2 particle in a magnetic field. This done, the behavior of the system looks like a magnetic dipole in a magnetic field, where the **B**-field exerts a torque $\mathbf{N} = \mathbf{m} \times \mathbf{B}$ on the magnetic dipole moment **m**. The angular momentum of the magnetic dipole changes in direction in accordance with the classical relation $\mathbf{N} = d\mathbf{L}/dt$. The angular momentum, in turn, is proportional to the magnetic moment through the gyromagnetic ratio γ. The well known result for a constant **B** is the precession of the dipole moment about the magnetic field, $d\mathbf{m}/dt = \gamma\mathbf{m} \times \mathbf{B}$ [27, pp. 232–235].

We proceed by defining the components of the Bloch vector $\mathbf{S} = u(t)\hat{\mathbf{x}} + v(t)\hat{\mathbf{y}} + w(t)\hat{\mathbf{z}}$, which are the real numbers [7, p. 78]:

$$u(t) = [\rho_{21}(t)e^{i\omega t} + c.c.] = 2\,\text{Re}\{\rho_{21}(t)\}\cos(\omega t) \tag{2.35}$$

$$v(t) = i[\rho_{21}(t)e^{i\omega t} - c.c.] = -2\,\text{Im}\{\rho_{21}(t)\}\sin(\omega t) \tag{2.36}$$

$$w(t) = \rho_{22}(t) - \rho_{11}(t) \tag{2.37}$$

The equations of motion for these variables are

$$\frac{d}{dt}u(t) = -\Delta v(t) - \frac{u(t)}{T_2} \tag{2.38}$$

$$\frac{d}{dt}v(t) = \Delta u(t) - \Omega_R w(t) - \frac{v(t)}{T_2} \tag{2.39}$$

$$\frac{d}{dt}w(t) = \Omega_R v(t) - \frac{w(t) - w_{eq}}{T_1}, \tag{2.40}$$

which, in the limit of no decay $(T_1 = T_2 \to \infty)$ is equivalent to the vector equation

$$\frac{d}{dt}\mathbf{S} = \mathbf{Q} \times \mathbf{S}. \tag{2.41}$$

for a vector of the rotation frequency $\mathbf{Q} = \Omega_R \hat{x} + \Delta \hat{z}$ (sometimes called the "torque" or "axis" vector). The rotation frequency label comes from identifying $\mathbf{S}$ as a dimensionless position vector for an object undergoing centripetal acceleration with angular velocity $\mathbf{Q}$ [7, p. 78]. In our magnetic field analogy, $\mathbf{Q}$ is like a magnetic field that exerts a torque on the magnetic moment. $\mathbf{S}$ is like the (intrinsic) angular momentum that is proportional to the magnetic moment.
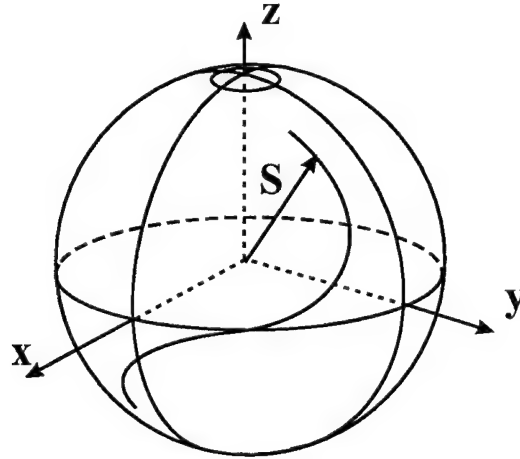
Figure 2.3: The two-state optical response is represented by the motion of the Bloch vector $\mathbf{S}$ in the Bloch sphere. The $\hat{x}$ component of $\mathbf{S}$ corresponds to the polarization in-phase with the electric field, which is responsible for dispersive effects. The $\hat{y}$ component is the in-quadrature polarization responsible for absorption and gain. The $\hat{z}$ component is the inversion.

For a constant amplitude optical field and constant detuning (constant $\mathbf{Q}$), the Bloch (or pseudo-spin) vector $\mathbf{S}$ precesses about the $\mathbf{Q}$ axis. If the detuning is zero (resonant excitation), $\mathbf{S}$ rotates at the Rabi frequency in a circle in the $\hat{y}$-$\hat{z}$ plane. We took out the optical frequencies in our definition of the Bloch vector components, but in that original frame, the Bloch vector precesses about the $\hat{z}$ axis at the optical frequency ω and nutates like a top [27, pp. 213–225] at the Rabi frequency (see Figure 2.4). This is the origin of the term "optical nutation," and is the same Rabi

oscillation behavior as derived previously; the inversion oscillates (in the resonant case) between -1 and 1 as does $v(t)$.
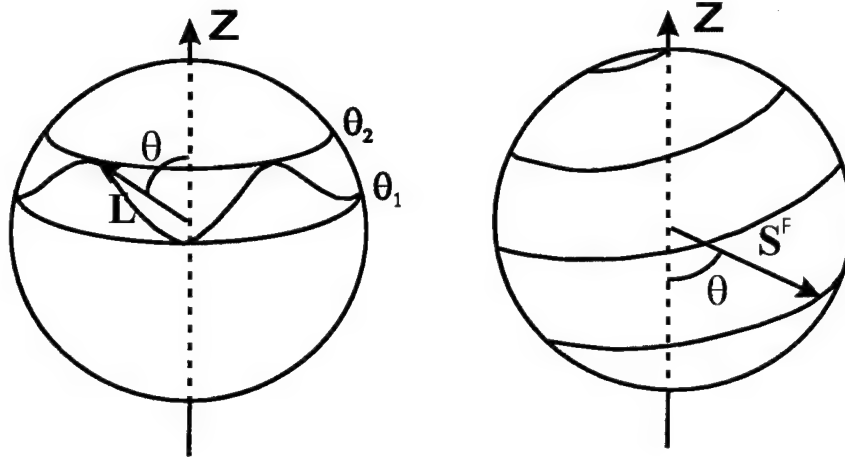
Figure 2.4: The optical nutation description of Rabi oscillations. A top rotates about it principal axis with an angular momentum **L**. The angular momentum **L** both precesses (rotates about the vertical z axis) and nutates (oscillates up and down). The nutation is bound between the angles θ_1 and θ_2, both between 0° and 90°. The two-state optical response is governed by similar equations in the non-rotating frame. The Bloch vector for a constant **E**-field resonant interaction in the non-rotating coordinate system, $\mathbf{S}^F$, precesses at the optical frequency about the z (inversion) axis and nutates between $w = -1$ and $w = 1$ at the Rabi frequency. In the rotating frame, only the nutation remains.

What should we make of $v(t)$? From equations 2.28 and 2.36 we see that $-v(t)$ is the normalized component of the electric dipole in quadrature with the electric field [21, p. 45]. It is well known from optics that this corresponds the absorption or amplification of the incident field [1, pp. 358–360]. The incident field is alternatingly absorbed and amplified at the Rabi frequency. This behavior will decay at a characteristic time T_2 to the steady state. From similar considerations, we can see that $u(t)$ corresponds to the in-phase part of the electric dipole responsible for refractive effects.

Without decay, the Bloch vector remains a unit vector. Decay shrinks the components exponentially as e^{-t/T_1} and e^{-t/T_2} respectively. The vanishing of the Bloch vector corresponds to entering the steady state where none of the components change

with time.

Time varying electric field envelopes can be conveniently recast in terms of the pulse area

$$\theta(t) = \frac{2\mu}{\hbar} \int_{-\infty}^{t} \mathcal{E}(t')dt'. \tag{2.42}$$

At zero detuning, equations 2.38, 2.39, and 2.40 take the form

$$\frac{d}{dt}u(t) = 0 \tag{2.43}$$

$$\frac{d}{dt}v(t) = -\Omega_R w(t) \tag{2.44}$$

$$\frac{d}{dt}w(t) = \Omega_R v(t), \tag{2.45}$$

with solutions

$$u(t) = u(0) \tag{2.46}$$

$$v(t) = -w(0)\sin\theta(t) + v(0)\cos\theta(t) \tag{2.47}$$

$$w(t) = v(0)\sin\theta(t) + w(0)\cos\theta(t) \tag{2.48}$$

The pulse area is the angle that the Bloch vector makes with the $-\hat{z}$ axis. A pulse with an area that is an integer multiple of 2π will leave the medium in its initial state, while an odd integral multiple of π pulse area will take the ensemble from a definite lower state ($w = -1$) to complete inversion ($w = 1$). A multiple π pulse will induce oscillations in the inversion as it passes. This is yet another way to look at Rabi oscillations, but this time the formalism is extended to include optical pulses. The result of equation 2.22 can be recovered using $|a_2|^2 = (w + 1)/2$, $w(0) = -1$, and $v(0) = 0$.

2.4 Semiconductor Bloch equations

We now adopt an approach that includes the banding (energy dependence on $\mathbf{k}$) of the real semiconductor and that includes the Coulomb interaction between carriers. This approach involves a great deal of algebra, so only the basic ideas are sketched
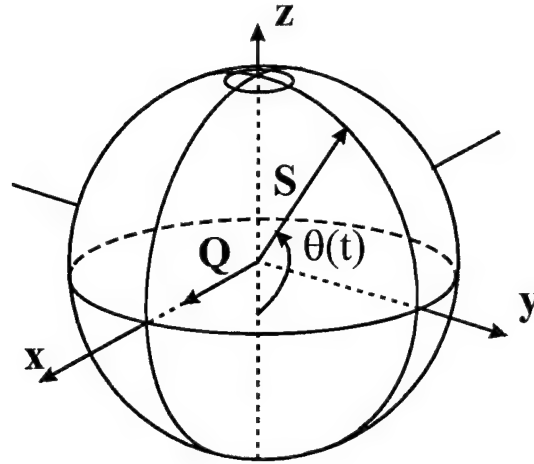
Figure 2.5: Rabi oscillations related to pulse area. For resonant excitation, the Bloch vector **S** rotates about the $\hat{x}$ axis at the Rabi frequency Ω_R in accordance with $d\mathbf{S}/dt = \mathbf{Q} \times \mathbf{S}$. The pulse area $\theta(t)$ is the angle that **S** makes with the $-\hat{z}$ axis.

here. A detailed accounting of this approach is found in References [7] and [23]. The result of our efforts will be the so-called semiconductor Bloch equations, which are subsequently shown to reduce to optical Bloch equations by ignoring the Coulomb interaction and to the Wannier equation for excitons in the low carrier density limit.

2.4.1 Semiconductor Hamiltonian

In order to account for the many-body interactions inherent in the semiconductor, we use quantum field theory.[10] We restrict the theory to two parabolic bands in a direct gap semiconductor. The Hamiltonian consists of three parts: (1) the kinetic energy and lattice potential, H_0; (2) the Coulomb interaction between electons, between core ions, and beween electrons and core ions, H_C; and (3) the electric dipole interaction, H_I.

$$H = H_0 + H_C + H_I. \tag{2.49}$$

---

[10]The second quantization method and notation are from OPTI 561, Physics of Semiconductors, a course at the University of Arizona taught by Prof. Rudolph Binder.

For an electron of effective mass m_e in the periodic lattice potential V_L we express H_0 in second quantization as

$$H_0 = \int d^3r \sum_s \psi_s^\dagger(\mathbf{r}) \left\{ -\frac{\hbar^2\nabla^2}{2m_e} + V_L \right\} \psi_s(\mathbf{r}). \tag{2.50}$$

The integral is over the volume of the semiconductor and the sum is over the two spin states. The field operator $\psi^\dagger(\mathbf{r})$ is the usual creation operator in real space, with $\psi(\mathbf{r})$ being its hermitian conjugate. We expand $\psi^\dagger(\mathbf{r})$ in terms of the single particle Bloch wavefunctions $\phi_{\nu\mathbf{k}}^*$ for the electron in the periodic potential:

$$\psi_s^\dagger(\mathbf{r}) = \sum_{\mathbf{k},\nu} \phi_{\nu\mathbf{k}}^*(\mathbf{r}) a_{\nu\mathbf{k}}^\dagger, \tag{2.51}$$

where the $a_{\nu,\mathbf{k}}^\dagger$ are creation operators in Fock space (i.e. they create an electron in state $|\nu\mathbf{k}\rangle$), and

$$\left\{ -\frac{\hbar^2\nabla^2}{2m_e} + V_L \right\} \phi_{\nu\mathbf{k}}(\mathbf{r}) = \mathsf{E}_{\nu\mathbf{k}}^0 \phi_{\nu\mathbf{k}}(\mathbf{r}). \tag{2.52}$$

The expansion of equation 2.51 combined with the orthonormality of the Bloch wavefunctions allow us the write H_0 in the form

$$H_0 = \sum_{\mathbf{k},\nu} \mathsf{E}_{\nu\mathbf{k}}^0 a_{\nu\mathbf{k}}^\dagger a_{\nu\mathbf{k}}, \tag{2.53}$$

with ν representing the four band indices corresponding to the two spin states at each $\mathbf{k}$ for each of the two bands.

The electrons in the semiconductor are not in position eigenstates, so their locations must be described by a probability density $\psi^*\psi$ or its equivalent. This means that we must calculate the Coulomb interaction in terms of charge density. In second quantization, we use density operators for the electron density at positions $\mathbf{r}$ and $\mathbf{r}'$ in the expression for the Coulomb Hamiltonian[11]

$$H_C = \frac{1}{2} \int d^3r \int d^3r' \sum_{s,s'} \psi_s^\dagger(\mathbf{r})\psi_{s'}^\dagger(\mathbf{r}')V^C(\mathbf{r}-\mathbf{r}')\psi_{s'}(\mathbf{r}')\psi_s(\mathbf{r}) \tag{2.54}$$

---

[11]The ordering of the operators has to do with the cancellation of the self-interaction energy. If the usual ordering with the "$\mathbf{r}$" operators to the left of V^C and "$\mathbf{r}'$" operators to the right (or vice-versa), then a term $NV(r=0)/2$ must be subtracted in the Hamiltonian.

where $V^C(\mathbf{r} - \mathbf{r}')$ is the Coulomb potential energy

$$V^C(\mathbf{r} - \mathbf{r}') \equiv \frac{1}{4\pi\epsilon_0}\frac{e^2}{|\mathbf{r} - \mathbf{r}'|} \tag{2.55}$$

Substituting the expansion of equation 2.51 for the creation and destruction operators, and using the Fourier transform[12] $V^C(\mathbf{r} - \mathbf{r}') = (1/L^3)\sum_{\mathbf{q}} e^{i\mathbf{q}\cdot(\mathbf{r}-\mathbf{r}')}\tilde{V}^C(q)$ we get

$$H_C = \frac{1}{2}\sum_{\{\mathbf{k}\},\{\nu\},\mathbf{q}\neq 0}\frac{1}{L^3}\tilde{V}^C(\mathbf{q})\left\langle\nu_1\mathbf{k}_1|e^{i\mathbf{q}\cdot\mathbf{r}}|\nu_4\mathbf{k}_4\right\rangle\left\langle\nu_2\mathbf{k}_2|e^{-i\mathbf{q}\cdot\mathbf{r}'}|\nu_3\mathbf{k}_3\right\rangle a^\dagger_{\nu_1\mathbf{k}_1}a^\dagger_{\nu_2\mathbf{k}_2}a_{\nu_3\mathbf{k}_3}a_{\nu_4\mathbf{k}_4}. \tag{2.56}$$

The deletion of $\mathbf{q} = 0$ from the sum is because that term is exactly cancelled by the ion-ion and electron-ion contributions when the ion charge density is considered a smooth background (jellium model). We make one more approximation in the Coulomb interaction Hamiltonian:

$$\langle\nu\mathbf{k}|e^{-i\mathbf{q}\cdot\mathbf{r}}|\nu'\mathbf{k}'\rangle = \frac{1}{L^3}\int d^3r\, e^{-i\mathbf{k}\cdot\mathbf{r}}u_{\nu\mathbf{k}}(\mathbf{r})e^{-i\mathbf{q}\cdot\mathbf{r}}e^{i\mathbf{k}'\cdot\mathbf{r}}u_{\nu'\mathbf{k}'}(\mathbf{r}) \tag{2.57}$$

$$\approx \delta_{\nu\nu'}\delta_{\mathbf{k}+\mathbf{q},\,\mathbf{k}'}, \tag{2.58}$$

which leaves us with (after some relabeling):

$$H_C = \frac{1}{2}\sum_{\mathbf{k},\mathbf{k}',\nu,\nu',\mathbf{q}\neq 0}\frac{1}{L^3}\tilde{V}^C(\mathbf{q})a^\dagger_{\nu,\mathbf{k}+\mathbf{q}}a^\dagger_{\nu',\mathbf{k}'-\mathbf{q}}a_{\nu'\mathbf{k}'}a_{\nu\mathbf{k}}. \tag{2.59}$$

Finally we have the dipole interaction Hamiltonian, which we write as

$$H_I = -\int d^3r\sum_s\psi^\dagger_s(\mathbf{r})[\mathbf{d}\cdot\mathbf{E}(\mathbf{r},t)]\psi_s(\mathbf{r}) \tag{2.60}$$

Making the equation 2.51 substitutions again, we can express this as

$$H_I = -\sum_{\mathbf{k},\nu,\nu'}[\mathbf{d}_{\nu'\nu}(\mathbf{k})\cdot\mathbf{E}(\mathbf{r},t)]a^\dagger_{\nu'\mathbf{k}}a_{\nu\mathbf{k}} \tag{2.61}$$

---

[12]We use the Fourier transform pair $\tilde{f}(\mathbf{k}) = \int d^3r\exp(-i\mathbf{k}\cdot\mathbf{r})f(\mathbf{r})$ and $f(\mathbf{r}) = (1/[2\pi]^3)\int d^3k\exp(i\mathbf{k}\cdot\mathbf{r})\tilde{f}(\mathbf{k}) = (1/L^3)\sum_{\mathbf{k}}\exp(i\mathbf{k}\cdot\mathbf{r})\tilde{f}(\mathbf{k})$. The last two expressions for $f(\mathbf{r})$ are equivalent in the limit $L \to \infty$.

2.4.2 Density matrix elements

In equations 2.26 through 2.28 we identified the ensemble averaged expectation value of the electric dipole moment with the density matrix elements we called the "coherences." By making the same calculation within the quantum field theory formalism, we can identify the coherences in terms of the Fock space creation and destruction operators.

$$\overline{\langle \mathbf{d} \rangle} = \int d^3r \sum_s \langle \psi_s^\dagger(\mathbf{r})|\mathbf{d}|\psi_s(\mathbf{r})\rangle \tag{2.62}$$

$$= \sum_{\mathbf{k},\mathbf{k}',\nu,\nu'} \langle \nu\mathbf{k}|\mathbf{d}|\nu'\mathbf{k}'\rangle \left\langle a_{\nu\mathbf{k}}^\dagger a_{\nu'\mathbf{k}'} \right\rangle \tag{2.63}$$

$$= \sum_{\mathbf{k},\mathbf{k}',\nu,\nu'} \mathbf{d}_{\nu\mathbf{k},\nu'\mathbf{k}'} \left\langle a_{\nu\mathbf{k}}^\dagger a_{\nu'\mathbf{k}'} \right\rangle . \tag{2.64}$$

The link between the first two lines is the expansion of equation 2.51, and the last line just changes notation. We mentioned in Chapter 1 that the negligable momentum (or wave vector) of the optical photon compared to the first Brillouin zone limits light-semiconductor interactions to near "vertical" transitions. This means that it is only possible to have a light induced dipole moment when the "crystal momentum" $\mathbf{k}$ does not change, or in terms of the notation above, $\mathbf{k} = \mathbf{k}'$. Furthermore, our Hamiltonian in its current state of approximation (electric dipole interaction) does not change the spin angular momentum.[13] The four values of ν and ν' in our summation are reduced to a sum over two states (c for conduction and v for valence) and an overall factor of 2 for the spin states. These additional considerations allow us to simplify equation 2.64 to

$$\overline{\langle \mathbf{d} \rangle} = 2 \sum_{\mathbf{k}} \left[\mathbf{d}_{vc} \left\langle a_{v\mathbf{k}}^\dagger a_{c\mathbf{k}} \right\rangle + \mathbf{d}_{cv} \left\langle a_{c\mathbf{k}}^\dagger a_{v\mathbf{k}} \right\rangle \right] \tag{2.65}$$

$$= 2 \sum_{\mathbf{k}} \left[\left\langle a_{v\mathbf{k}}^\dagger a_{c\mathbf{k}} \right\rangle \mathbf{d}_{vc} + c.c. \right] \tag{2.66}$$

By comparison with equation 2.28 we identify $\left\langle a_{v\mathbf{k}}^\dagger a_{c\mathbf{k}} \right\rangle$ and its complex conjugate as the coherences. Since it is diagonal in $\mathbf{k}$ it is often called an element of the

---

[13]Selection rules for electric dipole, magnetic dipole, and electric quadrupole transitions are examined in detail in Reference [28, pp. 120–138, 178–224].

"reduced" density matrix.

We can identify the diagonal density matrix elements, called the "populations," by examining equation 2.53. The expectation value of H_0 is the occupation probability of state $|\nu\mathbf{k}\rangle$ times its eigenenergy $E^0_{\nu\mathbf{k}}$. The occupation probability is the so-called population, so the complete set of reduced density matrix elements is:

$$\rho_{22} \;\rightarrow\; \left\langle a^\dagger_{c\mathbf{k}} a_{c\mathbf{k}} \right\rangle \equiv f_c(\mathbf{k}) = f_e(\mathbf{k}) \tag{2.67}$$

$$\rho_{11} \;\rightarrow\; \left\langle a^\dagger_{v\mathbf{k}} a_{v\mathbf{k}} \right\rangle \equiv f_v(\mathbf{k}) = 1 - f_h(-\mathbf{k}) \tag{2.68}$$

$$\rho_{21} \;\rightarrow\; \left\langle a^\dagger_{v\mathbf{k}} a_{c\mathbf{k}} \right\rangle \equiv P_{cv}(\mathbf{k}) \tag{2.69}$$

$$\rho_{12} \;\rightarrow\; \left\langle a^\dagger_{c\mathbf{k}} a_{v\mathbf{k}} \right\rangle \equiv P^*_{cv}(\mathbf{k}). \tag{2.70}$$

From here on, we will use the symbols $P_{cv}(\mathbf{k})$, $f_h(\mathbf{k})$, and $f_e(\mathbf{k})$, with subscripts c for conduction band, v for valence band, e for electron, and h for hole. All are time dependent, although the explicit time dependence is suppressed.

2.4.3 SBE equations of motion

We can derive the equations of motion for these variables by applying the Heisenberg equations of motion to the operators and then taking the expectation values. There is much cumbersome but straightforward operator algebra which we will skip. We get the following results:

$$i\hbar \frac{\partial}{\partial t} f_e(\mathbf{k}) =$$
$$\sum_{\mathbf{k}',\nu,\mathbf{q}\neq 0} \frac{1}{L^3} \tilde{V}^C(\mathbf{q}) \left[\left\langle a^\dagger_{c\mathbf{k}} a^\dagger_{\nu,\mathbf{k}'-\mathbf{q}} a_{\nu\mathbf{k}'} a_{c,\mathbf{k}-\mathbf{q}} \right\rangle + \left\langle a^\dagger_{\nu,\mathbf{k}'+\mathbf{q}} a^\dagger_{c,\mathbf{k}-\mathbf{q}} a_{\nu\mathbf{k}'} a_{c\mathbf{k}} \right\rangle \right]$$
$$- \sum_\nu \left[\mathbf{d}_{c\nu} \cdot \mathbf{E} \left\langle a^\dagger_{c\mathbf{k}} a_{\nu\mathbf{k}} \right\rangle - c.c. \right] \tag{2.71}$$

$$i\hbar \frac{\partial}{\partial t} f_h(\mathbf{k}) = i\hbar \frac{\partial}{\partial t} f_e(\mathbf{k}) \tag{2.72}$$

$$i\hbar\frac{\partial}{\partial t}P_{cv}(\mathbf{k}) = \left[\mathsf{E}_{c\mathbf{k}}^0 - \mathsf{E}_{v\mathbf{k}}^0\right]P_{cv}(\mathbf{k})$$

$$-\sum_{\mathbf{k}',\nu,\mathbf{q}\neq 0}\frac{1}{L^3}\tilde{V}^C(\mathbf{q})\left[\left\langle a_{v\mathbf{k}}^\dagger a_{\nu,\mathbf{k}'+\mathbf{q}}^\dagger a_{c,\mathbf{k}+\mathbf{q}}a_{\nu\mathbf{k}}\right\rangle + \left\langle a_{v,\mathbf{k}+\mathbf{q}}^\dagger a_{\nu,\mathbf{k}'-\mathbf{q}}^\dagger a_{\nu\mathbf{k}'}a_{c\mathbf{k}}\right\rangle\right]$$

$$-\sum_{\nu}\left[\mathbf{d}_{c\nu}(\mathbf{k})\cdot\mathbf{E}\left\langle a_{v\mathbf{k}}^\dagger a_{\nu\mathbf{k}}\right\rangle - \mathbf{d}_{\nu v}(\mathbf{k})\cdot\mathbf{E}\left\langle a_{\nu\mathbf{k}}^\dagger a_{c\mathbf{k}}\right\rangle\right]. \qquad (2.73)$$

Unfortunately, we cannot solve these equations as they stand.

2.4.4 Hartree-Fock approximation

To progress further we make two appoximations: spatial homogeniety and the Hartree-Fock approximation. The assumption of spatial homogeniety allows us to make the substitution $\langle a_{\nu\mathbf{k}}^\dagger a_{\nu'\mathbf{k}'}\rangle = \delta_{\mathbf{k}\mathbf{k}'}\langle a_{\nu\mathbf{k}}^\dagger a_{\nu'\mathbf{k}'}\rangle$. One can understand this diagonalization by considering the density of an electron gas, which in second quantization is $n(\mathbf{r}) = \sum_s \psi_s^\dagger(\mathbf{r})\psi_s(\mathbf{r})$. If we expand the ψ's as in equation 2.51 and ignore the small scale variations of the $u_{\nu\mathbf{k}}$, we find the Fourier transform of the density to be $\tilde{n}(\mathbf{q}) = \sum_{s,\mathbf{k}} a_{s,\mathbf{k}}^\dagger a_{s,\mathbf{k}+\mathbf{q}}$. The spatially homogeneous Fourier component is obtained with no difference in the wavevectors of $a^\dagger$ and a.

The Hartree-Fock approximation is a method to reduce the four-operator expectation values in the equations of motion to products of two-operator expectation values. Hartree-Fock wavefunctions are defined by the successive operation of Fock-space creation operators, as in

$$|HF\rangle = a_{n_1}^\dagger a_{n_2}^\dagger \cdots a_{n_N}^\dagger|\Phi_0\rangle, \qquad (2.74)$$

where $|\Phi_0\rangle$ is the vacuum state. The four-operator expectation values for a system in a Hartree-Fock state reduce to

$$\left\langle a_1^\dagger a_2^\dagger a_3 a_4\right\rangle = \left\langle a_1^\dagger a_4\right\rangle\left\langle a_2^\dagger a_3\right\rangle - \left\langle a_1^\dagger a_3\right\rangle\left\langle a_2^\dagger a_4\right\rangle. \qquad (2.75)$$

Applying these approximations to equations 2.71 through 2.73, we get the semi-conductor Bloch equations (SBE):

$$\frac{\partial}{\partial t} f_{e/h}(\mathbf{k}, t) = \frac{i}{2} \left[\omega_R^*(\mathbf{k}, t) P_{cv}(\mathbf{k}, t) - c.c. \right] \tag{2.76}$$

$$\left(\frac{\partial}{\partial t} + \frac{i}{\hbar} [\mathbf{E_k} + \Sigma^e(\mathbf{k}, t) + \Sigma^h(\mathbf{k}, t)] \right) P_{cv}(\mathbf{k}, t) = \frac{i}{2} \omega_R(\mathbf{k}, t) \left[f_e(\mathbf{k}, t) + f_h(-\mathbf{k}, t) - 1 \right],$$
$$\tag{2.77}$$

using the definitions:

$$\omega_R(\mathbf{k}, t) = \Omega_R(t) e^{-i\omega t} - \frac{2}{\hbar L^3} \sum_{\mathbf{q}} \tilde{V}^C(\mathbf{q}) P_{cv}(\mathbf{k} + \mathbf{q}, t) \tag{2.78}$$

$$\mathbf{E_k} = \mathbf{E}_{c,\mathbf{k}}^0 - \mathbf{E}_{v,\mathbf{k}}^0 + \frac{1}{L^3} \sum_{\mathbf{q}} \tilde{V}^C(\mathbf{q}) \tag{2.79}$$

$$\Sigma^{e/h}(\mathbf{k}, t) = -\frac{1}{L^3} \sum_{\mathbf{q}} \tilde{V}^C(\mathbf{q}) f_{e/h}(\mathbf{k} + \mathbf{q}, t). \tag{2.80}$$

The e/h superscripts and subscripts mean that the equation applies to both electrons and holes. The equation for P_{vc} is just the complex conjugate of the equation for P_{cv}.

2.4.5   Comparison of SBE to OBE

If we set $\tilde{V}^C(\mathbf{q})$ to zero, the semiconductor Bloch equations (2.76 and 2.77) reproduce the optical Bloch equations (2.31 through 2.34) for each $\mathbf{k}$ by making the associations of equations 2.67 through 2.70. The semiconductor becomes essentially a set of two level systems, one for each allowed $\mathbf{k}$ value. Of course, we cannot in practice turn off the Coulomb interaction.

The semiconductor Rabi frequency $\omega_R(\mathbf{k}, t)$ is renormalized by the Coulomb interaction (equation 2.78). The appearance of the optical frequency oscillation $e^{-i\omega t}$ shows that the positive frequency components of the Coulomb interaction will be effective while the negative frequency components will not, an observation that suggests the rotating wave approximation (see, for example, Reference [19, pp. 323,324]). The appearance of the negative sign before the Coulomb contribution is the opposite of that usually found in the literature and has to do with the phase

chosen for the dipole matrix element (or the sign of μ). The sum over wave vectors in the Coulomb contribution serves to couple the **k** states, so the semiconductor cannot be considered a collection of uncoupled two-state systems.

The semiconductor Bloch equations exhibit a time dependent and **k** dependent renormalization (shrinkage) of the **k** dependent energy differences between the bands (second term on the left side of equation 2.77). This bandgap renormalization depends on the electron/hole density. The change in band curvature affects exciton states since they are a superposition of single particle states (see equation 1.2), but the actual band shift is approximately **k** independent. In practice, the band renormalization is found to compensate for the reduction in binding energy due to band-filling, and the spectral position of the excitons is relatively static.

The factor $[f_e + f_h - 1]$ in equation 2.77 is the inversion, the "w" component of the Bloch vector. The negative of this quantity is called the band-filling factor and it results in what is called phase space filling, state filling, or Pauli blocking. It results, along with plasma screening, in an easily observed bleaching of the exciton resonance. For semiconductor quantum wells, the Pauli-blocking nonlinearity dominates [4, pp. 337–338]. It is very important in our experiments for achieving overlap, for determining the appropriate intensity of light, and for verifying the relative delay of the pulses in our data.

Much more is contained in the SBE that is beyond the scope of this dissertation. We do know clearly what happens in the ideal two-state optical electric dipole interaction, and thus the differences contained in the SBE can be studied by observing the difference in two-state behavior and two-band behavior.

2.4.6 Formation of excitons

The Wannier equation for excitons (equation 1.8) derives from the SBE in the low excitation limit, so excitons are indeed an appropriate system for seeking two-state effects. With low excitation we can neglect the time development of the electron and hole populations and set $f_e = f_h = 0$ for all **k**. The equation for P_{cv}, which is

related to the polarization, reduces to

$$\left(\frac{\partial}{\partial t} + \frac{i}{\hbar}\mathsf{E}_{\mathbf{k}}\right) P_{cv}(\mathbf{k}, t) = -\frac{i}{2}\Omega_R e^{-i\omega t} + \frac{i}{\hbar L^3}\sum_{\mathbf{q}} \tilde{V}^C(\mathbf{q})P_{cv}(\mathbf{k}+\mathbf{q}, t). \qquad (2.81)$$

With our parabolic band assumption, we explicitly show the $\mathbf{k}$ dependence of $\mathsf{E}_{\mathbf{k}}$ by writing

$$\mathsf{E}_{\mathbf{k}} = \frac{\hbar^2 k^2}{2m_r} + \mathsf{E}_g. \qquad (2.82)$$

Fourier transforming equation 2.81 from t to ω', making the substitution from equation 2.82, and multiplying all terms by $i\hbar$, we get

$$\left(\hbar\omega' - \frac{\hbar^2 k^2}{2m_r} - \mathsf{E}_g\right) \tilde{P}_{cv}(\mathbf{k}, \omega') + \frac{1}{L^3}\sum_{\mathbf{q}} \tilde{V}^C(\mathbf{q})\tilde{P}_{cv}(\mathbf{k}+\mathbf{q}, \omega') = \frac{\hbar}{2}\tilde{\Omega}_R(\omega' - \omega).$$

$$(2.83)$$

Since this is an inhomogeneous, linear, differential equation, we can solve it by expanding P_{cv} into the corresponding homogeneous equation [7, p. 177]

$$\frac{\hbar^2 k^2}{2m_r}\tilde{\psi}_n(\mathbf{k}) - \frac{1}{L^3}\sum_{\mathbf{q}} \tilde{V}^C(\mathbf{q})\tilde{\psi}_n(\mathbf{k}+\mathbf{q}) = \mathsf{E}_n\tilde{\psi}_n(\mathbf{k}), \qquad (2.84)$$

The Fourier transform of this equation to real space returns the Wannier equation that we arrived at a different way in Chapter 1 (see equation 1.8).

$$\left(-\frac{\hbar^2}{2m_r}\nabla_r^2 + V^C(\mathbf{r})\right)\psi_n(\mathbf{r}) = \mathsf{E}_n\psi_n(\mathbf{r}). \qquad (2.85)$$

As noted before, the Wannier equation has hydrogenic solutions appropriate to excitons. We could now expand $\tilde{P}_{cv}$ using these solutions and solve equation 2.83. Furthermore, we could calculate the macroscopic polarization using equation 2.66 (divided by the crystal volume) and obtain expressions for the susceptibility, absorption, and refractive index. We will not do this, but merely note that the hydrogen like resonances do show up in the spectrum, but only for s-orbital exciton envelopes in the electric dipole approximation.

2.4.7 Dephasing and decay

Energy and coherence decay play the same role in the SBE as in the OBE. When we made the Hartree-Fock approximation, we lost the collision terms from the equations. There are other (non-electronic) scattering and dephasing mechanisms that can also be added to the Hamiltonian. Systematic approximations do exist for approximating the four operator terms in the Hamiltonian [7, p. 221]. The Boltzmann collision rates for electron-electron and electron-hole scattering represent one such approximation, and can be found in References [29] and [30]. For our purposes, the inclusion of phenomenological damping rates as applied in the two-state case will suffice.

2.5 The two-particle or exciton picture

We have been considering how the two-band model of a semiconductor compares to the ideal two-state system. There is one more slight complication. Nothing resembling excitons occurs in the prototypical optical two-state system, a gas or beam of atoms. Yet it is the exciton resonance that is the most interesting place to look for Rabi oscillations because it is a discreet resonance. What are the two states?

In band-to-band continuum transitions, we can have direct transitions at any wavevector. This creates a band-edge for continuum transitions, beyond which there is finite absorption. The discreet resonances which result from the Coulomb interaction can be viewed simply as other excited states in the N-particle problem [31, p 161]. We can call the bound states excitons while still considering the system described by a single "average" electron in the potential created by everthing else. As we showed in Chapter 1, light induced excitons only occur near the Γ point ($\mathbf{k} = 0$); that is why they are discreet resonances.

Another point of view is to consider the creation or destruction of an exciton to be a two-particle process involving an electron and a hole. This is what we did in Chapter 1 when we introduced an exciton wavefunction as a superposition of

products of electron and hole wavefunctions. This point of view does not conflict with the single electron approximation. The states that derive from the single (averaged) particle include both the excitons and the continuum states.

In light of the two-particle picture, appropriate states to consider are: (1) no electron in the conduction band and no hole in the valence band, and (2) one electron in the conduction band and one hole in the valence band. Alternatively: (1) no exciton, and (2) one exciton.

CHAPTER 3

SEMICONDUCTORS AND THE THREE-STATE "V" SYSTEM

Like the two-state system, the three-state system is an approximation. For optical interactions, the states are isolated by selection rules and by near-resonant electric dipole interactions between states. There are three basic three-state configurations: (1) two resonances which share a common excited state, the "lambda" system; (2) two resonances which share a common ground state, the "V" system; and (3) two resonances for which the ground state of one is the excited state of the other, the "cascade" system (see Figure 3.1). The dynamics of all three systems are similar, with the key differences coming from the inclusion of one or two nondecaying ground states.

As we did with our two-band semiconductor experiments, we conducted our three-band semiconductor experiments utilizing exciton states. The isolation of the three relevant states is described in some detail in Chapter 4. The two resonances involved are the light-hole (lh) and heavy-hole (hh) exciton resonances, which are common to semiconductors with a p-like valence band and an s-like conduction band.

A key element in our scheme for decoupling a three-state system from other states is exciting one transition with right-circularly-polarized light and the other with left-circularly-polarized light. This requires two separate pulse trains to excite the two transitions. Although it is possible to excite both transitions with a single laser (for example as in Reference [32]), the flexibility is limited as well as being unsuitable for our scheme to isolate three states. Experiments with two spectrally separated beams are often called "two-color" although in our case both pulse trains are invisible in the near infrared.
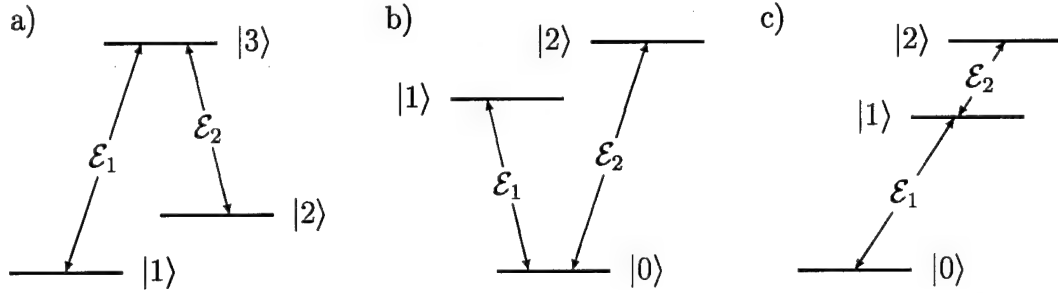
Figure 3.1: Three state configurations: a) lambda ("Λ") system, b) "V" system, c) cascade system. The energy levels of the three states and also the fields coupling the states are shown. The labels are arbitrary.

3.1 The three-state semiconductor Hamiltonian

Our three-band system is a "V" system, represented schematically by Figure 3.2. The Hamiltonian is the same as developed in subsection 2.4.1 with some new interpretations. When we sum over band indices, we sum over all relevant bands; in the case of the two-band system we used two bands labeled c and v; in the three-band system we sum over the conduction band c, the heavy-hole valence band hh, and the light-hole valence band lh. The electric field in the interaction term of the Hamiltonian now consists a term for each of the two near-resonant pulses.

$$\mathbf{E}(\mathbf{r}, t) = \left[\hat{\sigma}_- \mathcal{E}_1(\mathbf{r}, t) e^{i[\mathbf{k}_1 \cdot \mathbf{r} - \omega_1 t]} e^{i\phi_1} + c.c.\right] + \left[\hat{\sigma}_+ \mathcal{E}_2(\mathbf{r}, t) e^{i[\mathbf{k}_2 \cdot \mathbf{r} - \omega_2 t]} e^{i\phi_2} + c.c.\right] \quad (3.1)$$

The factors $e^{i\phi_1}$ and $e^{i\phi_2}$ contain the initial phase angles of the two pulses.

Looking at the band structure, one is tempted to designate the relevant states a lambda system. This would be incorrect since the band structure is a representation of single electron states. The wavefunction for the semiconductor crystal is an N-particle wavefunction, antisymmetric under exchange, given by a superposition of the products of occupied one electron states (the Slater determinant)[6, p. 333]. This means that one should not think of a particular ground state electron as occupying a particular valence band state (in which case it could be excited only to one particular exciton state). Both exciton states are excited two-particle (electron-hole) states,
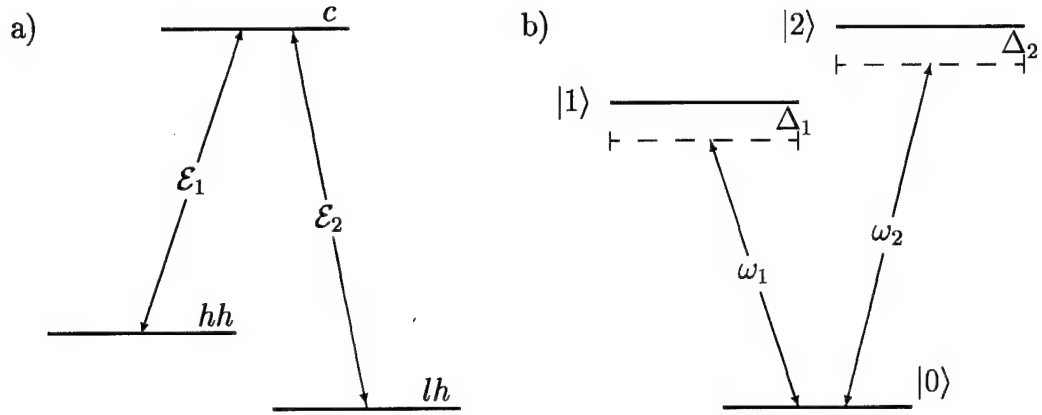
Figure 3.2: a) Dipole transitions that apply to our semiconductor three-band system. The levels represent the energy at the Γ-point ($\mathbf{k} = 0$) for the heavy hole (hh), light hole (lh). and conduction (c) bands. $\mathcal{E}_1$ and $\mathcal{E}_2$ represent the fields that interact with the electric dipole moments. b) The three-state system in the exciton picture. State $|0\rangle$ is the ground state with no exciton, $|1\rangle$ is the hh-exciton state, and $|2\rangle$ is the lh-exciton state. The optical frequencies are given by ω_1 and ω_2, while the detunings are given by Δ_1 and Δ_2.

and either can involve any electron. We cannot distinguish between the initial states appropriate for given lattice positions. Furthermore, the Wannier exciton is properly a mobile excitation of the crystal and not well localized on the scale of the lattice constant [33, p. 12,13]. As we demonstrated in the last chapter, the formation of excitons arises naturally from an expansion of the semiconductor wavefunction in terms of single particle wave functions, but excitons and single particles are clearly different entities that cannot be properly represented on the same energy diagram.

As in the two-state case, we will first consider the semiconductor to be an ideal three-state system to get at the essence of its three-state behavior. Afterwards we will show how the full semiconductor Hamiltonian exhibits the same intervalence-band coherence that we will find in the ideal "V" system (or any of the three-level systems mentioned) and how that leads to a dark state. Writing our system as a superposition of the three states, we have

$$|\psi\rangle = a_0|0\rangle + a_1|1\rangle + a_2|2\rangle, \qquad (3.2)$$

where $|0\rangle$ is the ground state with no exciton, $|1\rangle$ is the hh-exciton state, and $|2\rangle$ is the lh-exciton state. Neglecting the Coulomb interaction and $\mathbf{k}$ dependence we will again write the Hamiltonian in the electric dipole approximation as

$$H = H_0 - \mathbf{d} \cdot \mathbf{E}(0, t), \tag{3.3}$$

with $H_0 = \mathbf{p}^2/2m_e + W(\mathbf{r})$ for a periodic lattice potential $W(\mathbf{r})$.

Because we excite a $\Delta m_j = -1$ transition at the hh-exciton resonance with σ^- light and a $\Delta m_j = +1$ transition at the lh-exciton resonance with σ^+ light (or vice versa), we can simplify our expression for the electric dipole matrix elements:

$$\mathbf{d}_{10} = \mu_1 \hat{\sigma}_+ \tag{3.4}$$

$$\mathbf{d}_{20} = -\mu_2 \hat{\sigma}_-, \tag{3.5}$$

where μ_1 and μ_2 are real and positive, leading to the interaction energy matrix elements

$$-\mathbf{d}_{10} \cdot \mathbf{E}(0, t) = \mu_1 \hat{\sigma}_+ \cdot \left[\hat{\sigma}_- \mathcal{E}_1(t) e^{-i\omega_1 t} e^{i\phi_1} + c.c.\right] \tag{3.6}$$

$$= \mu_1 \mathcal{E}_1(t) e^{-i\omega_1 t} e^{i\phi_1} \tag{3.7}$$

$$-\mathbf{d}_{20} \cdot \mathbf{E}(0, t) = -\mu_2 \hat{\sigma}_- \cdot \left[\hat{\sigma}_+ \mathcal{E}_2(t) e^{-i\omega_2 t} e^{i\phi_2} + c.c.\right] \tag{3.8}$$

$$= -\mu_2 \mathcal{E}_2(t) e^{-i\omega_2 t} e^{i\phi_2}. \tag{3.9}$$

3.2 Three-state equations of motion

Applying Schrödinger's equation to the state vector of equation 3.2 and the Hamiltonian of equation 3.3 we get the equations of motion for the expansion coefficients:

$$i\hbar \frac{d}{dt} a_0(t) = \mu_1 \mathcal{E}_1 e^{i\omega_1 t} e^{-i\phi_1} a_1(t) - \mu_2 \mathcal{E}_2 e^{i\omega_2 t} e^{-i\phi_2} a_2(t) \tag{3.10}$$

$$i\hbar \frac{d}{dt} a_1(t) = \mu_1 \mathcal{E}_1 e^{-i\omega_1 t} e^{i\phi_1} a_0(t) + \mathsf{E}_1 a_1(t) \tag{3.11}$$

$$i\hbar \frac{d}{dt} a_2(t) = -\mu_2 \mathcal{E}_2 e^{-i\omega_2 t} e^{i\phi_2} a_0(t) + \mathsf{E}_2 a_2(t), \tag{3.12}$$

where we have set the zero point energy of the system to the energy of state $|0\rangle$. We now define new variables that take the optical frequencies out of the equations.

For linearly polarized light, this is a prelude to the rotating wave approximation, but for us it is purely a mathematical convenience.

$$c_0 = a_0 \tag{3.13}$$

$$c_1 = a_1 e^{i\omega_1 t} \tag{3.14}$$

$$c_2 = a_2 e^{i\omega_2 t} \tag{3.15}$$

We further define detunings from resonance and Rabi frequencies for the two transitions of interest, retaining an arbitrary initial phase angle for each optical field by using complex Rabi frequencies.

$$\Delta_1 = \frac{\mathsf{E}_1}{\hbar} - \omega_1 \tag{3.16}$$

$$\Delta_2 = \frac{\mathsf{E}_2}{\hbar} - \omega_2 \tag{3.17}$$

$$\Omega_{R1} = \frac{2\mu_1 \mathcal{E}_1(t)}{\hbar} e^{i\phi_1} \tag{3.18}$$

$$\Omega_{R2} = -\frac{2\mu_2 \mathcal{E}_2(t)}{\hbar} e^{i\phi_2} \tag{3.19}$$

Using these definitions, we can write equations of motion for the slowly varying c's.

$$\frac{d}{dt} c_0(t) = -\frac{i}{2} \left[\Omega_{R1}^* c_1(t) + \Omega_{R2}^* c_2(t) \right] \tag{3.20}$$

$$\frac{d}{dt} c_1(t) = -\frac{i}{2} \left[2\Delta_1 c_1(t) + \Omega_{R1} c_0(t) \right] \tag{3.21}$$

$$\frac{d}{dt} c_2(t) = -\frac{i}{2} \left[2\Delta_2 c_2(t) + \Omega_{R2} c_0(t) \right] \tag{3.22}$$

3.3 Equations of motion in another basis

Rather than directly solve the equations of motion 3.20 through 3.22 we will transform to a more convenient basis. In this new basis, the behavior of the system will be more apparent. We define the new basis by the equations:

$$|\psi\rangle = c_0|0\rangle + c_+|+\rangle + c_-|-\rangle \tag{3.23}$$

$$|+\rangle = \frac{1}{\overline{\Omega}_R} \left[\Omega_{R1} e^{-i\omega_1 t}|1\rangle + \Omega_{R2} e^{-i\omega_2 t}|2\rangle \right] \tag{3.24}$$

$$|-\rangle = \frac{1}{\overline{\Omega}_R} \left[\Omega_{R2}^* e^{-i\omega_1 t}|1\rangle - \Omega_{R1}^* e^{-i\omega_2 t}|2\rangle \right], \tag{3.25}$$

which are consistent with equations 3.2 and 3.13 through 3.15 with the definitions:

$$c_0 = c_0(t) \tag{3.26}$$

$$c_+ = \frac{1}{\overline{\Omega}_R}\left[\Omega_{R1}^* c_1(t) + \Omega_{R2}^* c_2(t)\right] \tag{3.27}$$

$$c_- = \frac{1}{\overline{\Omega}_R}\left[\Omega_{R2} c_1(t) - \Omega_{R1} c_2(t)\right] \tag{3.28}$$

$$\overline{\Omega}_R = \sqrt{|\Omega_{R1}|^2 + |\Omega_{R2}|^2}. \tag{3.29}$$

Note that we have defined a new Rabi frequency $\overline{\Omega}_R$ that derives from both electric-dipole Rabi frequencies. Inverting these equations allows us to put the equations for c_0, c_1, and c_2 in terms of the new expansion coefficients. The inverted equations are:

$$c_1 = \frac{1}{\overline{\Omega}_R}\left[\Omega_{R1} c_+(t) + \Omega_{R2}^* c_-(t)\right] \tag{3.30}$$

$$c_2 = \frac{1}{\overline{\Omega}_R}\left[\Omega_{R2} c_+(t) - \Omega_{R1}^* c_-(t)\right], \tag{3.31}$$

and the new equations of motion, neglecting time derivatives of the pulse envelope, become

$$\frac{d}{dt}c_0(t) = -\frac{i}{2}\overline{\Omega}_R c_+(t) \tag{3.32}$$

$$\frac{d}{dt}c_+(t) = -\frac{i}{2}\overline{\Omega}_R c_0(t) - i\left(\frac{\Delta_1 |\Omega_{R1}|^2 + \Delta_2 |\Omega_{R2}|^2}{\overline{\Omega}_R^2}\right) c_+(t)$$

$$-i\left[\Delta_1 - \Delta_2\right]\left(\frac{\Omega_{R1}^* \Omega_{R2}^*}{\overline{\Omega}_R^2}\right) c_-(t) \tag{3.33}$$

$$\frac{d}{dt}c_-(t) = -i\left[\Delta_1 - \Delta_2\right]\left(\frac{\Omega_{R1} \Omega_{R2}}{\overline{\Omega}_R^2}\right) c_+(t) - i\left(\frac{\Delta_1 |\Omega_{R2}|^2 + \Delta_2 |\Omega_{R1}|^2}{\overline{\Omega}_R^2}\right) c_-(t) \tag{3.34}$$

From these equations we can write the matrix representation of the system Hamiltonian in this new basis. Relating the time derivitives to the Hamiltonian through Schrödinger's equation, we get

$$H \doteq \hbar \begin{pmatrix} 0 & \frac{\overline{\Omega}_R}{2} & 0 \\ \frac{\overline{\Omega}_R}{2} & \left(\frac{\Delta_1 |\Omega_{R1}|^2 + \Delta_2 |\Omega_{R2}|^2}{\overline{\Omega}_R^2}\right) & \left[\Delta_1 - \Delta_2\right]\left(\frac{\Omega_{R1}^* \Omega_{R2}^*}{\overline{\Omega}_R^2}\right) \\ 0 & \left[\Delta_1 - \Delta_2\right]\left(\frac{\Omega_{R1}\Omega_{R2}}{\overline{\Omega}_R^2}\right) & \left(\frac{\Delta_1 |\Omega_{R2}|^2 + \Delta_2 |\Omega_{R1}|^2}{\overline{\Omega}_R^2}\right) \end{pmatrix} \tag{3.35}$$

From an examination of either the equations of motion or the Hamiltonian, it is clear that the three states are coupled through the applied electric fields. There is an exception, however, when the detunings Δ_1 and Δ_2 are equal. For this special case, the $|-\rangle$ state becomes uncoupled and its motion is independent of the applied field. Furthermore, this state is an eigenstate of the total Hamiltonian with an eigenenergy of $\hbar\Delta_1 = \hbar\Delta_2 \equiv \hbar\Delta$.[1] Such a state is often called a dressed state of the Hamiltonian [34, p. 70], which is now

$$
H \doteq \hbar \begin{pmatrix} 0 & \frac{\overline{\Omega}_R}{2} & 0 \\ \frac{\overline{\Omega}_R}{2} & \Delta & 0 \\ 0 & 0 & \Delta \end{pmatrix}.
\tag{3.36}
$$

3.4 Discussion of the dark state

The state $|-\rangle$ is called the dark state since it does not interact with the light field. In other words, a material that is in the dark state is transparent. Coherent trapping and electromagnetically induced transparency are based on pumping atoms into the dark state; once there, they can neither absorb light nor decay through stimulated emission. In the case of our semiconductor, excitons in the dark state are not able to absorb or emit light (fluorescence takes much longer than the coherence decay, so it is ignored). As demonstrated numerically by Lindberg and Binder [35], the semiconductor absorbs less light when the detunings are equal as compared to when they are unequal. A system cannot be induced into the dark state by a static light field since the state is noninteracting, but the state can be produced by adiabatic transfer [10, pp. 228–229] and excitons can, in principle, scatter into a superposition of states that includes a dark-state component.

Next we solve the equations of motion for the case of equal detunings where the dark state appears. Following that, we examine the intervalence-band coherence that arises in the three-state system and couples the two excitons. Still studying

---

[1] If we diagonalized the matrix to the eigenbasis, we would only need to diagonalize the 2×2 submatrix of the states $|0\rangle$ and $|+\rangle$ because of the zero elements in the row and column of H_{--}. Thus the eigenenergy can be read directly off the matrix.

the ideal three-state system, we derive the eigenenergies and see how the two-photon Raman-type transition interpretation arises. Lastly, we put the SBE into a form where we can see the genesis of three-state behavior.

3.5 Time dependent probability amplitudes

When we solve the equations of motion 3.32 through 3.34 for $\Delta_1 = \Delta_2 = \Delta$ and arbitrary initial conditions, we get

$$c_0(t) = -\frac{\overline{\Omega}_R A_1}{\overline{\Omega}_{gen} - \Delta} e^{i\overline{\Omega}_{gen} t/2} e^{-i\Delta t/2} + \frac{\overline{\Omega}_R A_2}{\overline{\Omega}_{gen} + \Delta} e^{-i\overline{\Omega}_{gen} t/2} e^{-i\Delta t/2} \quad (3.37)$$

$$c_+(t) = A_1 e^{i\overline{\Omega}_{gen} t/2} e^{-i\Delta t/2} + A_2 e^{-i\overline{\Omega}_{gen} t/2} e^{-i\Delta t/2} \quad (3.38)$$

$$c_-(t) = c_-(0) e^{-i\Delta t} \quad (3.39)$$

where $\overline{\Omega}_{gen} = \sqrt{\overline{\Omega}_R^2 + \Delta^2}$ is the generalized Rabi frequency associated with $\overline{\Omega}_R$, and the factors A_1 and A_2 are initial conditions defined by

$$A_1 = \frac{\overline{\Omega}_R^2}{2\overline{\Omega}_{gen}(\overline{\Omega}_{gen} + \Delta)} c_+(0) - \frac{\overline{\Omega}_R}{2\overline{\Omega}_{gen}} c_0(0) \quad (3.40)$$

$$A_2 = \frac{\overline{\Omega}_R^2}{2\overline{\Omega}_{gen}(\overline{\Omega}_{gen} - \Delta)} c_+(0) + \frac{\overline{\Omega}_R}{2\overline{\Omega}_{gen}} c_0(0), \quad (3.41)$$

subject to the conditions of equations 3.27 and 3.28 and $\sum_j c_j^* c_j = 1$.

In our experiments, $c_0(0) = 1$ and $c_+(0) = c_-(0) = 0$; i.e., the semiconductor starts in the ground state. Without considering time derivitives of the pulse envelopes, and without allowing for interactions other than electric dipole which could populate the dark state, our equations show a dark state forever empty. The numerical calculations of Lindberg and Binder with the full SBE show our current model (i.e., the ideal three-state model with a static light field) to be inadequate in that respect, since the SBE do show theoretical dark state effects with our initial conditions. Nonetheless, let us examine the equations for a static light field with the true initial conditions. For these initial conditions, which are given above, we

have

$$c_0(t) = \left[\cos\left(\frac{\overline{\Omega}_{gen}}{2}t\right) + i\frac{\Delta}{\overline{\Omega}_{gen}}\sin\left(\frac{\overline{\Omega}_{gen}}{2}t\right) \right] e^{-i\Delta t/2} \tag{3.42}$$

$$c_+(t) = -i\frac{\overline{\Omega}_R}{\overline{\Omega}_{gen}}\sin\left(\frac{\overline{\Omega}_{gen}}{2}t\right) e^{-i\Delta t/2} \tag{3.43}$$

$$c_-(t) = 0, \tag{3.44}$$

which indeed shows a non-participating dark state. The first two equations show Rabi oscillations at a frequency derived from both electric fields and both electric dipole moments. In fact, the equations are identical to 2.20 and 2.21 which describe two-state Rabi flopping (the $e^{i\omega t}$ factor in equation 2.21 would disappear if written in terms of slow variables).

The original (slow) expansion coefficents corresponding to the eigenstates of the Hamiltonian with $\mathbf{E} = 0$ develop as

$$c_1(t) = -i\frac{\Omega_{R1}}{\overline{\Omega}_{gen}}\sin\left(\frac{\overline{\Omega}_{gen}}{2}t\right) e^{-i\Delta t/2} \tag{3.45}$$

$$c_2(t) = -i\frac{\Omega_{R2}}{\overline{\Omega}_{gen}}\sin\left(\frac{\overline{\Omega}_{gen}}{2}t\right) e^{-i\Delta t/2}. \tag{3.46}$$

The equation for c_0, which is the same in both bases, is given in equation 3.42. We see here that the probabilities of being in either exciton state are dependent on the relative Rabi frequencies. At equal detunings, the two transitions oscillate at a common Rabi frequency which is different from the individual Rabi frequencies for either transition excited separately.

Consider now the case with a non-zero initial condition for the dark state. If we decide to make $c_+(0) = 0$ as an initial condition, then $c_0(0) = c_-(0) = 1/\sqrt{2}$ to meet the constaints if both are assumed to be real.[2] It should be no surprise that the dark state population stays at $1/2$. The probability amplitudes for $|0\rangle$ and $|+\rangle$ are exactly as given by equations 3.42 and 3.43 if they are multiplied by $1/\sqrt{2}$. The affect of the dark state is simple to remove 50% of the population from the Rabi

---

[2] The selection of $c_+(0) = 0$ affects both $c_1(0)$ and $c_2(0)$. Along with the conservation of probability, there are severly limited choices for the other initial variables.

oscillations at the modified Rabi frequency $\overline{\Omega}_{gen}$. The inactive population is simply transparent.

3.6   Interference and the intervalence-band coherence

For the active state $|+\rangle$, the exciton transition amplitudes for states $|1\rangle$ and $|2\rangle$ add constructively, while for the dark state $|-\rangle$ they interfere destructively. We can see this explicitly in the case we have just considered. The probability of being in the active state is given by

$$|c_+|^2 = \frac{1}{\overline{\Omega}_R^2} \left[|\Omega_{R1}|^2 \, |c_1|^2 + |\Omega_{R2}|^2 \, |c_2|^2 + (\Omega_{R1}^* \Omega_{R2} c_1 c_2^* + c.c.) \right]. \tag{3.47}$$

If we average over the ensemble, then we can write this equation in terms of density matrix elements

$$\rho_{++} = \frac{1}{\overline{\Omega}_R^2} \left[|\Omega_{R1}|^2 \, \rho_{11} + |\Omega_{R2}|^2 \, \rho_{22} + (\Omega_{R1}^* \Omega_{R2} \rho_{12} + c.c.) \right]. \tag{3.48}$$

We can write a similar equation for the probability of the system to be in the dark state, which is an observable since the dark state is an energy eigenstate.

$$\rho_{--} = \frac{1}{\overline{\Omega}_R^2} \left[|\Omega_{R2}|^2 \, \rho_{11} + |\Omega_{R1}|^2 \, \rho_{22} - (\Omega_{R1}^* \Omega_{R2} \rho_{12} + c.c.) \right]. \tag{3.49}$$

In both equations the first two terms are positive definite and involve populations. The last term, which we will call the interference term, involves the intervalence-band coherence ρ_{12} between the two states not coupled directly. For our current case, this coherence is easily calculated assuming no decay. From equations 3.45 and 3.46 we derive

$$\Omega_{R1}^* \Omega_{R2} \rho_{12}(t) = \frac{|\Omega_{R1}|^2 |\Omega_{R2}|^2}{\overline{\Omega}_{gen}^2} \sin^2 \left(\frac{\overline{\Omega}_{gen}}{2} t \right), \tag{3.50}$$

which is positive definite at all times. In the case of the active state, the interference term is positive, corresponding to constructive interference. For the dark state the interference is destructive.

3.7   Eigenenergies and Raman-type transitions

The equal detuning requirement can be viewed in at least two different ways. With the semiclassical formalism we have been using, it is most natural to think of the beat frequency of the two pulse trains as stimulating population transfer from one excited state to the other. The beat frequency exactly matches the energy difference between the two excited states when the electric fields exciting both resonances are equally detuned. The difference (or beat) frequency between the two fields induces a polarization in the medium corresponding to the oscillation between exciton states. Our earlier interpretation of the coherence as related to the average dipole moment (or macroscopic polarization) supports this notion, but the inter-exciton coherence must be related to a second order nonlinear process $(\chi^{(3)})$ instead of a dipole moment. In the one-particle picture one can think of the coherence as between the two valence bands, so long as both excitons have the same binding energy. We know this cannot be precisely true since the effective hole masses differ. However, since the semiconductor reduced density matrix coherences are in terms of single particle bands, it makes sense to think of intervalence-band coherence.

The equal detuning condition, $\hbar\omega_2 - \hbar\omega_1 = E_2 - E_1$, is also the condition for a Raman-type two-photon transition between states $|1\rangle$ and $|2\rangle$ [14, p. 830]. If the pulse trains are considered to be photon wave packets,[3] then it clearly takes a two-photon process to conserve energy in transitions between exciton states. In a quantized electromagnetic field approach to Rabi oscillations the same basic equations derive [34, p. 201–201], which justifies a photon (quantized electromagnetic field) interpretation. At this point we will derive the eigenenergies and schematically depict the processes in terms of photons.

The eigenenergies for the dressed Hamiltonian are easily obtained by diagonalizing the matrix 3.36. Doing so, we get the three eigenenergies $E_- = \hbar\Delta$, $E_\alpha = (\hbar/2)(\Delta + \overline{\Omega}_{gen}) > \hbar\Delta$, and $E_\beta = (\hbar/2)(\Delta - \overline{\Omega}_{gen}) < \hbar\Delta$. The eigenen-

---

[3]The term "photon" is used loosely here, and is meant only to refer to the resonant interaction of quasi-monochomatic light with quantized material energy levels. The same property actually holds with a purely classical view of the electromagnetic field.

ergy E_- corresponds to the dark state $|-\rangle$, which we have already seen to be a superposition of the two exciton states. The other two energy eigenstates are a superposition of the states we have been working with. Defined by the equations $H|\alpha\rangle = \mathsf{E}_\alpha|\alpha\rangle$ and $H|\beta\rangle = \mathsf{E}_\beta|\beta\rangle$, we have

$$|\alpha\rangle = \frac{\overline{\Omega}_R|0\rangle + \left(\Delta + \overline{\Omega}_{gen}\right)|+\rangle}{\sqrt{2}\sqrt{\overline{\Omega}_{gen}^2 + \Delta\overline{\Omega}_{gen}}} \tag{3.51}$$

$$= \frac{\overline{\Omega}_R|0\rangle + \left[\frac{\Omega_{R1}}{\overline{\Omega}_R}\left(\Delta + \overline{\Omega}_{gen}\right)\right]e^{-i\omega_1 t}|1\rangle + \left[\frac{\Omega_{R2}}{\overline{\Omega}_R}\left(\Delta + \overline{\Omega}_{gen}\right)\right]e^{-i\omega_2 t}|2\rangle}{\sqrt{2}\sqrt{\overline{\Omega}_{gen}^2 + \Delta\overline{\Omega}_{gen}}} \tag{3.52}$$

$$|\beta\rangle = \frac{\overline{\Omega}_R|0\rangle + \left(\Delta - \overline{\Omega}_{gen}\right)|+\rangle}{\sqrt{2}\sqrt{\overline{\Omega}_{gen}^2 - \Delta\overline{\Omega}_{gen}}} \tag{3.53}$$

$$= \frac{\overline{\Omega}_R|0\rangle + \left[\frac{\Omega_{R1}}{\overline{\Omega}_R}\left(\Delta - \overline{\Omega}_{gen}\right)\right]e^{-i\omega_1 t}|1\rangle + \left[\frac{\Omega_{R2}}{\overline{\Omega}_R}\left(\Delta - \overline{\Omega}_{gen}\right)\right]e^{-i\omega_2 t}|2\rangle}{\sqrt{2}\sqrt{\overline{\Omega}_{gen}^2 - \Delta\overline{\Omega}_{gen}}} \tag{3.54}$$

At zero detuning for both transitions, the eigenstates $|\alpha\rangle$ and $|\beta\rangle$ are equal mixtures of the ground and $|+\rangle$ states, with the components being in phase for $|\alpha\rangle$ and π out of phase for $|\beta\rangle$. For weak fields or large detuning, the eigenenergies approach the energies E_0 (the zero point), E_1, and E_2. For interactions with $\overline{\Omega}_R \gg \Delta$, the energy splitting approaches $\hbar\overline{\Omega}_R$, which in the case of equal Rabi frequencies exceeds the individual two-state Stark splitting by a factor of $\sqrt{2}$.

The switch we made from the optical frequency "a" variables to the slow "c" variables was equivalent to reducing E_1 and E_2 by their ground-state transition energies.[4] If we put the optical frequencies back into the picture, we get the energy diagram of Figure 3.3. This diagram shows the formation of Rabi sidebands that are the same for each transition. For nonzero equal detuning, there is also a Stark shift similar to a two-level system with detuning Δ. One can see from the diagram that any time the detunings are equal, it is possible to transfer population between

---

[4]E_1 and E_2 are eigenenergies of H_0. Without the applied fields, their phases advance as $e^{-i\mathsf{E}_j t/\hbar}$ as appropriate for any stationary state. The substitutions of equations 3.14 and 3.15 slow the phase by an optical frequency, e.g., under the influence of H_0 only, $a_1(t) = a_1(0)e^{-i\mathsf{E}_1 t/\hbar} = c_1(t)e^{-i\omega_1 t}$, resulting in $c_1(t) = a_1(0)e^{-i(\mathsf{E}_1/\hbar - \omega_1)t}$, which shifts the energy by $\hbar\omega_1$.
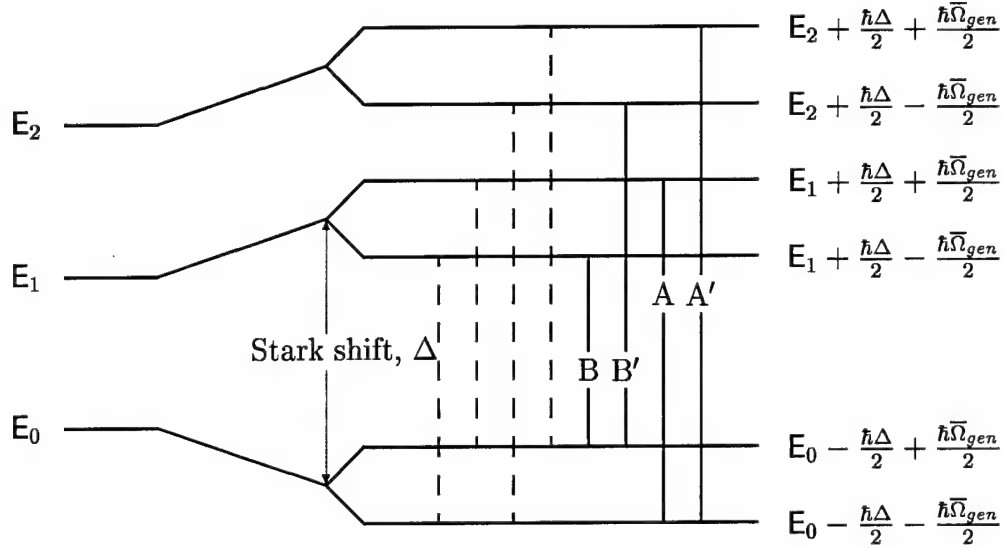
Figure 3.3: Schematic diagram showing the Stark shift and Stark splitting of the three-state system. The system energies without the light fields are shown on the left, and the energies with the light fields are shown on the right. Dark transitions are indicated by dashed lines and possible optical transitions are shown by solid lines. The two-photon processes A–A′ and B–B′ are Raman-type transitions between exciton states. Detuning Δ is assumed positive—a blueshift always results.

the excited states by a two-photon Raman-type transition. This coupling results in the intervalence-band coherence which allows for the interference that creates the dark state.

3.8   Coupled Stark shifting

If one of the two electric fields is negligably weak and broadband, then the above analysis in terms of equally detuned pumps is obviously not applicable. However, since the analysis of the equally detuned three-state system degenerates to the consideration of two dressed states, the results are easily adapted to the case of a single pump near resonant with one transition. In this case, the energy levels that belong to the strongly driven transition (E_0 and E_1) will be split and shifted as in Figure 3.3, but with a generalized Rabi frequency $\sqrt{\Omega_{R1}^2 + \Delta^2}$ instead of $\overline{\Omega}_{gen}$. For detunings that are large compared to the Rabi frequency, this reduces to a Stark shift of

the resonance by $\Omega_{R1}^2/2\Delta$.[5] Thus the optical Stark shifting is proportional to the intensity and inversely proportional to the detuning in this limit.

A transition to energy level E_2 is assumed far enough off resonance so that E_2 remains unaffected. However, E_0, which is involved in the transition to E_2, has been shifted to an energy $\hbar\Omega_{R1}^2/4\Delta$ lower. This results in a Stark shift of the nonresonant transition that is half of the shift of the near-resonant transition. This shift should be measurable by the broadband probe.

In a semiconductor the actual response can be strongly influenced by many-body effects. For moderately large detunings, however, few real carriers are excited and many-body effects are minimized. One would expect that the results just derived would apply more accurately to larger detunings and smaller driving fields.

3.9 Semiconductor dark states

The analysis up to this point has treated the semiconductor as an ideal three-state "V" system. In this final section, we summarize the work of Lindberg and Binder [35], who analyzed the multiband semiconductor Bloch equations with respect to dark states. They write the Hamiltonian in terms of "dark" and "active" hole states, so we first must adapt our Hamiltonian, given by equations 2.49, 2.53, 2.59, and 2.61, to electron and hole operators.

The electron operator is identically the conduction band operator, though we change notation: $a_{\mathbf{k}}^\dagger = a_{c\mathbf{k}}^\dagger$. The creation of a hole in a valence band corresponds to the destruction of an electon in that band with opposite momentum, so we define: $b_{\nu,-\mathbf{k}}^\dagger = a_{\nu,\mathbf{k}}$, where the index ν indicates any of the hole states lh, hh, d (for dark), or a (for active).

Substituting our new definitions and restoring normal ordering using the appropriate commutators, H_0 becomes

$$H_0 = \sum_{\mathbf{k}} \left[\mathsf{E}_{e,k}^0 a_{\mathbf{k}}^\dagger a_{\mathbf{k}} + \Delta_{\mathbf{k}} \left(b_{hh,-\mathbf{k}}^\dagger b_{hh,-\mathbf{k}} + b_{lh,-\mathbf{k}}^\dagger b_{lh,-\mathbf{k}} \right) \right] \tag{3.55}$$

---

[5]The Stark *splitting* is not measurable in this limit because the wavefunctions for the dressed states are almost entirely the original states [36, pp. 222–223].

We have taken out the optical frequencies, which is reflected in the appearance of $\Delta_{\mathbf{k}}$ instead of the hole energies. We have also assumed equal detuning and equal curvatures in the two valence bands, so we can use a single $\Delta_{\mathbf{k}}$. We can make the same basis transformation as we did to get from $(c_0,\ c_1,\ c_2)$ to $(c_0,\ c_+,\ c_-)$ by making the associations $c_0 \to a_{\mathbf{k}}^\dagger$, $c_1 \to b_{hh,-\mathbf{k}}^\dagger$, $c_2 \to b_{lh,-\mathbf{k}}^\dagger$, $c_+ \to b_{a,-\mathbf{k}}^\dagger$, $c_- \to b_{d,-\mathbf{k}}^\dagger$ from equations 3.27, 3.28, 3.30, and 3.31. This results in

$$H_0 = \sum_{\mathbf{k}} \left[\mathsf{E}_{e,k}^0 a_{\mathbf{k}}^\dagger a_{\mathbf{k}} + \Delta_{\mathbf{k}} \left(b_{a,-\mathbf{k}}^\dagger b_{a,-\mathbf{k}} + b_{d,-\mathbf{k}}^\dagger b_{d,-\mathbf{k}} \right) \right] \tag{3.56}$$

In the electron, lh, hh basis, the interaction energy is given by

$$H_I = \sum_{\mathbf{k}} \left[\frac{\hbar}{2} \Omega_{R1} b_{hh,-\mathbf{k}} a_{\mathbf{k}} + \frac{\hbar}{2} \Omega_{R2} b_{lh,-\mathbf{k}} a_{\mathbf{k}} + h.c. \right] \tag{3.57}$$

using equations 2.61, 3.7, 3.9, 3.18, and 3.19. Making the transformation to the electron, active state, dark state basis in the same way as for H_0, we get

$$H_I = \sum_{\mathbf{k}} \left[\frac{\hbar}{2} \overline{\Omega}_R b_{a,-\mathbf{k}} a_{\mathbf{k}} + h.c. \right] \tag{3.58}$$

The essential point in this representation of the interaction Hamiltonian is that the dark state is not coupled to the light field. This result obtains, as we have seen before, from the cancellation of the dark state interaction terms, or destructive interference. Had we not assumed equal effective masses for the light and heavy hole valence bands, the dark state would not be an energy eigenstate for all $\mathbf{k}$ and hole number would not be conserved. In any real semiconductor, this will be the case.

The Coulomb interaction part of the Hamiltonian can be obtained with the same methods and much algebra. The basis transformation does not add much clarity to the our understanding of the interactions. The form is similar to equation 2.59; it consists of four operator products, in this case with dark and active holes and electrons, multiplied by $\tilde{V}^C(\mathbf{q})$ and summed over wave vectors. The full form is found in the Lindberg and Binder paper that this section follows, reference [35]. The essential feature of the Coulomb terms is that the dark and active holes interact, unlike the atomic three-state system.

Computations by Lindberg and Binder do show dark state behavior in a semi-conductor quantum well with GaAs parameters and a 40 meV *lh-hh* splitting. They assume an unscreened Coulomb potential and an excitation independent dephasing rate. They compute the spectrally integrated sample absorption with one pulse of fixed freqency and one pulse that is scanned. They find that the minimum absorption occurs at the equal detuning point, regardless of the detuning of the fixed pulse. This behavior is consistent with an intervalence-band coherence and cannot be explained by the other nonlinearities contained in the semiconductor Bloch equations.

Lindberg and Binder also computed effects due to two sets of two pulses, primarily based on the three-state system mimicking a two-state system due to the inactivity of the dark state. These computations are interesting in that they show behavior similar to the ideal three-state system but with marked differences. They note that "the density response ... depends sensitively on the specific parameter values, such as delay time and effective masses." The complications arising from the solid state appear to be significant even in theory; experiments may depend sensitively on factors that are not fully understood.

CHAPTER 4

CONCEPTS OF THE EXPERIMENTS

Either two- or three-state coherent transient behavior can occur in a three-state optical system, depending on the intensity and spectral characteristics of the light field. In fact, all three experiments described in this dissertation are nearly identical except for the characteristics of the light pulses. There are two electric dipole transitions in a three-state optical system,[1] and this is where our primary interest lies. For the Rabi oscillation experiment, one pulse was made resonant with each of the two transitions. The strong pump pulse created two-state density (Rabi) oscillations, while the weak pulse probed the oscillations by virtue of the shared conduction band. By greatly broadening the probe pulse spectrum and pumping nonresonantly, we measured the Stark shift of both resonances simultaneously to study directly the effect of the shared conduction band. The coupling of the Stark shifts is a three-state, single pump effect. With both electric dipole transitions pumped near resonantly with spectrally discreet intense pulses, we tried to create a transient coherence between the optically uncoupled states that could, in theory, result in dark states and a host of other intriguing effects. The Rabi oscillation and dark states experments described herein used two independent, nondegenerate pulses created from separate optical parametric amplifiers (OPAs), while the coupled Stark shifting experiment used one OPA and a supercontinuum pulse. By adding the supercontinuum probe pulse to the pump-pump scheme, we have recently expanded our capabilities to study the intervalence-band coherence.

For the two experiments with spectrally discreet pulses (Rabi oscillations and dark states) there is a deeper connection between two- and three-state behavior. We

---

[1]It is possible to create an optically excited three-state system with higher order electric or magnetic multipole transitions, but we do not do so here.

have seen that under the conditions for the existance of the dark state (equal detuning), the three-state system behaves like a two-state system with a Rabi frequency determined by the two light-field amplitudes and both electric dipole moments. This suggests that the behavior of one exciton resonance can be used to probe the behavior of the other exciton resonance. If the semiconductor behaves like an ideal three-state system, the semiconductor should exhibit two-state behavior for equal pulse detunings whatever the relative pulse intensities.

In fact, in the limit that one of the electric fields is negligably small (as in the Rabi oscillation experiments), the three-state system must behave as a two-level system with respect to the strong driving field only. Before the coherence decays, the system will oscillate at the generalized Rabi frequency derived from the strong field and the electric dipole moment it excites. Say, for example, that the light pulse which is near resonant with the E_0–E_2 transition is very weak, so that $\Omega_{R2} \to 0$. The dark state $|-\rangle$ approaches a very weakly interacting state $|2\rangle$ while $|\alpha\rangle$ and $|\beta\rangle$ become the dressed states of the two-state system.[2] The three-state dynamics for equal detuning still apply, so both occupation probability amplitudes (c_1 and c_2) oscillate at the three-state generalized Rabi frequency, which now approaches $\sqrt{\Delta^2 + \Omega_{R1}^2}$, the two-state generalized Rabi frequency for the strong transition. The weakly excited transition is now a probe for the strong transition. The apparent drawback to this approach is that the maximum probability for being in the lh-exciton state is proportional to the square of the ratio of the small and large Rabi frequencies (see equations 3.45 and 3.46) if both transitions are resonant. It gets even worse for pumping that is detuned from the transition energies.

Why is such a probe useful with this handicap? It is useful because the absorptance that we measure is the *fraction* of intensity absorbed, so while exciton occupation probabilities scale with the squares of their Rabi frequencies (which are proportional to applied optical field amplitudes), absorption coefficients scale with the squares of the dipole matrix elements, as usual. However, because of the large

---

[2]To show this is so, substitute $\Omega_{R2} = 0$ into equations 3.25, 3.52, and 3.54, use equation 3.28 with equation 3.25, and compare this to the two eigenstates derived using equations 2.29 and 2.30.

fraction of the ground state (no exciton) involved in hh-exciton Rabi oscillations, the lh-exciton absorption is affected both by oscillations in the ground state population and by its own oscillating probability of transition, as is shown in Section 4.4.

A reason not to directly measure the hh-exciton transmission to see Rabi oscillations is coherence decay. To time resolve oscillations that occur fast enough to beat the decoherence time, we cannot use electronics—we need a probe pulse. If we make the probe pulse resonant with the strong (pump) pulse, it is difficult to differentiate between the effect of the pump versus the probe. More importantly, it is difficult to differentiate between Rabi oscillations and the many other nonlinear effects contained in the semiconductor Bloch equations. Thus the two-color pump-probe is a useful technique to directly observe semiconductor Rabi oscillations.

Now let us consider what happens when we let the probe pulse become stronger so that its nonlinear effects on the system cannot be ignored. If we maintain equal detuning while increasing the probe pulse intensity, the synchronized Rabi oscillations theoretically become faster. When both individual (two-state) Rabi frequencies are equal, the probability amplitudes are the same for the occupation of both exciton states. With comparable populations of lh- and hh-excitons we expect the maximum probability of Raman-like transitions and the maximum intervalence-band coherence.

Although the oscillation frequencies will only be equal for the equal detuning condition that allows for a dark state, the existence of equal oscillation frequencies is not by itself evidence for dark states. In fact, the oscillation amplitudes are theoretically largest for an empty dark state. Atomic experiments that have demonstrated a nonradiative coherence include population trapping, electromagnetically induced transparency, lasing without inversion, refractive index enhancement, and quantum beats [10, Ch. 7]. The first four of these effects are generally done in a "Λ" system, either so that the system can start in a coherent superposition of two ground states or so that population can be transferred by spontaneous emission or adiabatic transfer. Both creation of the "Λ" system and enabling population transfer present challenges in semiconductors. Quantum beats were observed by Ferrio

and Steel in 1997 [37] but, unlike the other four effects, quantum beats can exist without population in the dark state. A demonstrated decrease in absorption that peaks at the equal detuning condition would be direct evidence, and was the object of our dark states experiments.

4.1 Two-color pump-probe concept

We did the Rabi oscillation and coupled Stark shifting pump-probe experiments with non-collinear pulse trains (see Figure 4.1). The light-hole and heavy-hole exciton resonances of the samples were spectrally split by an amount determined by the composition and growth conditions of the quantum wells. In the Rabi oscillation experiment one of the pulse trains was near resonant with each of the two exciton resonances, while in the Stark shifting experiment the pump pulse train had a narrow spectrum near resonant with the hh-exciton and the probe pulse train had essentially a continuous spectrum. In both experiments we spectrally narrowed the pump pulse which had the additional effect of stretching it temporally. The probe pulses had to remain temporally short to time gate the interaction.

By using the non-collinear geometry, we somewhat diminished the problems associated with spectral overlap of the two pulse trains. In this geometry one measures only the probe pulse beam, which is spatially well separated from the pump pulse beam some distance from the sample. For the thinner sample that we used for the Rabi oscillation measurements this was sufficient to isolate the measurement to the probe beam so that the small spectral overlap was not a problem, although the spectral width of the probe did require us to integrate over the range of detunings. The thicker sample that we used for the Stark shifting experiments scattered a considerable amount of pump light which had to be accounted for in the data analysis.

We have the capability to vary the pulse spectral widths with a pulse shaper for each pulse train. The apparatus is described in the next chapter. For the Rabi oscillation experiment, we had to keep the probe pulse duration to a fraction of a Rabi oscillation period to time resolve the oscillations. This meant that it had to
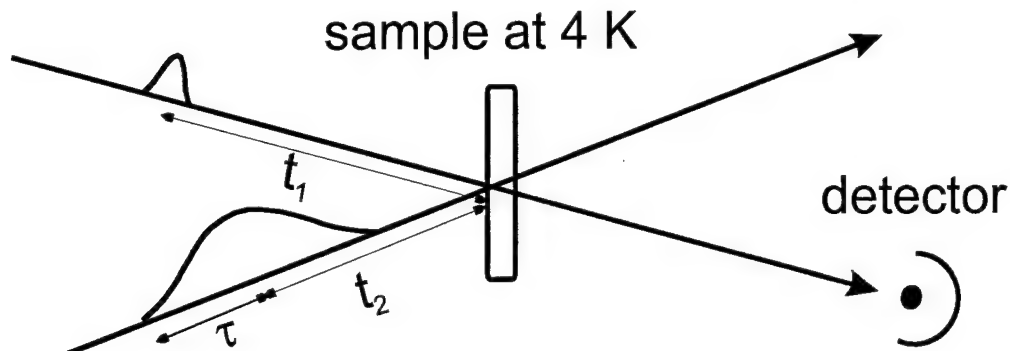
Figure 4.1: The two-color pump-probe concept. The upper pulse, which is shown at time t_1 before arriving at the sample, is a 150 fs duration weak probe, which was near resonant with the *lh* exciton transition for the Rabi osciallation experiments and very broadband for the Stark shifting experiments. It is measured with and without the pump to get a differential transmission spectrum (DTS). The lower (pump) pulse is 800–1200 fs in duration and about two to three orders of magnitude stronger than the probe. It is shown at a time t_2 before arriving at the sample and is near resonant with the *hh* exciton resonance. The delay $\tau = t_1 - t_2$ is varied with a delay line to time resolve the pump-sample interaction.

be around 200 fs or less. We narrowed the probe spectrum only a little or not at all to keep the short duration. Since the Stark shifting measurements relied on a supercontinuum pulse train, there was no spectral shaping of the probe pulse except for the addition of edge filters where unwanted light was causing problems. When we looked for Rabi oscillations in samples with a smaller *lh–hh* splitting, we found it necessary to narrow the probe pulse spectrum significantly to keep it nonresonant with the heavy hole exciton.

We did not need ultrashort pulses in either experiment for the pump beam. The upper limit to the useful duration of the pump beam was determined by the dephasing time of the semiconductor sample. The probe pulse "time gated" the interaction with its short duration, and we were able to look at integrated time slices of the interaction through the probe. The integration time was determined only by the short probe. This was very useful for the Rabi oscillation experiments. The number of Rabi oscillations was determined by the time integrated Rabi frequency, the dimensionless "pulse area" examined in Subsection 2.3.3. As we changed the relative pump-probe delay, we were adding to the pulse area that had passed prior

to the arrival of the probe. As the excitation density increases, so does the decay rate. By keeping the intensity lower by stretching the pulse energy out over a longer time, we kept the excitation density lower and increased the decay time. The hh exciton was excited far enough off-resonance in the coupled Stark shifting experiments that negligably few real carriers were generated. Thus the transient Stark shifts adiabatically followed the pump pulse, and the relatively short duration probe was able to resolve that behavior.

4.2   Two-color pump-pump concept

For the dark states experiments, both pulse trains played a more or less equal role (see Figure 4.2). The key distinction between two-state and three-state behavior (i.e., nonradiative coupling) is theoretically largest when the two transitions have equal Rabi frequencies. The interaction that has the smaller oscillator strength (which is proportional to the square of the dipole matrix element) can be compensated for by using a more intense pulse on that resonance. Equal frequency Rabi oscillations of the two exciton densities should occur when the Raman-transition condition is met, as well as a transient decrease in overall absorption. Because of the spectral symmetry of the response, it is desirable to observe the behavior of the semiconductor at both exciton resonances.

The decisive evidence for or against the existance of a dark state in a semiconductor would probably be based on the coherent behavior of the system with repect to detuning. The oscillations should be smaller (or, if Rabi oscillations could not be resolved, the absorption should be smaller) if the semiconductor were in a superpositon of states that included a dark state component. Experiments have shown conclusively that this occurs at the equal detuning condition for atomic systems [12]. In a semiconductor, we believe that the total absorption of both pulses would be less with some of the exciton population (in the noninteracting basis) destructively interfering so that they could not interact with the light, which is the mechanism for dark states. No other known nonlinearity depends in the same way on the detuning.

Unfortunately, a null result would be difficult to sell. First of all, it may be
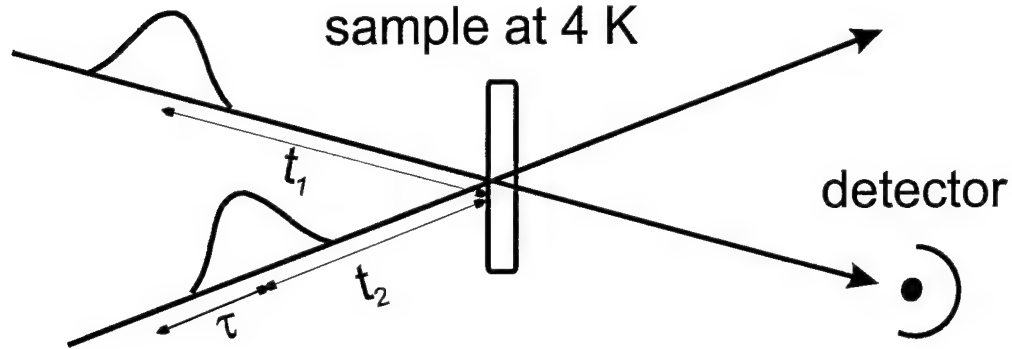
Figure 4.2: Pump-pump concept. The two pulses are of near equal intensity, one near resonant with each of the two exciton transitions. They are shown here in a non-collinear geometry, but can be measured in a collinear geometry since they are spectrally split. The transmission of the pulse near the *lh*-exciton is theoretically largest when the *hh*-exciton pulse is equally detuned, due to the creation of a dark state. The *hh*-exciton pulse is tuned to test this behavior and the delay is changed to identify coherent behavior.

possible that the amplitude of the dark state is very small; perhaps a different experiment could put more population in the dark state. Secondly, dephasing times are fast, carrier density dependent, and not well known; the dark state might not be detected due to loss of coherence. Thirdly, fluctuations in the light source could be obscuring the signals or changing the detuning and/or Rabi frequency from pulse to pulse. Lastly, it could just be that a different semiconductor structure, different semiconductor materials, or different material engineering is needed. At best, a null result would indicate that we either cannot create or cannot prove dark states exist within the limitations of our laser system, semiconductor materials, and measurement apparatus.

Since we believe it is better to observe both pulses, we usually did the dark states measurements in a collinear geometry. Other than the pulse characteristics, this was the only significant difference between the dark states experiments and the two-band Rabi oscillation experiments. If we were to vary the intensity of one pulse continuously from much weaker to much stronger than the other, and maintain equal detuning, the joint oscillation frequency of the two transitions would change from the generalized Rabi frequency of one pulse, to a sum in quadrature, to the

generalized Rabi frequency of the other.

With two strong pulses in the dark states experiments, we do not have a probe to time gate the interaction. Without a probe, it is impossible to see the Rabi oscillations and we had to look directly for an increase in transmission to reveal a decrease in absorption. We had to make both pulses short, about the same duration as the decoherence time or shorter, so that we did not collect a large background of light that had interacted with an incoherently excited semiconductor. The goal then was to make the pulses spectrally narrow enough so that they did not overlap both exciton resonances, but temporally remain within the coherent time span. We varied the overlap of the pulses to distinguish between coherent and incoherent effects, and we varied the detuning to see if absorption changes were consistent with the dark state.

4.3   Two-color pump-pump-probe concept

An improvement over the two-color pump-pump concept is the two-color pump-pump-probe configuration, which may be unique to our lab. For the pump-pump-probe setup we simply added a broadband probe that makes a three-way intersection with the two pump pulses inside the sample. In practice, we did this by putting a microscope slide immediately after the sapphire crystal in one of the OPAs to reflect a small portion of the white light supercontinuum (for a discussion of the OPA, see Section E.5 and Figure E.4). The supercontinuum probe pulse path length is varied using a delay line to time resolve the two-color pump-pump interaction with the semiconductor. The relative delay of the two pumps is also adjustable.

In our initial measurements with this setup, we first got maximum overlap of the two pumps using cross-correlation in a BBO crystal. We put the sample at the intersection as accurately as possible and cooled the sample to 4.2 K. We then adjusted the probe pulse to overlap with the lh-exciton pump pulse by looking for hh-exciton bleaching, remembering to use the correct probe polarization. Next, we overlapped the hh-exciton pump by looking for lh-exciton bleaching. An accurate determination of the temporal probe overlap can be ascertained using the nonlinear

response of the sample itself. Our initial measurements have not been fully analyzed yet.

4.4 Ideal three-state optical response

The coherent optical response of the semiconductor is complicated by significant many-body interactions (the subject of Reference [38]). Insight into these effects is, in fact, one of the chief objectives of our studies of coupled Stark shifts and semiconductor Rabi oscillations. First, however, we will examine the three-level optical Bloch equation response that neglects the many-body interactions. We will call the objects of interest "atoms" as a shorthand for the semiconductor in the one- or two-particle picture while neglecting the exchange interactions.

The optical response of a material derives from the polarization induced by the applied electric field. For a density of N atoms per unit volume, initially in the ground state, that do not interact except through collisions, the coherent polarization is given by

$$\mathbf{P}(t) = N\overline{\langle \mathbf{d} \rangle}, \tag{4.1}$$

with $\overline{\langle \mathbf{d} \rangle}$ determined as in equation 2.28, repeated here with different labeling for convenience:

$$\overline{\langle \mathbf{d} \rangle} = \rho_{ba}\mathbf{d}_{ab} + c.c. \tag{4.2}$$

We are interested in the polarizations derived from the lh-exciton resonance and the hh-exciton resonance, which we will label $\mathbf{P}_2(t)$ and $\mathbf{P}_1(t)$ respectively. A complication arises from our use of a three-state system, namely that the density of atoms associated with each of the two two-state resonances varies with time. By this I mean that both exciton resonances share the same ground state (the unexcited semiconductor) which is depleted by a transition to either exciton state. Furthermore, an electron-hole pair in one of the exciton states can be moved to the other exciton state through a two-photon Raman-type transition. This is reflected in coherence between the two excited states, the so-called intervalence-band coherence.

We will try to include this in an approximate way by considering N to vary with time and the polarization to follow adiabatically. The energy levels we will use in the following arguments are as labeled in Figure 3.2.

Since we are concerned with a coherent system, we can compute the needed density matrix elements from the three-level solutions of equations 3.42, 3.45, and 3.46 while additionally using equations 3.13 through 3.15. Assuming zero detuning for simplicity, we get

$$\rho_{10} = a_1 a_0^* = -i\frac{\Omega_{R1}}{\overline{\Omega}_R}\sin\left(\frac{\overline{\Omega}_R}{2}t\right)\cos\left(\frac{\overline{\Omega}_R}{2}t\right)e^{i\omega_1 t} \tag{4.3}$$

$$\rho_{20} = a_2 a_0^* = -i\frac{\Omega_{R2}}{\overline{\Omega}_R}\sin\left(\frac{\overline{\Omega}_R}{2}t\right)\cos\left(\frac{\overline{\Omega}_R}{2}t\right)e^{i\omega_2 t}. \tag{4.4}$$

We start by treating these coherences coequally, as in the dark states experiment, and then specialize to a pump-probe relationship appropriate to the Rabi oscillations measurements.

Using the label $j = 1, 2$ for states $|1\rangle$ and $|2\rangle$, we get the following expression for the polarization at frequency ω_j:

$$\mathbf{P}_j(t) = -iN_j\mu_j\frac{\Omega_{Rj}}{2\overline{\Omega}_R}\sin\left(\overline{\Omega}_R t\right)e^{i\omega_j t}\hat{\sigma}_\pm + c.c. \tag{4.5}$$

As before, μ_j is the magnitude of the dipole moment, and its direction is either $\hat{\sigma}_+$ or $\hat{\sigma}_-$. The complex polarization $\mathcal{P}_j$, defined by

$$\mathbf{P}_j(t) = \mathcal{P}_j e^{i\omega_j t}\hat{\sigma}_\pm + c.c. \tag{4.6}$$

is related to the absorption coefficient α_j (with $\mathcal{P}_j \ll \mathcal{E}_j$) by[3]

$$\alpha_j = \frac{\omega_j}{n_b c\epsilon_0}\mathsf{Im}\left\{\frac{\mathcal{P}_j}{\mathcal{E}_j}\right\}, \tag{4.7}$$

with n_b representing the background refractive index (about 3.6), c being the speed of light, ϵ_0 being the permittivity of free space, and $\mathcal{E}_j$ being the complex elecric

---

[3]See, for example, Reference [36, p. 202]. More generally, $\mathsf{Im}\{\mathcal{P}_j/\mathcal{E}_j\}$ should be replaced by $2\mathsf{Im}\{\sqrt{1 + \mathcal{P}_j/\mathcal{E}_j}\}$; we have taken the first complex term of the Taylor's series expansion.

field envelope as defined in equation 3.1. Extracting the complex polarization from equation 4.5 and using equation 4.7, we derive an absorption coefficient

$$\alpha_j = N_j \frac{\mu_j^2 \omega_j}{\hbar n_b c \epsilon_0} \frac{1}{\overline{\Omega}_R} \sin\left(\overline{\Omega}_R t\right). \tag{4.8}$$

If both transitions have similar coupling strengths (or Rabi frequencies), both excited states will have similar populations. When $\overline{\Omega}_R t = 2n\pi$ with integer n, the ground state is full and there is no excited population. The lh- and hh-exciton states are simultaneously populated to comparable levels. For both transitions, N_j changes at the same rate, reaching a maximum at the full ground state and a minimum when $\overline{\Omega}_R t = (2n+1)\pi$. The population in the dark state does not participate in this synchronized Rabi flopping. The sum of these effects is that: (1) the amplitude of either (lh or hh) absorption oscillation is similar to a two-state system with a Rabi frequency of $\overline{\Omega}_R = \sqrt{\Omega_{R1}^2 + \Omega_{R2}^2}$, (2) the oscillations are not exactly sinusoidal due to the non-conservation of population for each of the two resonances, (3) the absorption oscillation amplitudes are reduced by dark state population, which along with damping results in lower integrated absorption.

In the pump-probe case, we have $\Omega_{R2} \ll \Omega_{R1}$ and $\overline{\Omega}_R \approx \Omega_{R1}$. Nearly all of the population goes into the heavy hole exciton state, which oscillates to good approximation as a two-level system. We can approximate that $N_1 = constant$ throughout the process, as an appreciable number of atoms are not removed from the hh transition two-state system:

$$\alpha_1 = N_1 \frac{\mu_1^2 \omega_1}{\hbar n_b c \epsilon_0} \frac{1}{\Omega_{R1}} \sin\left(\Omega_{R1} t\right). \tag{4.9}$$

The lh exciton resonance oscillates at the same frequency, as can be seen by substituting the appropriate labels into the absorption equation using our pump-probe approximation,

$$\alpha_2 = N_2(t) \frac{\mu_2^2 \omega_2}{\hbar n_b c \epsilon_0} \frac{1}{\Omega_{R1}} \sin\left(\Omega_{R1} t\right), \tag{4.10}$$

but $N_2(t)$ somewhat alters the oscillation from sinusoidal. Taking $N_2(t)$ as $1 - \rho_{11} \approx$

$\cos^2(\Omega_{R1}t/2)$, we have

$$\alpha_2 = \frac{\mu_2^2 \omega_2}{\hbar n c \epsilon_0} \frac{1}{\Omega_{R1}} \left[\frac{1}{2} \sin\left(\Omega_{R1}t\right) + \frac{1}{4} \sin\left(2\Omega_{R1}t\right) \right]. \tag{4.11}$$

This resonant alteration of the sinusoidal oscillation is worse than we should expect in our experiments because we have inhomogeneous broadening and a finite pulse spectral width. The result just derived is shown in Figure 4.3, and is still clearly an oscillation at the hh-resonant Rabi frequency.
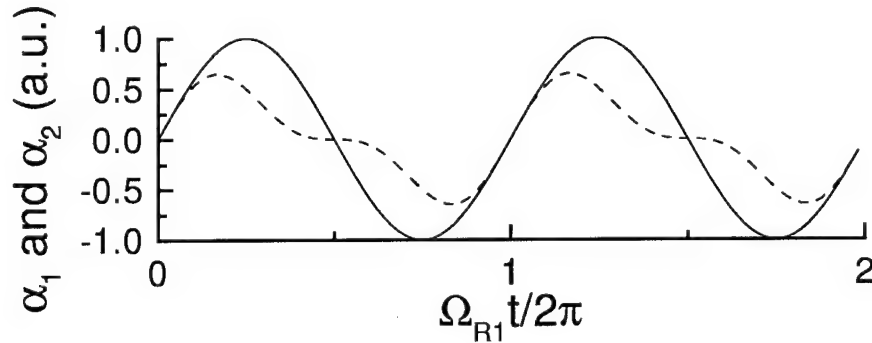

Figure 4.3: Rabi oscillations in the optical signal at the pump pulse (solid line) and the probe pulse (dashed line). The calculations shown here are for the idealized three-state system used as a probe of two-state Rabi oscillations. The relative absorptions should also be scaled by their respective oscillator strengths.

In the experiments we measure transmission. Light that enters the sample is either absorbed, reflected, scattered, or transmitted. The absorption is that which we have just calculated for the ideal three-state system. Reflection derives from a combination of the background index of refraction due to the core ions and electrons and the changes due to the active electrons. While the maximum changes in the refractive index occur at absorption resonances, there is little change at the absorption peaks (see any elementary derivation of the optical response of ordinary matter to light, such as Reference [39, pp. 90–98]). Since we are not looking to fit lineshapes, we approximate reflection from the background refractive index. Scattering occurs from sample inhomogenieties, which we neglect. With these assumptions, transmission assumes a constant value minus the absorption.

4.5   Semiconductor optical response

The discussion above, which applies to the three-state OBE density matrix elements, also applies to the three-state SBE, albeit with many-body modifications. With its $\mathbf{k}$-dependent energy bands, the semiconductor polarizations at ω_j become

$$\mathbf{P}_j(t) = 2\frac{1}{L^3}\sum_{\mathbf{k}}\left[P_{cv_j}(\mathbf{k},t)\mathbf{d}_{v_jc}(\mathbf{k}) + c.c.\right]. \qquad (4.12)$$

Here we have used the subscript v_j to represent either the lh or hh valence band, whichever applies. The sum over $\mathbf{k}$ and the division by the crystal volume L^3 take care of the atom density, but the partitioning of excited electrons between the two polarizations is still necessary and still affects the optical response as in the last section. To rigorously derive the semiconductor response, it is necessary to compute the general three-state semiconductor equations of motion, as the polarizations cannot be considered separately due to the intervalence-band coherence. This must be done numerically.

It is worth repeating that the application of the two- and three-state models to the semiconductor relies on the similarity of the OBE to the SBE (see Subsection 2.4.5). The absorption depends on the coherences which in turn depend on the populations. The differences between the equations for $P_{cv}(\mathbf{k},t)$ (2.77) and for $\rho_{21}(t)$ (2.33) are due only to many-body effects. The differences most readily seen in our experiments are the bleaching due to Pauli blocking,[4] which we are not interested in, and the renormalization of the Rabi frequency, which we are.

The total density of excited electons is related to the electron population by

$$n_e(t) = 2\frac{1}{L^3}\sum_{\mathbf{k}} f_e(\mathbf{k},t). \qquad (4.13)$$

Similar equations apply to the densities of light holes and heavy holes. Although the SBE are given as functions of $\mathbf{k}$, the polarization involves a sum, so it is the total densities that apply to the optical response. Since each particular $\mathbf{k}$ corresponds to

---

[4]Screening also causes some bleaching, but it is not included in the SBE in the form we have derived.

a different detuning, there will always be a range of Rabi oscillation frequencies in the optical response and a complete inversion is impossible.

In Subsection 2.4.6 we showed how the exciton develops from the single particle SBE in the limit $f_e = f_h = 0$. The result was the same as we derived in Chapter 1 from a consideration of an electron-hole (two particle) wavefunction. This is our justification for using the SBE while talking about a two particle "V" system. However, the pump pulses take the crystal out of the low-excitation limit, and the crystal excitations must deviate from the hydrogen-like exciton model. This is important since the deviations from the ideal exciton are due to the many-body "exchange" interactions that we are interested in exploring [38].

For an ideal (hydrogen-like) two-dimensional 1s exciton, the probability density of the relative electron-hole separation must be given by the square modulus of the 1s wavefunction. This is a result of the Wannier equation. Hankel transformed to k-space, this distribution is given by

$$\tilde{\psi}(k) = \frac{a_B^2/2}{\left(1 + \frac{k^2 a_B^2}{4}\right)^2},$$ (4.14)

where a_B is the exciton Bohr radius. This distribution can be compared to the carrier distribution functions $f_{e/h}(\mathbf{k}, t)$ obtained from the SBE; the differences should reflect the deviation from ideal excitons. R. Binder made such calculations for the sample parameters applicable to the Rabi oscillation experiments; he found significant deviation from the excitonic distribution for the strongly pumped hh resonance, but not for the lh probe resonance [38].

4.6 Creating the three-band system

Notwithstanding the heuristic model of the exciton as a hydrogenic quasi-atom, we cannot easily create a two- or three-state system in a semiconductor using the states of the exciton envelope. If we did, we would need light with a wavelength of around 10–100 μm, since the exciton Rydberg energy is two to four orders of magnitude smaller than the hydrogen Rydberg energy (13.6 eV, λ=91 nm) [31, pp. 162–163].

We would also need a second energy source (laser) to create the excitons. However, for $n > 1$ the exciton resonances are generally not well enough resolved to be isolated and are not spectrally separated enough to use the sub-ps pulses necessary to beat the dephasing time. Furthermore, first-class dipole-allowed transitions only occur between wave functions where $\Delta l = 0$ for the exciton envelope, while the photon carries an angular momentum of $l = 1$ in the dipole approximation [4, pp. 142–155]. This rules out the use of (generally) much stronger first-class transitions for exciton envelope transitions. For the right wide-band semiconductor, such as Cu_2O, it is possible to use exciton envelope states to create a three-state system as in the resonant Stark shifting experiments of Frölich *et al.* [40]. It is more useful for our purposes, however, to use exciton states deriving from three different bands.

4.6.1 The use of exciton states

The advantage that exciton states have over continuum states is that they are discreet resonances. It is, by definition, impossible to isolate states in a continuum. Although Rabi ocillations have been observed in the continuum [41], they were definitely complicated by the absence of isolated transitions. It is hard to imagine how three-state behavior could be manifest by the continuum states.

The Wannier exciton envelope for light induced electric dipole transitions has no angular momentum [7, p. 194]. A single light quantum carries a z-component of angular momentum of $\pm\hbar$ which corresponds to an intrinsic angular momentum of $s = 1$ [42, p. 275]. Since this angular momentum cannot go into the exciton envelope, the angular momentum of the atomic parts of the exciton wavefunction ($u_{\nu_e0}(\mathbf{r}_e)$ and $u_{\nu_h0}(\mathbf{r}_h)$ of equation 1.3) must change by $\Delta l = \pm 1$. Therefore we should look for $\Delta l = \pm 1$ between the valence and conduction band states. Furthermore, since binding energy is inversely proportional to the principal (exciton envelope) quantum number ($1/[n-(1/2)]^2$ for 2-D)[4, pp. 141, 213], we must limit ourselves to the lowest energy excitons to get adequate spectral separation between resonances.

So long as the tight binding approximation holds, the energy bands arise from the energy levels of the isolated atoms [43, p. 247]. In this case, the spatial configu-

rations, degeneracies, and selection rules for the circularly symmetric atomic system apply. We cannot assume this is always the case; it fails for most metals and some semiconductors. The determination of the band structure is often involved and is beyond the scope of this research.

Semiconductors that exhibit T_d (zinc-blende) or O_h (diamond) point group symmetries crystallize into structures with p-like valence bands and s-like conduction bands [31, p. 135]. The C_{6v} (wurtzite) semiconductors are similar but with lower symmetry. Transitions between valence and conduction bands in these materials obey $\Delta l = \pm 1$, as needed. It is still necessary to reduce the six degenerate p-like bands and two degenerate s-like bands to a three-band system.

4.6.2 States of the InGaAs/GaAs multiple quantum well

We have done our experiments with InGaAs/GaAs multiple quantum wells for a number of reasons including sample quality, convenient wavelength, sample engineering, and sample availability. The quantum wells are made of 8–9 nm of the tertiary compound $In_x Ga_{1-x} As$, and the barriers are 66 to 92 nm of GaAs. There are ten to twenty periods. Some samples also have C-doped GaAs substrates.

The bonding in GaAs, InAs, and InGaAs is primarily covalent with some ionic character, as is common to III-V compounds [6, p. 387]. The bands arise from sp^3 hybridization of the highest energy levels of the isolated atoms [31, p. 128][4, p. 172]. The lowest energy antibonding level is s-like and twofold degenerate. It is the lowest conduction band, and is empty in the ground state. Three gallium electrons and five arsenic electrons (per lattice site) fill the bonding levels in the ground state; six of these form the highest energy valence band, which is p-like.

The electron has intrinsic angular momentum, or spin, of 1/2, which results in a magnetic moment. If the electon has orbital angular momentum, it will feel a magnetic force called the spin-orbit interaction [28, pp. 73–77]. The eigenstates of the system become functions of the total angular momentum[5] J and its projection[6]

---

[5] J assumes integer values between $L + S$ and $L - S$, i.e. $+3/2$ and $+1/2$

[6] Values for m_J range from $-J$ to J.

m_J. Due to the spin-orbit interaction, the two $J = 1/2$ states are sufficiently split from the four $J = 3/2$ states that they can be ignored for our purposes.

The four remaining valence bands separate into two twofold degenerate bands away from the Γ-point. This can be derived from degenerate $\mathbf{k \cdot p}$ perturbation theory [7, p. 48–51], resulting in the Luttinger Hamiltonian and the Luttinger parameters. In the parabolic band approximation, the lifting of the degeneracy amounts to a heavier effective mass for the $m_J = \pm 3/2$ (hh) band relative to the $m_J = \pm 1/2$ (lh) band, which is quantified by the Luttinger parameters.

When a semiconductor is made thin enough to quantum confine its wavefunction, the energies associated with the confinement direction are those of the finite square well. This is the essence of a quantum well. Since these energies are inversely proportional to the effective mass, the lh valence band is shifted to a higher energy than the hh valence band (the confinement energies are negative). The lh and hh valence bands are thus non-degenerate at the Γ-point in a quantum well, although there is an anticrossing where the states mix and then switch effective masses.[7] Near the anticrossing, the valence bands cannot be described by the original J and m_J and the selection rules break down. It is important that the exciton wavefunctions not include much of these mixed states so that the selection rules apply.

Nature and molecular beam epitaxy have reduced the system to three twofold degenerate bands. We can connect the valence bands with the conduction band by an optical (near infrared) interaction. In the next subsection we will make the final step in creating the three-state system, but we first examine the energies involved.

GaAs, InAs, and InGaAs are III-V compounds with different energy gaps. GaAs has a low temperature E_g of 1.52 eV compared to 0.43 eV for InAs [4, p. 133]. $In_x Ga_{1-x} As$ is somewhere inbetween depending on x. More important, however, is that GaAs and InAs have different lattice constants, which induces strain in the tertiary compound and changes the lh–hh splitting. For example, our $x = 0.04$ sample has a bandgap of 1.49 eV and a lh–hh splitting of 16.9 meV, while for $x = 0.10$ the bandgap is 1.44 eV and the splitting is 31.3 meV. The quantum well

---

[7]See, for example, References [7, pp. 63–66] and [31, pp. 144–146].

thicknesses are similar, so the splitting difference can be attributed mainly to the composition.

Generally, wider splitting is better for our experiments, and splitting increases (to a point) with indium concentration. However, the lh-exciton oscillator strength decreases with indium concentration. We believe this to be due to the hole confinement potential becoming shallower and the electon-hole overlap decreasing [44]. The samples we selected were a compromise between these effects.

4.6.3 Linking three states through light field polarization

We separate the two twofold degenerate valence bands and the single twofold degenerate conduction band into two equivalent three-band systems through selection rules and resonance. Only one of these systems interacts resonantly for a given choice of light polarization.
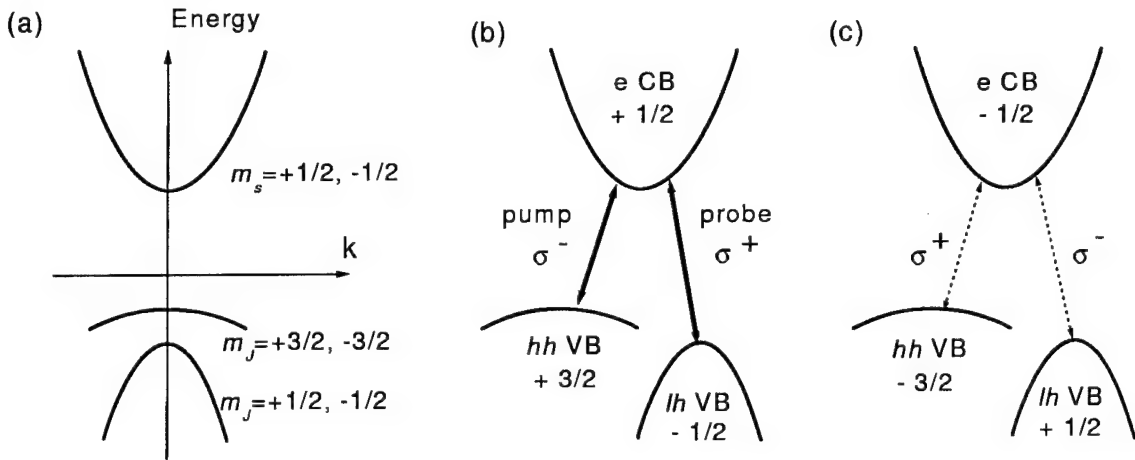

Figure 4.4: Optical coupling creates a three-band system: a) Schematic band structure in the effective mass and six band approximations. b) Transitions excited by the pump and probe pulses. Note that only three of the six bands are effectively coupled because of dipole selection rules for the near resonant transitions. c) There is actually some weak non-resonant dipole coupling of the other three bands that slightly complicates the experiment. The theoretical modelling accounts for all six bands, although to a good approximation the non-resonant coupling can be ignored.

We made one pulse train near-resonant with the lh-exciton resonance and the

other near-resonant with the *hh*-exciton resonance. For Rabi oscillations both were exactly resonant, but detuning was a parameter in the Stark shifting and dark states experiments. The pulse trains were circularly polarized in opposite directions. Either choice of polarizations is equivalent so long as they are counter-circularly polarized.

Take, for example, right-circularly-polarized light resonant with the *hh*-exciton resonance and left-circularly-polarized light at the *lh*-exciton resonance, which is the case we used for Chapter 3 (see Figure 4.4). The only non-zero electric dipole matrix element for the *hh* transition is between the $m_J = +3/2$ (*hh*) valence band and the $m_s = +1/2$ conduction band, while the only non-zero electric dipole matrix element for the *lh* transition is between the $m_J = -1/2$ (*lh*) valence band and the $m_s = +1/2$ conduction band. Both transitions share the same conduction band. For the opposite choice of circular light polarizations, the other three states participate and form their own three-band system. The pulse spectral widths are such that the non-resonant interactions should not be totally ignored, and they are included in the theoretical calculations by R. Binder and M. Lindberg that parallel this work.

CHAPTER 5

EXPERIMENTAL SETUP AND TECHNIQUES

All three sets of experiments, Rabi oscillations, coupled Stark shifting, and dark states, employ similar two-color excitations of coupled excitonic transitions, although the two-color label is debatable for the Stark shifting experiments. Therefore, the arrangements of devices to create and measure the desired interactions are quite similar. In this chapter, we examine how the experiments are done, concentrating first on pulse production, which is common to all of the experiments, and then on pulse manipulation, which varies with the particular experiment. We discuss in some detail the devices and techniques used in the experiments, and also describe intermediate measurements which are done to characterize the light pulses.

5.1   Experimental setup

The equipment used to conduct the experiments can be divided into two categories: (1) lasers and amplifiers which create the light pulses, and (2) devices which are arranged to create and measure the desired light-semiconductor interactions. A scale diagram of our complete non-collinear pump-probe setup, which is arranged on two optical tables connected by an optical breadboard, is shown in Figure 5.1. The equipment assigned to the first category is all contained on the upper table. The lasers and amplifiers are commercially produced by Spectra Physics and described only briefly in this section. The equipment on the lower table constitutes the second category.

5.1.1   Pulse production

The lasers and amplifiers that produce the light pulses all use solid state materials for optical gain. The system was installed in March 1998. A brief description follows,
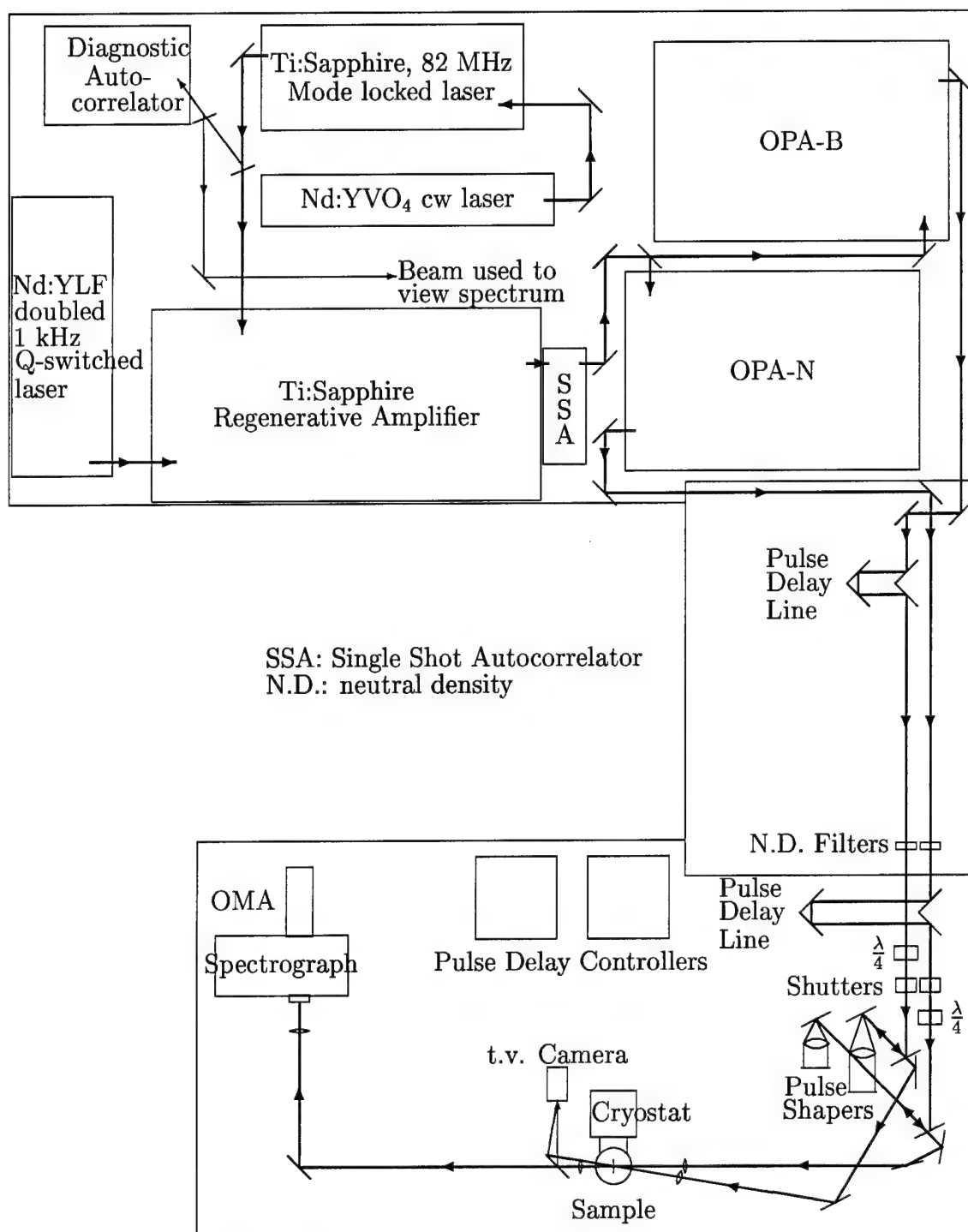
Figure 5.1: 1:20 scale diagram of the optical tables set up for pump-probe experiments. The upper table contains the light pulse source, i.e. lasers, regenerative amplifier, and OPAs. The lower table contains equipment to delay, polarize ($\lambda/4$), shape, overlap, focus, and measure the pulses, and also to cryogenically cool the sample.

with a more detailed description in Appendix E.

The heart of the system is a pair of dual-pass optical parametric amplifiers, nicknamed OPA-N (for Nasser) and OPA-B (for Bernard).[1] They each produce approximately 130 fs optical pulses at a repetition rate of 1 kHz, with pulse energies between 5 μJ and 70 μJ. This corresponds to a pulse power of 40-500 MW, and, if focussed to a 100 μm diameter spot, a huge pulse intensity of 0.5-7 TW/cm^2. The output can be either the signal or the idler pulse train from the optical parametric amplification process, which can be doubled twice, once, or not at all to create output wavelengths from about 290 nm to 2.9 μm. In all of our experiments we frequency double either the signal or idler pulse trains of one or both OPAs to obtain pulse wavelengths in the near infrared with 10-15 μJ/pulse. Precise wavelength selection occurs by rotating the BBO crystal (in which the optical parametric amplification occurs) to create phase-matching conditions for the desired output.[2]

The pump and seed pulse trains for both passes of both OPAs come from a single amplified "Tsunami" Ti:Sapphire mode locked laser. The Tsunami is tuned to produce 80 fs pulses at 82 MHz by active mode locking with an acousto-optic modulator (AOM).[3] While the laser will mode lock spontaneously and remain so for long periods, the AOM keeps the mode locking stable to prevent any cw laser output, which can damage an operating regenerative amplifier. We operate the Tsunami at about 450–550 mW average power (5.5–6.7 nJ per pulse), 800 nm central wavelength, and around 10–12 nm bandwidth.

One out of every 82,000 Tsunami pulses is amplified by the "Spitfire" regenerative amplifier, resulting in approximately 100 fs, 1 mJ pulses at 1kHz repetition rate. This output is evenly divided between the two OPAs by a beamsplitter. Within the OPAs, beamsplitters further divide the pulse trains into pre-amplifier (first pass)

---

[1]Having chosen these nicknames, it is perhaps fortunate that neither consistently outperforms the other.

[2]A classical theory of optical parametric amplification, essentially the same as difference frequency generation, is developed in references [45, pp. 409–411], [46, pp. 117-119], and [36, pp. 75–77]. Reference [45, pp. 421–425] also treats the subject quantum mechanically. Type II phase matching and angle tuning are covered in these same references and others.

[3]Mode locking and Q-switching are done with different types of AOM. An explanation of both uses of the AOM is found in [47, pp. 253–256,279–280] and [48, pp. 367,375].

and power-amplifier (second pass) pump beams and into seed beams. The seed pulse trains are spectrally broadened into "white light continuua" through nonlinear processes (primarily self-phase modulation) in a sapphire crystal,[4] thus creating tunability through the phase-matching condition mentioned earlier. For the coupled Stark shifting experiment we reflect about 4% of this broadband seed beam from the front surface of a microscope slide to use as a probe pulse train. Of course we lose another 4% from the back surface. The supercontinuum probe pulse train is directed out of the OPA through a window and guided to the sample with mirrors and lenses.

We can infer the Tsunami's temporal pulse width from an autocorrelator built by Dr. K. Wundke which measures the frequency doubled output of a Michelson interferometer (diagnostic autocorrelator in Figure 5.1). The operating principle of this autocorrelator is explained later in this chapter in Section 5.3. It is different from the autocorrelator used to characterize the OPA output pulses in that one arm of the interferometer is continuously scanned,[5] and the signal is measured by a photomultiplier tube and viewed on an oscilloscope. The Tsunami output has appoximately a bandwidth limited $\text{sech}^2(t)$ intensity distribution, so the autocorrelation FWHM is 1.543 times the pulse FWHM [49, p. 383].

The power of a Tsunami pulse is increased by about a factor of 2×10^5 in the Spitfire regenerative amplifier, but the repetition rate is decreased from 82 MHz to 1 kHz, a factor of almost 10^5. The repetition rate is governed by an AOM Q-switched Nd:YLF laser (Merlin) which pumps the Ti:Sapphire crystal of the amplifier. The regenerative amplifier itself is a laser cavity with Pockels cells, a quarter-wave plate, and polarizers to switch a pulse in and out of the cavity synchronized to maximize the gain (about 14 passes).

---

[4]This so-called supercontinuum generation is explained in References [49, pp. 144–145] and [50] The pulse beam appears white, although spectral measurements show that it is strongest between about 730 nm and 850 nm wavelengths. To seed the OPA signal, the supercontinuum must have spectral content between 800 nm and 1.1 μm wavelengths.

[5]A periodic voltage is applied to a piezoelectric transducer (shaker) which moves the mirror of one arm of the interferometer back and forth. The periodic voltage also drives the horizontal scale of the oscilloscope, making it proportional to mirror displacement.

Another important part of the regenerative amplifier is the pulse stretching which preceeds the amplification and the pulse compression which follows. The pulse is intentionally chirped by spectrally dispersing the light with a diffraction grating, causing different wavelengths to travel different distances. The pulse is stretched by about a factor of 1000. If this were not done, the pulse would damage the Ti:Sapphire crystal in the amplifier due to the extremely high peak power. By chirping the pulse, the energy is spread out over a longer time, so lower peak power results. The reverse process compresses the amplified pulse. Additionally, in order for the pulse compression to reverse the pulse stretching, the amplification must be linear; unlike other laser amplifiers, the gain medium is not pumped to saturation. Thus the regenerative amplifier is more sensitive to fluctuations in the pump laser than, for example, dye amplifiers.[6]

A frequency doubled, diode pumped $Nd:YVO_4$ (Nd^{3+} ion impurities in a yttrium vanadate lattice) cw laser pumps the Tsunami. In its first two and a half years of use, it has had to be repaired once. There is only one set of knobs that can be adjusted, which adjust a mirror, but we have not used them. The reader is again referred to Appendix E for details.

5.1.2 Pulse manipulation

Having briefly described the system which produces two trains of 130 fs pulses, we will now examine how those pulse trains are manipulated so as to have the desired pulses at the sample. We use optical delay lines to change the relative pulse overlap, neutral density filters to vary the pulse energy, Berek compensators to change the polarization from linear to circular, pulse shapers to reduce the spectral bandwidth and increase the temporal length, lenses to focus and overlap the pulses, shutters to block and unblock the beams, and an optical multichannel analyzer or CCD camera with spectrograph to measure the pulse spectra. We rearrange these components to get collinear or non-collinear pulse trains, pump-probe or pump-pump measurements, and co- or counter-circularly-polarized pulses. In this subsection, we describe

---

[6]A discussion of laser amplifiers is found in Chapter 6 of Reference [49].

both the operation of the equipment and how it is used in each experiment.

We use three mechanical delay lines to give us flexibility in arranging the temporal pulse overlap. Most of the time only the lowermost delay line of Figure 5.1 is moved to create time resolved data. The uppermost delay line in this figure is primarily used to take up any excess distance between the two paths. In particular, this delay line makes it easier to switch between collinear and non-collinear setups or to put a pulse shaper in or out of the setup. It is made from a one-dimensional translation stage; scrounged metal pieces, fasteners, and mirrors; and a New Focus "micrometer-replacement actuator" (i.e. a motor driven micrometer screw). The motor/actuator (along with other motors adjusting the bottom right mirror mount of Figure 5.1) is driven by a remote control box. With the addition of the supercontinuum probe, the controller for this delay line also has to be used to control a third delay line. The supercontinuum probe delay line, which is not shown in Figure 5.1, is similar to the one just described. The second delay line that is shown in Figure 5.1 is a stepper motor driven stage with 15 cm travel. It is controlled by the CC-1 Programmable Stepper Motor Controller from Klinger Scientific. Motion can be controlled over the GPIB computer interface to within 1 μm, which corresponds to a 6.67 fs change in pulse delay. To get time resolved data, we use a LabView computer program to drive this delay line between data points. During a long run of, say, ten picoseconds, the stage moves only 1.5 mm. The time resolution is not limited at all by this delay stage, but rather by the temporal width of the probe pulse ($\approx$150 fs). In the case of the Stark shifting and dark states experiments, the overlap served to distinguish coherent from incoherent effects.

It is important that the beam direction not change during delay stage movement, since a change in beam direction would probably result in a loss of pulse energy and would certainly change the overlap of the two pulse trains. To keep the delay lines true, they are carefully adjusted with light propagating much farther than it does during the experiments. The delay lines are adjusted so that a laser spot far from the delay line remains stationary throughout the entire range of delay line travel.

The pulse intensity is critical in our experiments. It can be changed through

both focusing and filtering, but the range of change attainable through focusing (or defocusing) is strongly limited by lens aberrations. We used neutral density filters with an optical density of between 0.05 and 4.0. Since the optical density is a logarithmic quantity, a series of filters adds algebraically ($10^{-\delta_1}10^{-\delta_2} = 10^{-(\delta_1+\delta_2)}$). Both the attenuation and the optical path delay of each filter must be known, since they cannot generally be measured during the experiments. A description of how they were measured along with the results are included as Appendix F.

Berek Polarization compensators are variable retarders (waveplates) that operate using the birefrigence of a uniaxial crystal [39, p. 694]. In such a crystal, orthogonal components of a light wave travel with different speeds through the crystal. If one component of a linearly polarized light wave is delayed a quarter period with repect to the other component, and both have equal magnitudes, the output is circularly polarized. In our experiments we use the Berek compensators to produce just this result, which makes the compensators act as quarter-wave plates for the desired wavelengths. The crystal properties which allow us to vary the retardation are the same as those which allow us to angle-tune in the optical parametric amplification process, and to phase match in the sum frequency generation and second harmonic generation processes which we use throughout the experiments.[7] The theory behind these techniques follows in Appendix A.

We use the Berek compensators in our experiments in two ways. In collinear experiments, such as the dark states measurements, we use the doubled signal from one OPA and the doubled idler from the other OPA. The second harmonic of the signal is vertically polarized and the second harmonic of the idler is horizontally polarized. Since the wavelengths of both are within 20 nm, we use one compensator to change the polarization of both beams. One becomes right-circularly polarized and the other left-circularly polarized since the fast axis of the compensator is at $+45°$ with respect to one beam and at $-45°$ with repect to the other. For the non-collinear experiments, this technique is not possible. Then we compensate each

---

[7]Our Berek compensators use MgF_2 crystals; all of the nonlinear wave mixing is done with $\beta - BaB_2O_4$, beta barium borate, or BBO.

pulse train individually.

For each of the two pulse trains we use a pulse shaper, which narrows the pulse spectrum and increases the pulse duration. The original pulse shaper was made by Dr. H. Giessen and is explained in detail in his Ph.D. dissertation, Reference [51, pp. 42–51]. We made the second pulse shaper with a similar design, but without the plate connecting the lens and mirror for simplicity. The concept of the pulse shapers is shown in Figure 5.2
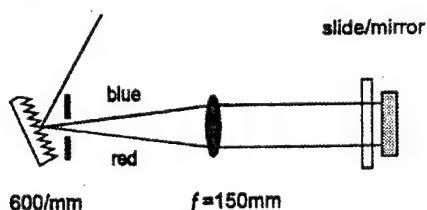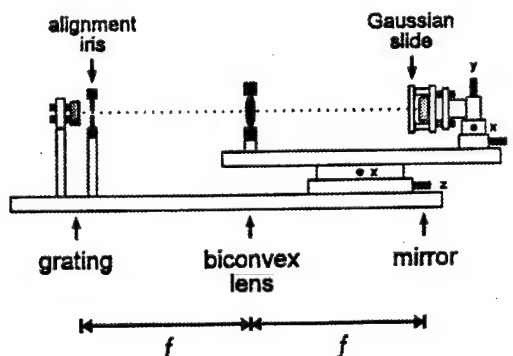

Figure 5.2: Dr. Giessen's pulse shaper design [51, p. 44]
(Top view) Operating principle of the pulse shaper: a diffraction grating disperses the incoming light, the light is collimated, the wings of the spectrum are attenuated by a Gaussian spatial filter, and the light reflected by the mirror undergoes the reverse process.
(Side view) Pulse shaper setup: The slide is made by exposing film with a TEM_{00} mode He-Ne laser beam. Our experience indicates that it would be better to make the slides of glass since the film creates interference friges.

The pulse shapers are very sensitive to the component spacing. We optimize the

alignment by using a second harmonic autocorrelation signal (Section 5.3) from the pulse shaper output. First we adjust the scanning arm of the interferometer to a position where the second harmonic signal from the two arms is at half maximum. We then minimize this signal by making fine adjustments to the lens and mirror of the pulse shaper, which has already been set near the correct separation. By iterating this process, we minimize the time duration of the pulses. When used for narrow spectra, the shaped pulses end up nearly bandwidth limited, but for wider spectra the chirp can be noticeable. Data showing the pulse spectra and autocorrelations achieved with various masks is included in Appendix G.

Lenses, filters, and mirrors would seem to be benign elements in the experimental setup, and they are to some degree, but there are some effects we must consider. The lenses and filters are made of glass and will chirp the pulses. Additionally, focusing can introduce chirp. Chirp is analyzed in Appendix B. The transverse pulse area on the sample (spot size) along with the pulse energy determine the pulse intensity. The spot size is determined by diffraction and lens aberration, along with the positioning of the sample relative to the focus. At a minimum, we must measure the spot size and energy. This is the subject of Section 5.4. The mirrors we use to manipulate the pulses are made of silver or gold. Dielectric mirrors are undesirable because none exist that are highly reflective over the 290 nm to 2.9 μm tuning range of the OPAs. It is useful to understand the effects of the metal mirrors to avoid undesired results.

One obvious effect of metal mirrors is that pulse energy is absorbed by Joule heating, which is unavoidable in metals. Each pulse is reflected off ten or eleven metal mirrors on its way to the sample. The reflectance is a function of the incident angle as well as the polarization. If we take a nominal refectance for silver of 97.5% for p-polarized light at 45°, we lose about 24% of the initial intensity due to absorption. This loss is completely unimportant, and we have orders of magnitude more intensity than is needed for the experiments.

The polarization change that can be induced by metals is, however, very important. Our intent is to convert linear polarization to circular polarization with the Berek compensators. Linearly polarized light is generally converted to elliptically

polarized light when reflected off a metal. Fortunately, there is a way out of this predicament. Light that is either s- or p-polarized will maintain its polarization after reflection. Thus we need to be careful that we use our mirrors so that the vertically or horizontally polarized OPA output pulses reflect off the mirrors as either s- or p-polarized. This condition is met so long as the pulses are redirected in a horizontal plane. Once the pulses have been converted to circularly polarized, they will gain some ellipticity by being reflected off a metal mirror.

The shutters are not triggered, so with any inaccuracy in their timing they can let through one pulse more (or less) than expected. Their response time is such that this error should not be more than a few pulses. With a typical run using a 100 ms exposure time for 50 shots, we get about 5000 pulses, so a few pulse variation due to the shutters can be neglected.

After the light interacts with the semiconductor, we measure the transmitted light. The full spectrum of interest is measured simultaneously on an optical multichannel analyzer (OMA) or CCD camera. Aspects of signal detection are covered in Section 5.5.

5.2   Testing of Berek compensators

Dispersion in its MgF_2 crystal prevents a Berek compensator from being a perfect quarter-wave plate for an entire pulse bandwidth. Furthermore, the concepts behind a Berek compensator are somewhat idealized, as in practically all actual devices. This section describes the experiments we did to examine the effectiveness of the Berek compensator for the wavelengths and bandwidths of our experiments.

We can gain insight into our OPA tuning, sum frequency generation, and second harmonic generation techniques by extending the Berek compensator theory just a little. All are based on the birefringence of uniaxial crystals. Appendix A reviews the theory that underlies these important devices.

We used two primary techniques to measure how well the Berek compensators circularly polarize the OPA generated light. One technique is more sensitive to incomplete circular polarization due to pulse bandwidth, and the other technique gives

us a better idea of the pulse ellipticity. The results presented here were obtained for pulse trains at wavelengths of 857 nm and 873 nm respectively.

One of the techniques we used was to send a pulse train twice through a Berek compensator in its quarter-wave plate configuration (see Figure 5.3). Ideally, with two passes, the compensator becomes a half-wave plate oriented with its fast (or slow) axis at $\pm 45°$. This rotates the linearly polarized input by 90° [42, pp. 301–303]. If, for example, the input is horizontally polarized, the output will be vertically polarized. With a horizontal analyzer (we use a Glan-Foucault polarizer) we can block all of the vertically polarized light and measure only the horizontal component.[8] The fraction of the light still horizontally polarized, either as a component of linearly polarized light or time averaged elliptically polarized light, gives us a measure of how well the Berek compensator is working as a quarter-wave plate. Since we used this technique to optimize both the tilt of the crystal in the compensator and its azimuthal angle, we expect that the transmitted component is primarily an uncorrectable result of pulse bandwidth, although we have not done calculations to determine the theoretical limit. Results of this test, shown in Figure 5.4, show that only about 3% of the incident light power is transmitted by the horizontal analyzer.[9] With the compensator fast axis parallel to the incoming polarization (no component retarded), at least 85% of the incident light power is transmitted by the analyzer.

A second, more direct way we test a Berek compensator is to send the pulse train one pass through the compensator and then through an analyzer (polarizer), measuring the power transmitted through the analyzer at various azimuthal angles (see Figure 5.5). If the light is perfectly circularly polarized, the time averaged signal measured by the photodiode will not depend on the angle. We found the ratio of the highest to lowest powers transmitted by the analyzer to be 81% for pulses from OPA-B, 88% for pulses from OPA-N, and 12% for light without the compensator (see Table 5.2). We used a dichroic polarizer as the analyzer to avoid the

---

[8]Birefringent polarizers, to include the Glan-Foucault polarizer, are described in Reference [42, pp. 290–292]. The Glan-Foucault polarizers were 100% effcent to the level we could measure with our photodiodes.

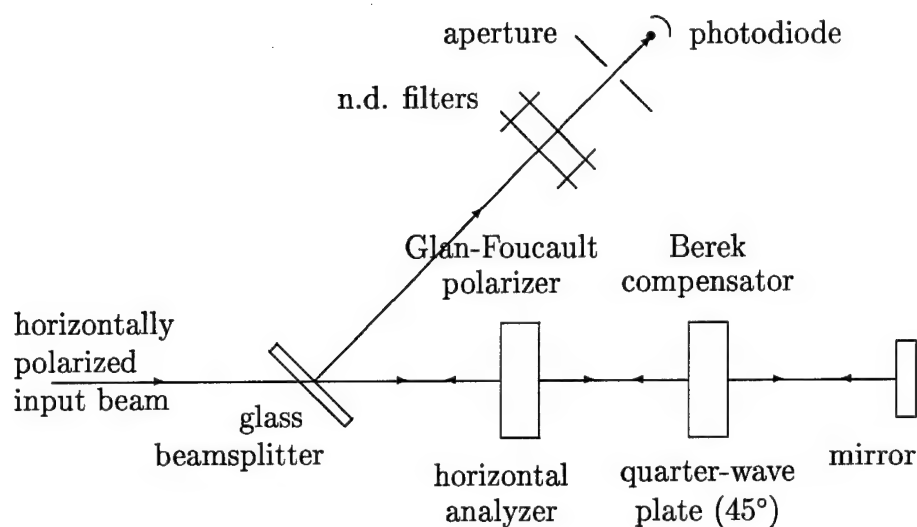[9]Reflection losses, which vary slightly with the Berek compensator setting, have been ignored.

Figure 5.3: Test of Berek compensators for circular polarization. With two passes, the Berek compensator at ±45° is acting as a half-wave plate, and ideally rotates the polarization to vertical. whence it cannot pass the analyzer. The mirror is very slightly tilted so that unwanted reflections off of the front faces of the analyzer and compensator can be intercepted by the aperture.
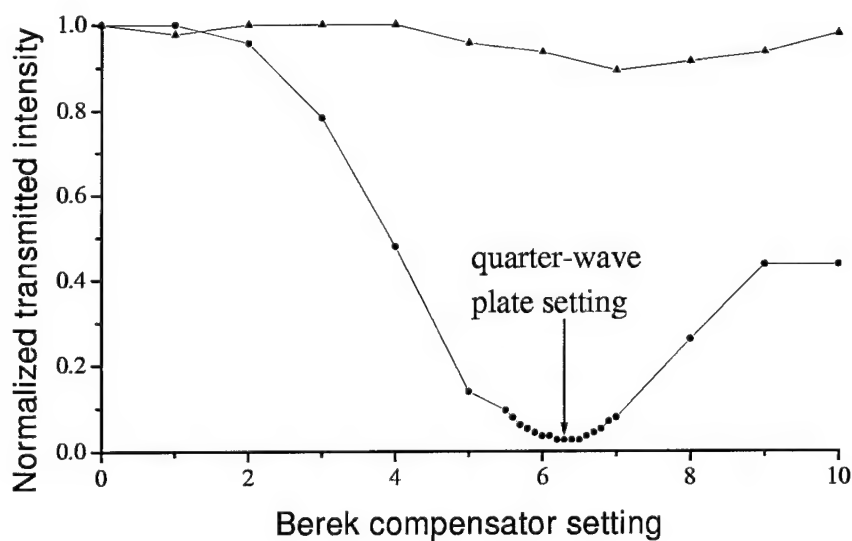

Figure 5.4: Results of circular polarization test shown in Figure 5.3. The data plotted as triangles is for incoming light parallel to the slow axis of the Berek compensator (no retarded component). The data plotted as circles is for incoming light polarized at 45°, so that the output is rotated to vertical after two passes. Less than 3% of the intensity is transmitted in this case.
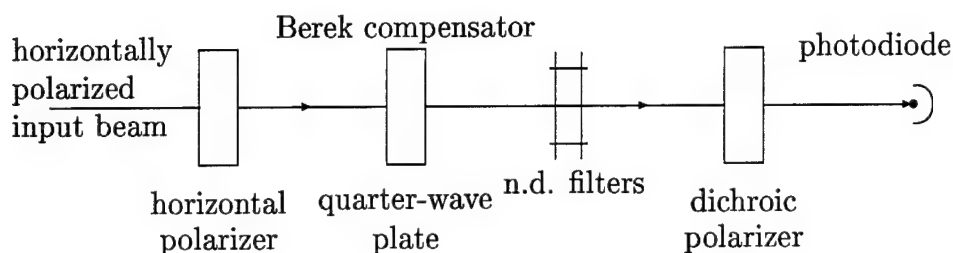
Figure 5.5: Another test of Berek compensators for circular polarization. The figure shows a setup for horizontally polarized input, but there is a similar setup for vertically polarized input. Ideally, the quarter-wave plate converts the input to circularly polarized light, which is transmitted with equal intensity at any orientation of the polarizer. In fact, the intensity variation was 12% for one pulse train and 19% for the other.

slight asymmetry shown by the Glan-Foucault polarizers with respect to direction of rotation (e.g. the minimum at 0° is different from the minimum at 180°), but the extinction of cross-polarized light was not nearly as good, as indicated by the 12% figure. We know the input polarization to be quite linear since the power transmitted through a Glan-Foucault polarizer as a function of polarization axis angle matched the Law of Malus (see Figure 5.7). The ratios of the amplitudes of the highest to lowest electric fields come to 90% for OPA-B and 94% for OPA-N based on these measurements, but they may in fact be slighly lower due to the incomplete extinction of cross-polarized light. It is possible that some ellipticity comes from the final metal mirror; the compensators were placed behind the final mirrors for most experiments.

5.3 Pulse characterization

For our experimental measurements to be meaningful, we must know the characteristics of the pulses that interact with the semiconductor sample. The time integrated spectral characteristics are measured with the OMA or CCD camera. Simply by viewing our beams with an IR phosphor card or IR viewer we know that the transverse spatial pulse profile is circular, somewhat Gaussian. We probe an area that

| POLARIZER | SIGNAL (mV) $\propto$ INTENSITY | | |
ANGLE	polarizer	OPA-B	OPA-N
vertical	370	365	190
horizontal	70	300	170
+45°	—	340	185
−45°	—	310	165
background	30	30	30
	$\frac{I_y}{I_x} = 12\%$	$\frac{I_y}{I_x} = 81\%$	$\frac{I_y}{I_x} = 88\%$

Figure 5.6: Data from the setup drawn in Figure 5.5. No meaning should be attached to the absolute measurements and no comparison should be made between columns. Data at ±45° are shown for comparison; I_x/I_y is calculated from vertical and horizontal measurements. Numbers shown are averages from several measurements with an error of $\sim \pm 5$.
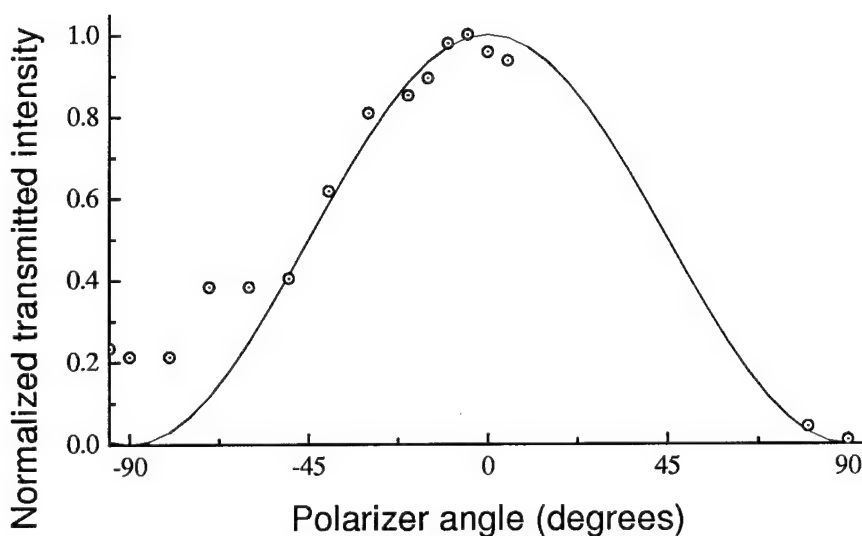

Figure 5.7: The fractional intensity transmitted by the Glan-Foucault polarizer as a function of polarizer-polarization angle. The solid line represents the Law of Malus which is the theoretical transmission. The asymmetry in the polarizer is evident, but the complete extinction at +90° indicates fairly linear input polarization.

is small compared to the pump spot area so that the probed region has a fairly uniform intensity.[10] In the pump-pump experiments we sometimes used an iris to select a homogeneously excited area of the sample, but the beam radius was really too small for this to be very useful. The longitudinal spatial and phase profiles are the most difficult to determine, since no electronics can react fast enough to get an accurate time profile[11] and no photodetector is sensitive to the phase. For the supercontinuum probe it was not possible to use the characterization tools that we used for the other pulses, so we measured the chirp using two-photon absorption in ZnO as described in Subsection 7.2.3. Since it was only used as a probe, the pulse energy and spot size were unimportant so long as the probe spot was small compared to the pump spot. For the other pulses, we used interference to convert the time measurements to space measurements and we used a technique (frequency resolved optical gating, FROG) which combines the spectrum and autocorrelation to determine pulse phase. These techniques are examined below.

5.3.1 Autocorrelation and frequency resolved optical gating (FROG)

We use the frequency doubled output of a Michelson interferometer to measure the autocorrelation of our pulses. There are several variations to the autocorrelator: first order versus higher order autocorrelators, background present versus background free autocorrelators, single shot versus averaging autocorrelators, intensity versus interferometric autocorrelators, and autocorrelators that use a host of non-linear optical process. While all of these variations are examined in Reference [49, pp. 365–372], we will only consider (1) first order, (2) background free, (3) pulse averaging, (4) intensity autocorrelators using (5) second harmonic generation (SHG). We actually use three autocorrelators, two of which share all five of the above listed properties and another which is a single shot autocorrelator. Since the single shot autocorrelator is a commercial system (Positive Light) we will only note that the

---

[10]As discussed on page 349 of Reference [4].

[11]The longitudinal spatial profile can be considered as a function of space in a reference frame moving at the group velocity or as a function of time at a point in the lab frame. Since it is impractical for us to move intruments at the pulse group velocity, we must make time resolved pulse measurements.

time autocorrelation is changed to a spatial intensity distribution which is read out by a CCD array.[12]

The general concept of our autocorrelators is shown in part (a) of Figure 5.8. The Michelson interferometer[13] divides the light from a single pulse train equally between two paths and then recombines them at the output. The output pulse trains from either arm are not collinear, but rather cross in a BBO crystal. The vector phase matching condition dictates that the second harmonic signal generated from the combination of light from both arms will be inbetween the second harmonic signals generated by the individual pulse trains. The intensity of the "sum" second harmonic signal is, roughly speaking, proportional to the pulse overlap. As one arm is scanned to change the overlap, the autocorrelation is mapped out. The physics behind this effect is the subject of Appendix C.

The autocorrelation only provides limited information. It is always a symmetric function peaked at its central value. It does not uniquely determine the autocorrelated function. But if you have some reasonable estimate of the pulse shape, the autocorrelation is very useful. For example, a double pulse will generally give a three peaked autocorrelation. You can also determine the pulse duration if you reasonably know the pulse shape.[14] If you know the pulse shape, you can further calculate how close it is to bandwidth limited, where it must be chirp free.

To get more information, one has to know more about the field as a function of time delay. Frequency resolved optical gating technique (FROG) is a technique in which the spectrum is measured for each delay position of an autocorrelation.[15] Complicated iterative mathematical algorithms exist to piece this information into

---

[12]The concept was developed by Jansky et al. [52] and applied to femtosecond pulses by Salin et al. [53] and Rempel and Rudolph [54].

[13]Since the souce is a laser beam and not an extended source, and since there is no compensator, some would argue that it is a Twyman-Green interferometer. However, the lenses usually found in a Twyman-Green interferometer are absent. Since the Michelson and Twyman-Green interferometers are nearly identical, we will stick with historical precedence.

[14]See Reference [49, p. 383]. Typical autocorrelation halfwidth to pulse halfwidth ratios are 1.414 for Gaussian profiles and 1.543 for $sech^2(t)$ profiles.

[15]A good appreciation for the potential of the various types of FROG and for interpreting the results without computation can be gained in Reference [55].
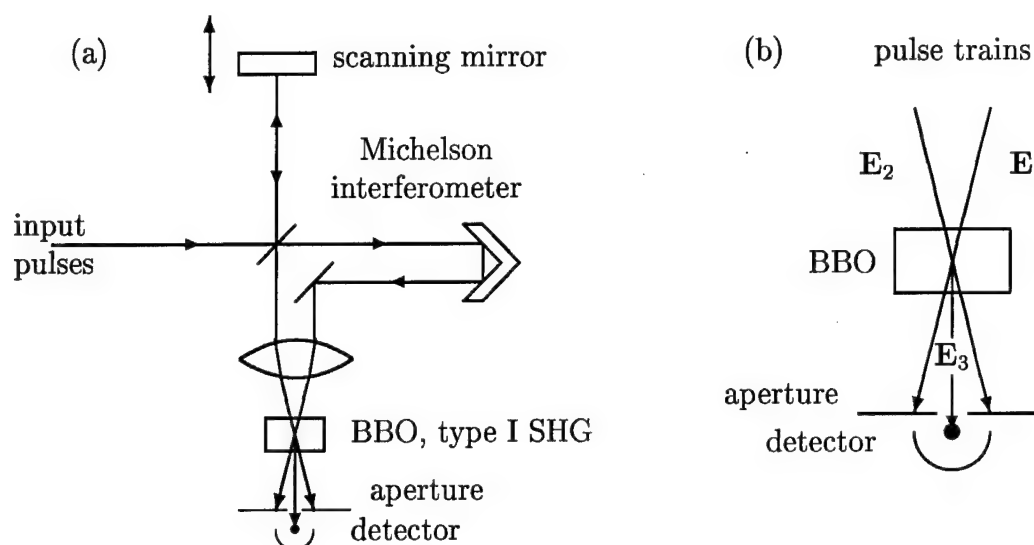
Figure 5.8: Part (a): Concept of the second harmonic generation autocorrelator: a pulse train is split into two by a Michelson interferometer and recombined in a $\chi^{(2)}$ crystal. Measurements of the second harmonic intensity are taken at various time delays between the beams, τ, controlled by the scanning mirror. The intensity as a function of τ is proportional to the intensity autocorrelation. One of our autocorrelators uses a photomultiplier for the detector, another uses a diode array, and the third use an OMA. Part (b): Labeling of the pulse trains used in the text.

an electric field amplitude (or intensity) and instantaneous phase profile of the pulse [56]. The result is unique and the characterization of the pulse is complete, limited of course by experimental inaccuracies and the sampling period $\Delta\tau$.

We get FROG traces by directing the ouput of an autocorrelator to the OMA or CCD camera, where a second harmonic spectrum is accumulated for each delay position. The spectra are combined into a three dimensional plot of pulse intensity versus time delay and frequency. We use a commercial computer program to extract the pulse characteristics from this plot, yielding the pulse shape, pulse phase (from which we can find chirp), pulse duration, and time-bandwidth product.

5.3.2 Cross-correlation

If the wave mixing analyzed in Appendix C is done with separate pulse trains, as opposed to a single divided pulse train, the result is the cross-correlation. The

mathematics is essentially identical except that the two beams may have different pulse profiles and spectra. Certain integer factors may vary because of conventions defining the nonlinear susceptibilities,[16] and one will have to relabel the frequencies involved, but that is all. If one knows the temporal intensity profile of one of the pulses, we will call it the reference pulse, then the profile of the other pulse is obtainable through Fourier techniques [57, pp. 172–173]. In the limit that the reference pulse is a delta function in time, the cross-correlation will be the pulse profile. Like the autocorrelation, however, no phase information can be garnered from the cross-correlation alone.

In our pump-probe measurements the pump pulse is generally much longer than the probe pulse, typically by a factor of five or so. Having done an autocorrelation or FROG measurement of the probe, we often use it as a reference pulse for cross-correlating with the pump pulse. This is convenient for several reasons: (1) the cross-correlation does not require aligning an interferometer, (2) the alignment for the cross-correlation is the same as has to be done to get pulse overlap in space and time for the experiments, and (3) the cross-correlation gives us an accurate time zero (best overlap) for the experiments. These last two advantages accrue because we have set up the BBO crystal for cross-correlation to be at the sample position, with the sample and cryostat removed, of course. It has proven easier, at least with non-collinear measurements, to get the initial overlap in the BBO crystal and then move the sample into the crossed beams. One more advantange of a cross-correlation is that with a short reference pulse, the cross-correlation profile is similar to the actual pulse profile. There is not as much uncertainty as in an autocorrelation, which can smooth larger features.

To summarize the most important points of this section, we use autocorrelations, cross-correlations, and FROG to characterize the pulses as they are just before interacting with the samples. These techniques use nonlinear wave mixing combined with variable pulse delay to probe ultrashort times. We use the results of these measurements to characterize the input pulses which interact with the semiconductor

---

[16]Specifically I mean the degeneracy factors.

samples.

5.4 Pulse focusing and overlap

We have four main concerns with pulse focusing and overlap: (1) that both pulse trains are centered at the same lateral position on the sample (spatial overlap), (2) that we know how the pulses are overlapped longitudinally (temporal overlap) as a function of delay (i.e. we know the time zero), (3) that we have some control over the cross sectional area to optimize the coupling and interact with a uniform piece of the sample, and (4) that we know the cross sectional area so we can calculate intensity from pulse power. We now address the two overlap concerns and the two cross sectional area concerns in the discussion that follows.

5.4.1 Pulse overlap

We decrease the pulse cross sectional area with a lens (for collinear beams) or a pair of lenses (for non-collinear beams) placed just before the sample. The primary reason for focusing is to limit the light-semiconductor interaction to a small area of the sample where quantum well irregularities are small. Smallness is not well defined, but it is easy to see that some spots on the samples have better defined exciton resonances, less baseline absorption or scattering, or less Fabry-Perot fringing than other spots.[17] We are limited in how small we make a spot primarily by diffraction, as we show in Appendix D, but tighter focusing means less light for a given intensity which can lead to problems with noise. Tight focusing can also make overlap more difficult and makes the overlap sensitive to smaller changes in beam direction, so there is a tradeoff to be made.

In the non-collinear geometry, we use the focusing lenses also to make fine corrections to the spatial pulse overlap. For collinear pulse trains we adjust the overlap with electronically controlled precision actuators on the final steering mirror before the beamsplitter that combines the pulses. The challenge is to know when the pulse

---

[17]We can see this, for example, in a thermal light spectrum where we select a sample area by using an aperture at a sample image.

trains have maximum overlap.

We have installed a television camera which images the sample. A microscope slide reflects a small fraction of the light from the pulse trains into the camera while the majority of the light continues on to the detector (see Figure 5.1, page 88). We image the sample either by reflecting light from a lamp off the back surface of the sample or by viewing the I.R. light from the lamp transmitted through the sample. Once the sample is well imaged, the pulse trains will coincide in the camera only when they cross in the sample. This works well in theory, but in practice it is impossible to tell when the sample is in focus to sufficient accuracy to use this for initial beam alignment. Once overlap has been established, however, the camera can be adjusted to the correct focus and thereafter used as a guide.

A better way to get the initial overlap of non-collinear beams is to use sum frequency generation (SFG). It is necessary to do this anyway to get the time zero, which is established accurately by cross-correlation. We need both spatial and temporal overlap to get SFG, so we have to get some spatial overlap either visually (I.R. viewer) or with the television camera described above.[18] We adjust the angle of the BBO crystal to midway between the phase matching angles of the individual beams. The delay line is then driven back and forth until we get some SFG signal (which might take hours if we cannot get good enough spatial overlap). We can then optimize the phase matching angle, the spatial overlap, and the temporal overlap. The BBO crystal is removed, and the sample is placed approximately in the same position.

Overlap in the sample can now be accomplished by moving the sample to the overlapped beams. In the non-collinear, dual-OPA, pump-probe configuration we measure only the probe spectrum, which shows the light hole exciton resonance. This resonance can be bleached by carriers excited by the pump pulses. Since the bleaching can only occur if the pump excites carriers at the same sample position as the probe, we can use the bleaching to optimize overlap. When the supercontinuum pulse is used as the probe, we use exactly the same technique, but have the luxery

---

[18]It is a little easier to focus the television on the BBO crystal than on the sample.

of monitoring the response of both excitons. In principle we could use the same technique for the collinear geometry, but the intense pump signal would dwarf the probe signal. There are techniques for overcoming this, but we did not use them. For collinear beams it is sufficient to ensure that the beams are overlapped before and after the sample and on the television image.

5.4.2 Pulse cross sectional area

We measure the pulse cross sectional areas using the television camera. The pulses produce images on the camera of a fairly well defined size that does not change with intensity. We call the area of this image (scaled for magnification) the pulse cross sectional area, although the lateral intensity distribution is not well known and the area cannot be a precise quantity. Pulse intensity at the sample is difficult to measure to better than one significant figure anyway, and it fluctuates on about the same scale; however, it is important that we can compare one spot size to another. None of our results depend on precise scaling, so the beam spot area defined by the apparent cutoff on the television is adequate.

There are several features on the camera image that we can use to scale the beam cross sectional area: the sample itself, the opening in which the sample is mounted, and the sample holder. With this scaling method, we measure spot diameters of about 100 μm.

We can change the cross sectional area somewhat by defocusing the image. This is useful for all of the reasons mentioned earlier, to decrease intensity, to decrease sensitivity to beam movement, and to make ovelap easier. It is also useful in pump-probe measurements to make the probe small compared to the pump, so that the pump intensity is fairly uniform over the probed area and carrier diffusion is less important. Unfortunately, the difference between the lower (diffraction) limit and the upper (distorted spot) limit is only about a factor of around five.

It is interesting and perhaps useful to understand what is limiting our spot sizes. Appendix D is an analysis of the effect of diffraction and lens aberration on the achievable spot sizes in our setup.
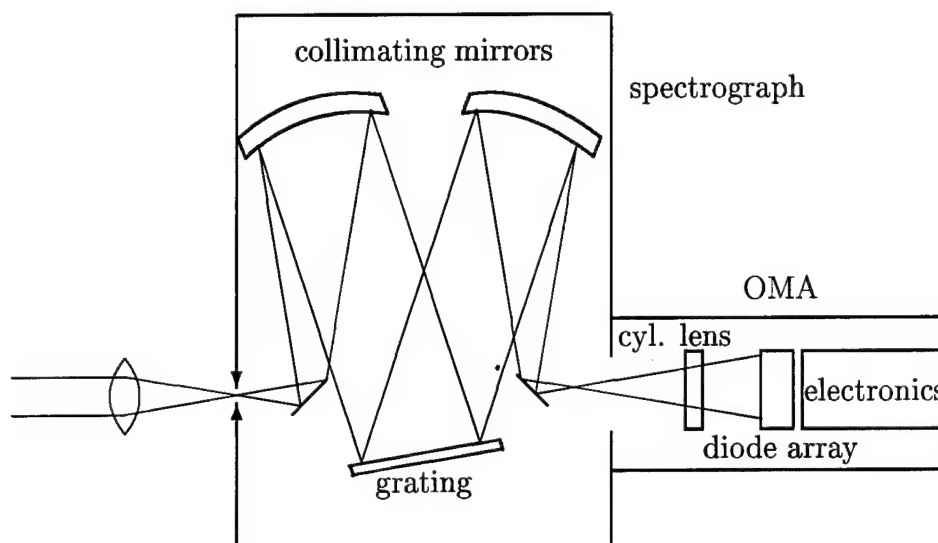
Figure 5.9: Concept of the optical multichannel analyzer: light is dispersed by a spectrograph, and a portion of that light is imaged onto a diode array, giving the power spectrum of a certain bandwidth of light. The band is changed by rotating the diffraction grating.

5.5 Signal detection and calibration

Both the optical multichannel analyzer (OMA) and CCD camera are instruments that read out the intensity spectrum of light that has been dispersed by a spectrograph (see Figure 5.9). They permit the rapid collection of spectra that do not individually suffer from intensity fluctuations, since the entire spectrum is measured simultaneously. Time resolved measurements such as constitute this dissertation require multiple spectra, however, and there are still problems with low frequency noise.

The low frequency noise problem has been a serious obstacle to collecting reliable, repeatable data that shows the effects we are interested in. We initially collected data with a 40 cm Thermo Jarrell Ash spectrograph attached to an EG&G OMA. Over the (typically) 64 to 256 spectra collected to map out the light-semiconductor interaction, we saw fluctuations in the intensity due to the light production system alone. It was not always possible to separate laser induced light fluctuations (low

frequency noise and jitter) from semiconductor induced light fluctuations (what we are interested in). We installed a one meter McPherson spectrograph and acquired a CCD camera with a two-dimensional readout in May 1999. With this system, we are able to simultaneously measure a reference spectrum along with the transmission spectrum to account for intensity fluctuations.

The EG&G OMA uses 1024 silicon photodiodes in a linear array. Its grating disperses the spectrum over a 120 nm range of wavelengths, so the maximum achievable resolution is about 1 Å. The actual resolution depends on the size of the entrance slit, and is about 0.5 nm for the slit we normally use. The system uses microprocessors to acquire and process spectral data and to manipulate and store that data. The data is displayed on a cathode ray tube. It is fully computer controllable over the GPIB interface.

The Thermo Jarrell Ash spectrograph that we use with this OMA is manually tuned and must be recalibrated every time the wavelength is changed. In the 800 nm spectral range we calibrate it using spectral lines from a xenon lamp, and in the 400 nm range (sum frequency or second harmonic) we use a mercury lamp.

The Apogee CCD camera has a two-dimensional CCD array upon which we image the signal spectrum and a reference spectrum. It is conceptually a two-dimensional OMA. A LabView computer program allows us to measure two designated subarrays within the CCD array. By comparing the signal and reference spectra, we are able to differentiate between changes due to the sample and fluctuations in the light pulses. The camera reads out a spectral width of about 20 nm in the near infrared.

The McPherson imaging spectrograph that we use with this camera theoretically resolves tenths of angstroms in the spectrum. We calibrate the spectra in the same way as for the Thermo Jarrell Ash spectrograph. The tuning is electronically driven, which makes it unnecessary to recalibrate every time the spectral region is changed.

We couple light into the McPherson spectrograph with 200 μm multimode optical fibers, which ensure that the two spectra are imaged at the same lateral position on the CCD array. Once the fibers are correctly positioned at the entrance slit,

it is not necessary to readjust the light going into the spectrograph. The fibers transmit about 60% to 80% of the input in red to near infrared wavelengths. We can collect nearly all of this light in the spectrograph if we set the entrance slit to get 0.25 nm spectral resolution. We selected multimode fibers so that we can vary the wavelength. The fibers do well in carrying the violet second harmonic or sum-frequency signals as well as the infrared signals.

5.6 Sample cooling

In order to observe coherent light-semicondutor effects, the coherence decay time must be more than the duration of the effects themselves. This amounts to a requirement to cool the samples to low temperatures. We cool our samples using a simple Janis Research continuous flow cryostat, in which liquid helium cools a cold finger in thermal contact with the sample to 4.2 K. The sample is insulated by a vacuum, which we pump with a liquid nitrogen cooled sorption pump to about 10 μm of Hg. The cold finger has a silicon diode temperature sensor connected to a digital readout. The cryostat windows are quartz.

CHAPTER 6

EXCITONIC RABI OSCILLATIONS

6.1 Overview

We successfully observed multiple excitonic Rabi oscillations in an InGaAs multiple quantum well in November 1998. While not the first observation of semiconductor Rabi oscillations, our results are significant for several reasons. The first observation of a semiconductor Rabi oscillation is generally credited to S. Cundiff *et al.* for their 1994 experiment [58, 59], but the measurement was indirect and implied less than an entire Rabi oscillation. Harald Giessen *et al.* also made indirect measurements that implied just over three Rabi oscillations when they studied propagation effects in 1998, [60] but their experiment was unsuitable for studying the Rabi oscillations themselves. In 1997 Fürst *et al.* measured a single Rabi oscillation in the continuum states of InP [41]. Unlike these other experiments, however, our experiment offered (1) a direct measurement of excitonic density oscillations, (2) observation of up to eight oscillations originating from a single pulse, and (3) a study of the pulse intensity dependence of the Rabi oscillation rate. With this last piece of information, the pulse intensity dependence, we were able to make the first quantitative evaluation of Rabi oscillation behavior derived from semiconductor many-body theory, highlighting the similarities and differences of semiconductor Rabi oscillations to two-state Rabi oscillations and particularly optical Rabi oscillations in atomic and molecular gasses.

Our use of the two-color pump-probe experimental technique (discussed in Section 4.1) allowed us to create and measure the multiple oscillations. It is most significant that the relatively long 700 fs pump pulse had the large "pulse area" necessary to excite multiple Rabi oscillations in the heavy-hole exciton density, but not the large intensity that would create excessive excitation-induced dephasing

and destroy the coherence before several observable oscillations. By probing with a relatively short 150 fs probe pulse at the light-hole exciton resonance, we were able to unambiguously time-resolve the oscillations. Earlier, in Sections 4.4 and 4.5, we discussed using the transmission at the light-hole resonance as a probe of the oscillating heavy-hole exciton density.

Results presented in this chapter were published in *Physical Review Letters* (reference [61]) and the proceedings of Photonics West 1999 and CLEO 1999 (references [62, 63]). Prof. Binder made the theoretical calculations that model the experiment, and his results are presented in reference [38] as well as in the above listed experimental papers.

6.2 Previous experiments on Rabi oscillations

The first experimental use of Rabi oscillations was to measure the nuclear magnetic moments of two isotopes of lithium and one isotope of fluorine by I. I. Rabi and colleagues in 1938 [9, 64, 65]. In the previous year, Rabi had suggested the use of two-state nuclear spin systems subject to microwave radiation to induce what are now called Rabi oscillations [8]. The probability of a nucleus transitioning from the ground spin state to a higher spin state increases strongly as the microwave photon energy approaches the energy level difference. A molecule that had experienced a transition would be deflected out of the molecular beam by a magnetic field gradient.[1] Rabi's experiment determined the energy level splitting by the resonant ejection of molecules, and thus the nuclear magnetic moment which is proportional to the splitting. A variation of this concept is used today in medicine as magnetic resonance imaging (MRI), where the electromagnetic radiation is measured instead of the (stationary) molecules.

In 1957, R. P. Feynman applied the Rabi formalism to electric dipole interactions (masers specifically) using the rotating coordinates and Bloch sphere developed by Rabi, Ramsey, and Schwinger [25, 26]. With the advent of the laser, it became

---

[1]A description of the apparatus that makes this possible can be found in Rabi's original paper, Reference [9] and in Reference [66, pp. 35.4–35.6]

possible to test the optical analogs to the coherent spin effects that followed Rabi's work. Tang and Statz suggested in 1967 that it should be possible to observe Rabi oscillations with CO_2 laser pulses passed through a CO_2 amplifier [67]. Hocker and Tang succeeded two years later using a Q-switched CO_2 laser (FWHM $\approx$ 300 ns, peak intensity $\approx$ 20 kW/cm^2) and SF_6 gas [68]. They saw modulation at the leading edge of the transmitted pulse, which they identified as a Rabi oscillation. Clear, multiple Rabi oscillations are now easily observed using a technique pioneered by Brewer and Shoemaker in 1971 [69]. The Brewer-Shoemaker technique uses cw laser radiation, Stark shifting certain velocity groups of atoms within a Doppler broadened gas in and out of resonance. The gas that they used was $C^{13}H_3F$, which has a first order Stark shift. Their laser was, again, the trusty CO_2 laser. In addition to the laser induced changes in transmission discussed above, Rabi oscillations have also been seen by monitoring the fluorescence of a coherent excited gas [70].

With the development of the semiconductor Bloch equations [71, 72, 29], it was natural to seek coherent transient behavior in semiconductors, but the search has been hampered by the short coherence decay times and the inhomogeneous broadening. As in the atomic case, the first measurements were not dramatic. As described above, it was not until we reported the measurements described in this chapter that more than a fraction of a Rabi oscillation had been measured.

6.3   Sample and Pulse Characteristics

We made our Rabi oscillation measurements with a multiple quantum well consisting of twenty 8-nm layers of $In_{0.1}Ga_{0.9}As$ separated by 92-nm GaAs barriers, with approximately 0.5 μm $Al_{0.3}Ga_{0.7}As$ layers above and below. The sample was grown by Professors Hyatt Gibbs and Galina Khitrova using molecular beam epitaxy (MBE) on a carbon-doped GaAs substrate with an AlAs stop layer. We removed the substrate through selective chemical etching up to the stop layer. This sample was engineered to have a particularly large difference in heavy-hole exciton and light-hole exciton resonance energies. Unfortunately, the light-hole exciton absorption is much smaller in comparison to that of the heavy-hole exciton than the usual 1:3

ratio of hydrogenic transition probabilities. This is believed to be due to a spatial broadening of the valence band single particle wavefunction with increased indium concentration due to a decrease in the energy barrier [73]. The small absorption at the light-hole resonance made it challenging to get an acceptable signal-to-noise ratio.

The heavy-hole exciton resonance in this sample at a temperature of 5 K occurs at an energy of 1.433 eV, corresponding to a wavelength of 865.0 nm, while the light-hole resonance occurs at 1.464 eV or 846.8 nm. This 31 meV splitting and the transition dipole matrix elements were extracted from the linear spectrum for use in the theoretical modeling of the nonlinear response as explained in reference [61]. The linear spectrum is shown in Figure 6.1(a).
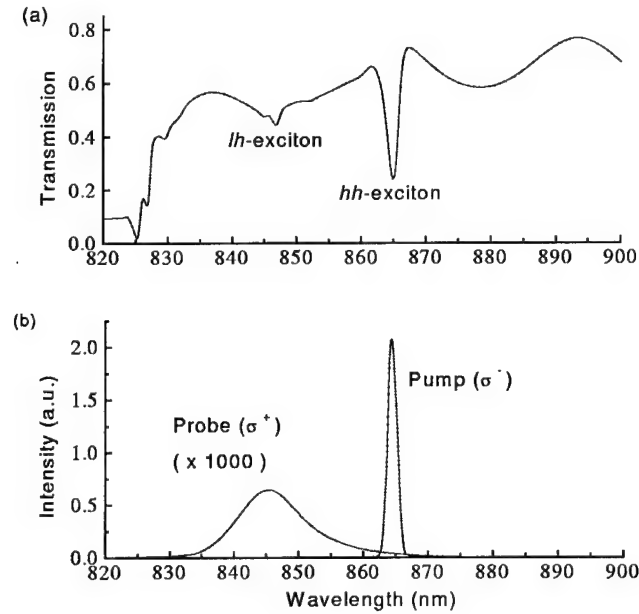

Figure 6.1: a) Linear low-temperature transmission spectrum of the $In_{0.1}Ga_{0.9}As/GaAs$ multiple quantum well in which we observed multiple Rabi oscillations. The overall spectrum is modulated by Fabry-Perot fringes. In addition to the 1s light- and heavy-hole excitons, several smaller InGaAs exciton resonances and the 825 nm GaAs barrier hh resonance are also visible. The sample is cooled to 5 K. b) Pump and probe pulse spectra used in the two-color pump-probe measurement of the MQW shown above. The pump pulse fluence was varied to study its affect on the Rabi frequency.

We made the pump pulse resonant with the heavy-hole exciton transition and of comparable width, as shown in Figure 6.1b. The pump pulse spectral width is (1.6 ±0.2) nm, with a measured temporal width of 770 fs. This compares favorably with the 660 fs Fourier limited Gaussian pulse width. The hh-exciton resonance is inhomogeneously broadened to a width of (2.0 ±0.2) nm. Because little excitation induced broadening was observed, Prof. Binder used the corresponding Fourier inverse (526 fs) as the dephasing time (T_2) for the theoretical model.

The 150 fs probe pulse had a 12.0 nm bandwidth (FWHM) and was centered near the light-hole exciton resonance wavelength. The broad bandwidth required to temporally resolve the Rabi oscillations resulted in some overlap of the probe pulse with the hh-exciton resonance. This interaction, though small, was included in the theoretical modelling. Thus, while the transition of interest was a two-band Rabi oscillation, the measurement technique exploited a third energy band (the light-hole band), and the modelling included six bands (three twofold degenerate bands).

6.4 Experimental Observations

We observed up to eight oscillations in the DTS at the light-hole exciton transition energy, corresponding directly to density (Rabi) oscillations in the $m_s = 1/2$ conduction band electron population. These density oscillations can be attributed to the light-induced transfer of electrons between the $m_J = 3/2$ heavy-hole valence band and the $m_s = 1/2$ conduction band, which is the only dipole allowed, resonant transition with a strong driving field (as covered in Section 4.6.3). The best data run is shown in Figure 6.2(a), but there were several data runs with clearly identifiable Rabi oscillations.

In Figure 6.2(a), we see a general increase in differential transmission from none at early negative pump-probe delay to about 8% for zero and positive delays. This increase is due to exciton bleaching from Pauli blocking and, to a lesser degree, Coulomb screening. As a quasi-equilibrium nonlinearity, the bleaching lasts for several picoseconds, much longer than the Rabi oscillations. The bleaching is very easy to see on a multichannel analyzer, and has proved a valuable too for achieving
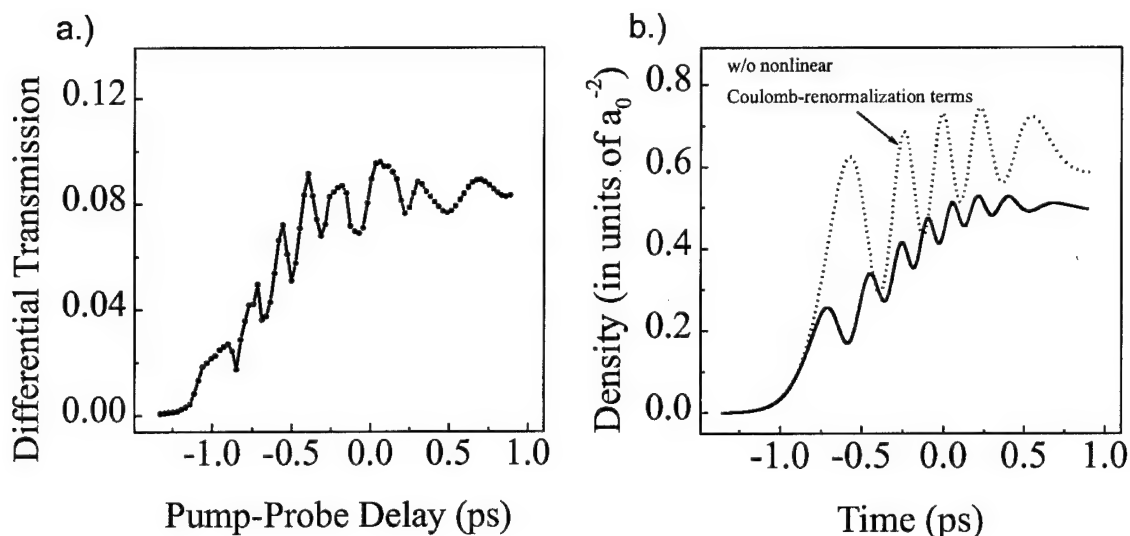
a.)

b.)

Figure 6.2: a) Differential transmission at the position of the *lh*-exciton due to a strong driving field at the *hh*-exciton resonance. The overall increase in transmission is due to exciton bleaching while the oscillations reflect the change in $m_s = 1/2$ electron density; i.e. Rabi oscillations. b) Theoretical $m_s = 1/2$ electron density in the Hartree-Fock approximation (solid), and the same electron density in the absence of Coulomb induced renormalizations (dotted).

spatial and temporal overlap. The amount of bleaching depends, of course, on the pump beam intensity.

The change in differential transmission that corresponds to the Rabi oscillations is seen to be only about 2% or less. To see this change in the DTS, it is necessary to achieve a stability in the probe pulse intensity somewhat near the 2% signal, which is only accomplished with much effort and some luck. We typically exposed the OMA for 100 ms (100 pulses) and averaged 50 of these exposures for both of the measurements needed at each of 128 or 256 delay positions. Adding time to move the delay line, open and close shutters, and digitally pass the data (albeit computer controlled), a single time resolved measurement took 45 minutes to $1\frac{1}{2}$ hours. Thus we had to contend with noise from the millisecond to hour time scales. We found it useful to smooth the data using adjacent averaging to enhance the signal.

We also see from Figure 6.2(a) that the Rabi oscillations are faster in the region of large pump intensity (near zero delay) and slower when the probe pulse overlaps

the wings of the pump pulse. Without the many-body renormalization, the Rabi frequency is directly proportional to the electric field strength, which means that the above observation is (at least qualitatively) consistent with our model.

We were able to make a more precise study of the Rabi frequency by taking several data runs and plotting the inverse of the average of the two fastest oscillation periods versus pulse energy flux (see Figure 6.3). Assuming a constant pulse shape, the pulse fluence is proportional to the square of the Rabi frequency at a particular point in the passing of the pulse. By using the fastest oscillations, we chose this point to be the peak electric field amplitude. The plot of Rabi frequency versus the pulse fluence shows the square root dependence characteristic of the unrenormalized Rabi frequency. In the next section we compare the experimental Rabi frequency to that derived from the semiconductor Bloch equations in the Hartree-Fock approximation.
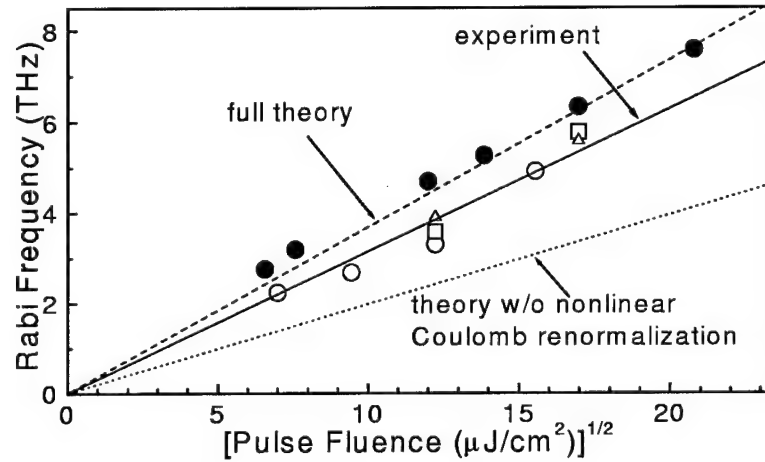

Figure 6.3: The classic (unrenormalized) optical Rabi frequency is directly proportional to the electric field amplitude and thus to the square root of the pulse fluence. This theoretical dependence is shown as a dotted line in the above figure. When Coulomb effects are included in the Hartree-Fock approximation, the Rabi frequency increases. Numerical calculations at several pulse fluences are shown as filled circles, and a dashed line is included to show that the dependence remains fairly linear, though shifted. The experimental results fell inbetween and are shown as open symbols, data from a single day shown with the same symbol. The solid line is a linear fit to the data.

6.5 Theoretical Modeling

Prof. Binder made the theoretical computations using the semiconductor Bloch equations in the Hartree-Fock approximation, as developed in Chapter 2 and shown in equations 2.76 through 2.80. Unlike the two- or three-band theories shown in this dissertation, however, he included all six bands discussed in subsections 4.6.2 and 4.6.3. In numerical computations, electron population was seen to oscillate between the $m_s = +1/2$ conduction band (actually its associated exciton state) and the $m_J = +3/2$ valence band. This population transfer affected light-hole exciton population due to the shared conduction band, and the oscillation of light hole transmission was, of course, the experimental evidence for Rabi oscillations. The inclusion of the three non-resonant bands slightly affected the population densities, but is not important for understanding the basic result.

Prof. Binder modeled the conditions of the experiment as accurately as possible, using both accepted and measured values.[2] He determined the hh-exciton dipole matrix element at the Γ-point by computing the linear absorption spectrum and adjusting the value of the dipole matrix element to fit the measured spectrum just above the band-edge, yielding a value of $\mu_{cv}/e = 0.575$ nm. The lh-hh splitting of 31 meV came also from the measured linear spectrum. Sample reflection losses of 32% were inferred from the accepted refractive index of 3.6. Prof. Gibbs determined the quantum well thickness to be 8 nm based on the conditions he created to grow the sample. The Luttinger parameters ($\gamma_1 = 6.85$, $\gamma_2 = 2.1$, and $\gamma_3 = 2.9$), effective electron mass ($m_e = 0.067$), and background dielectric constant ($\epsilon_b/\epsilon_0 = 12.7$) are based on accepted values. The parameter most in doubt in the computations was the dephasing time T_2. As mentioned earlier Prof. Binder decided to use the lowest dephasing time consistent with a collision-broadened heavy-hole linewidth of 2.0 nm based on the experimental fact that we observed little excitation induced resonance broadening. In any event, the semiconductor Rabi frequency is not strongly dependent on the exact value of T_2 [74].

---

[2]Input for this paragraph comes mostly from reference [61].

6.6 Conclusions

The theoretical computations agree well with the experimental results as seen in Figure 6.2. By comparing the experimental measurement of transmission at the light-hole resonance with the computed $m_s = 1/2$ electron density we see that the Rabi oscillations are fairly accurately modeled at the Hartree-Fock level of approximation. This qualitative accuracy disappears if one elimates the many-body corrections as was done for the dotted line in the figure.

Our quantitative study of the electric field strength dependence of the Rabi frequency as presented in Figure 6.3 shows that the actual Rabi frequencies are inbetween those predicted by the Hartree-Fock model and those without Coulomb renormalization. One can see that within the range of our measurements, the Rabi frequency still has a fairly linear dependence on the electric field strength. We expect that the inclusion of higher order approximation terms beyond the Hartree-Fock approximation would yield a closer agreement of theory and experiment.

CHAPTER 7

COHERENTLY COUPLED OPTICAL STARK SHIFTING

7.1 Introduction

Both one-photon transitions in a three-state system are coupled through the shared state even in the absence of a significant Raman-type coherence. Rather than use this coupling to get a high contrast probe as in the Rabi oscillation measurements, however, for the experiments described in this chapter we used a broadband probe to study the three-state coupling itself. Specifically, we did a set of measurements where the semiconductor was pumped in the transparency region below the hh-exciton resonance so that we excited an insignificant number of real carriers. Because of the coupling in the three-state system, the well-known off-resonant dynamic Stark shifting of the (lowest quantum well sublevel) hh-exciton resonance causes a Stark shifting of the lh-exciton resonance through the shared conduction band. With weak, broadband probe pulses, we time-resolved pump-induced changes in linear absorption at both hh- and lh-exciton resonances using both co-circularly-polarized (uncoupled transition) and counter-circularly-polarized (coupled transition) pump and probe. Again, as in the Rabi oscillation measurements, we saw deviations from the optical Bloch equations attributable to many-body Coulomb interactions.

Optical Stark shifting in semiconductors was first measured in 1985 by Frölich, Nöthe and Riemann using a long (20 ns) pump and a 60 ps probe [40]. In their experiment, 1S and 2P exciton states of bulk Cu_2O were coupled through an electric dipole transition by a Q-switched CO_2 laser, while the ground state to 2P exciton transition was probed by a tunable dye laser. A simple $\chi^{(3)}$ model was matched to the results in what clearly was stationary Stark shifting[1]. It is interesting to

---

[1]The stationary optical Stark effect, as opposed to the dynamic optical Stark effect, occurs

note that this very first optical Stark measurement used electric dipole coupling in a three-state "Λ" system made from exciton *envelope* states as a Stark shift probe. Frölich followed up this experiment by a measurement of quantum-confined optical Stark shifting two years later [75].

Meanwhile, the first nonresonant femtosecond pump-probe measurements of Stark shifting were made by Mysyrowicz *et al.* [76] and Von Lehmen *et al.* [77]. These measurements and others [78, 79, 80] showed transient blueshifting and bleaching of an exciton resonance, while similar experiments soon to follow showed transient spectral oscillations in transmission for negative time delays [81, 82]. Both of these coherent effects were analyzed in terms of the dynamic semiconductor optical Stark effect [83, 84, 85, 86, 87, 88, 89, 90], and the importance of many-body effects, manifested by deviations from atomic Stark shifting, became clear. The theoretical and experimental basis for dynamic Stark shifting in semiconductors continues to grow, now including a biexciton induced redshift [91, 92] and a Coulombic redshift [93, 94]. These redshifts are theoretically impossible in atomic systems, but have been experimentally verified in semiconductors under carefully prepared conditions.

7.2 Experiment

Our experiment was designed primarily to measure the Stark shift of a *lh*-exciton under the influence of a Stark shifted *hh*-exciton. We did take some data for resonant Stark shifting as well as data with the pump pulse between the *hh*-exciton resonance and the *hh*-continuum absorption, but that data is much harder to analyze due to the difficulties in subtracting scattered pump light and in accounting for real-carrier generated nonlinearities. We plan to explore this data in more detail in the near future.

---

when the light field amplitude variations are slow enough to make an adiabatic approximation [7, p. 307]

7.2.1 Experimental scheme

We ran a series of time-resolved DTS measurements with co-circularly-polarized and counter-circularly-polarized pump and probe pulses. The probe was too weak to cause a nonlinear response except for the coherent oscillations,[2] and the pump was kept far enough off resonance to excite negligably few real carriers. Pump-induced virtual transitions resulted in a coherent Stark shifting of either the σ^+ or σ^- transition of the hh-exciton, depending on the pump polarization. For the first time, we used a broadband probe pulse created by reflecting a small portion of the supercontinuum generated in the OPA. We alternated between making this probe pulse co-circularly polarized with the pump to measure the hh Stark shift and making the pulses counter-circularly polarized to measure the "V"-system coupled lh Stark shift. There is actually some higher order Stark shifting induced in the opposite three-state system which will be discussed later.

7.2.2 Multiple quantum well sample

We used another InGaAs/GaAs MQW sample for this experiment, but with less indium doping (4% by number) than that used in the Rabi oscillation experiment (10% by number). This resulted in three primary differences: (1) a lower band-edge energy, (2) less splitting between the lh- and hh-exciton resonances, and (3) a larger lh-exciton oscillator strength. The lower band-edge energy put the excitons into a spectral region with more substrate absorption than the previous sample. It was not possible to remove the substrate as I did with the Rabi experiment sample (no AlAs stop layer), so I could only polish it to a minimum thickness (about 50 μm). Nonetheless, substrate absorption was not a significant impediment to the measurements, and is subtracted from all data shown in this chapter. We spectrally narrowed the pump pulse to 2.2 meV (1.2 nm) so that the lh-hh splitting was more

---

[2]Interference of the probe-induced polarization with the leading tail of a pump pulse generates a population grating which scatters pump light in the probe direction. This scattered pump light interferes with the probe light at the detector, causing harmonic oscillations in the DTS with an argument proportional to the time delay [81, 4, pp. 392–395] This allows an accurate determination of time zero.

than enough to decouple the *lh*-exciton from any directly induced Stark shifting. Finally, the increase in *lh*-exciton oscillator strength gave us a much better signal-to-noise ratio than would have been possible with the other sample. All measurements were done with the sample cooled to 4.2 K.
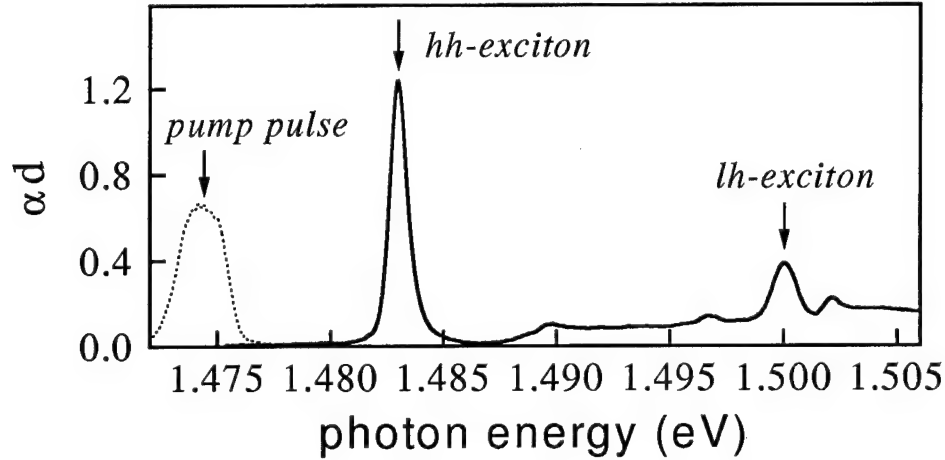

Figure 7.1: Linear absorption spectrum of the $In_{0.04}Ga_{0.96}As$ MQW sample used in the Stark shifting experiment (solid line). The $1s$ *hh*-exciton and $1s$ *lh*-exciton resonances are labeled, and the other smaller resonances are not positively identified. The pump pulse spectrum is shown (dotted line) for a detuning of 8.5 meV (5 nm), with amplitude scaled in arbitrary units.

The MQW structure used in the Stark shifting experiments consists of ten $In_{0.04}Ga_{0.96}As$ quantum wells grown by MBE to about 8 nm thickness. The barriers are about 65 nm of GaAs, and the substrate is C-doped GaAs. Its low temperature spectrum shows sharp *hh*- and *lh*-exciton resonances that are spectrally very well resolved (see Fig. 7.1). Strain increases the splitting over simple quantum confinement to 17 meV or 9.5 nm.

7.2.3 Pulses

We used a single OPA to produce both the pump pulses and the probe pulses for this experiment. We measured the pump pulses to be 1.2 ps in duration (FWHM) as compared to the Gaussian bandwidth limit of 830 fs. They were tuned within the transparency region to be between 3.5 meV (2 nm) and 10.6 meV (6 nm) below the

linear hh-exciton resonance. For most measurements, the pump pulses carried 2.4 nJ of energy focused to a 240-μm diameter spot for a peak intensity of 3.7 MW/cm^2, while for the two largest pump detunings the peak intensity was increased to 21 MW/cm^2 by removing a filter.

The probe pulses were focused to a diameter of about 100 μm in the central region of the pump spot to avoid inhomogeneous excitation. Their spectrum was very broad, as they came from the OPA supercontinuum that seeds pulses with wavelengths from at least 800 nm to 1.1 μm (the white appearance suggests spectral content throughout the visible spectrum, but it is not measurable). This spectrum, however, was very strongly peaked around 790 nm wavelength, falling off somewhat exponentially to either side. In the spectral region of interest, the probe spectrum was fairly flat, but more than two orders of magnitude below peak intensity. We used two 830 nm edge filters to reduce the unwanted light which was being absorbed by the sample and causing undesired nonlinearities. We overcame the somewhat low probe intensity by exposing the CCD camera for 500 pulses (typically) and then averaging ten exposures. Probe pulse intensity fluctuations were compensated for through a reference pulse that was collected before the sample with an optical fiber. The transmitted probe and reference probe were imaged to different parts of the CCD camera detector array and processed as a divided signal.

We measured the chirp of the probe pulses using two-photon absorption in a ZnO crystal. The beam of probe pulses was made to intersect in the ZnO crystal with an intense pump pulse train. No pulse shaper was used since it introduces a small chirp that could affect the results. The crystal absorbs probe pulses with a logarithmic absorption, αd, that, in the limit of a weak probe, is proportional to the pump intensity, $\alpha = \sigma^{(2)} I$ [4, p. 276]. The two-photon transition coefficient, $\sigma^{(2)}$, also depends on the sum of the absorbed photon energies with an obvious cutoff at the ZnO bandgap energy, 3.2 eV. We measured the probe transmission in spectral regions where the only significant two-photon transition cross-section involves one pump photon and one probe photon. The pump photon energy was fixed at around 2.1 eV (590 nm) as a compromise between intensity and maximum $\sigma^{(2)}$.

Each spectral component of the probe pulse has a different two-photon absorption cross-section, but for every spectral component the absorption is maximized with maximum pump pulse intensity; i.e. maximum pump-probe overlap. The pump is unchirped, so the time delay associated with maximum absorption is the time zero for that frequency component. By plotting the time zeros versus probe photon energies we get a plot of the chirp (see Figure 7.2). The linear component of the chirp was 1.8 fs/meV which is very small over the range of energies that we made our measurements.
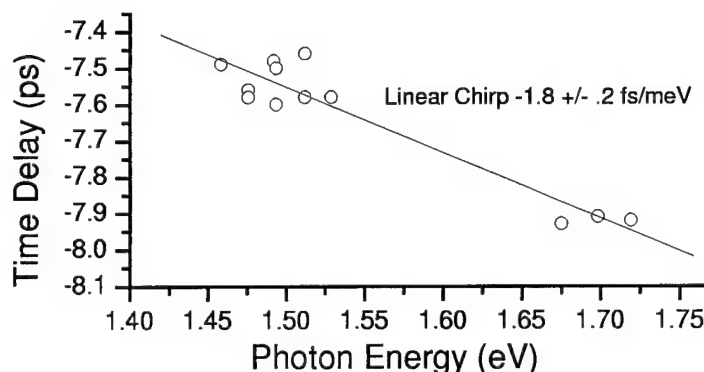
Figure 7.2: Measurement of the supercontinuum pulse chirp. Each data point represents the time delay for maximum two-photon absorption at the corresponding photon energy. A linear fit gives the linear component of chirp over the measured range. The significant result is that probe pulse chirp is negligable within the spectral range of our experiments.

7.2.4 Determination of time zero

Just prior to making the pump-probe measurements, we determined the time zero by cross-correlating the pump and probe pulses. As usual, the cross-correlation was done using sum frequency generation in BBO. The DTS data, however, allowed for an even better determination of time zero that was not affected by beam shifts or inaccuracies in filter delays. This was through the use of the coherent oscillations present at negative delays in the measurements. Figure 7.3 shows several DTS spectra stacked in order of increasing overlap. The wavelength difference between spectral oscillations is seen to increase as the pump-probe overlap improves. At

maximum pump-probe overlap the wavelength becomes infinite, and this is the time zero. A plot of time delay versus oscillation wavelength is shown on the right side of figure 7.3, from which the time zero is easily determined.
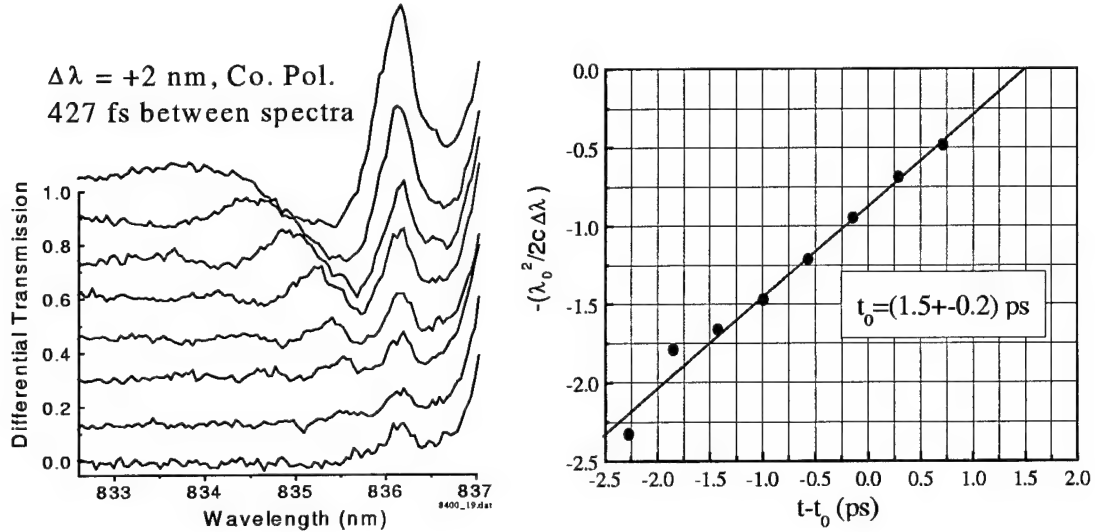

Figure 7.3: Left: An offset sequence of negative time delay differential transmission measurements (earliest at the bottom) for a pump detuning of 3.5 eV (2 nm) and co-polarized pump and probe. An increase in the vicinity of 836 nm wavelength is seen due to Stark shifting, bleaching, and fluorescense. Coherent transmission oscillations, which are only present at negative delays, are clearly visible at lower wavelengths. The apparent rise in differential transmission at higher wavelengths is due to scattered pump light. Right: The coherent oscillations approach an infinite wavelength at zero delay, and hence can be used to determine maximum pump-probe overlap.

7.3 Semiconductor response

7.3.1 Spectral features

Figure 7.4 shows a typical set of differential absorption spectra at zero time delay. This particular set is for a 21 MW/cm^2 pump pulse that is 8.85 meV below the hh-exciton resonance, as in figure 7.4. With a co-circulary polarized probe (upper graph), one sees a decrease in absorption at the hh-exciton position (1.483 eV) and an increase in absorption to its high-energy side. This corresponds to a blueshift of
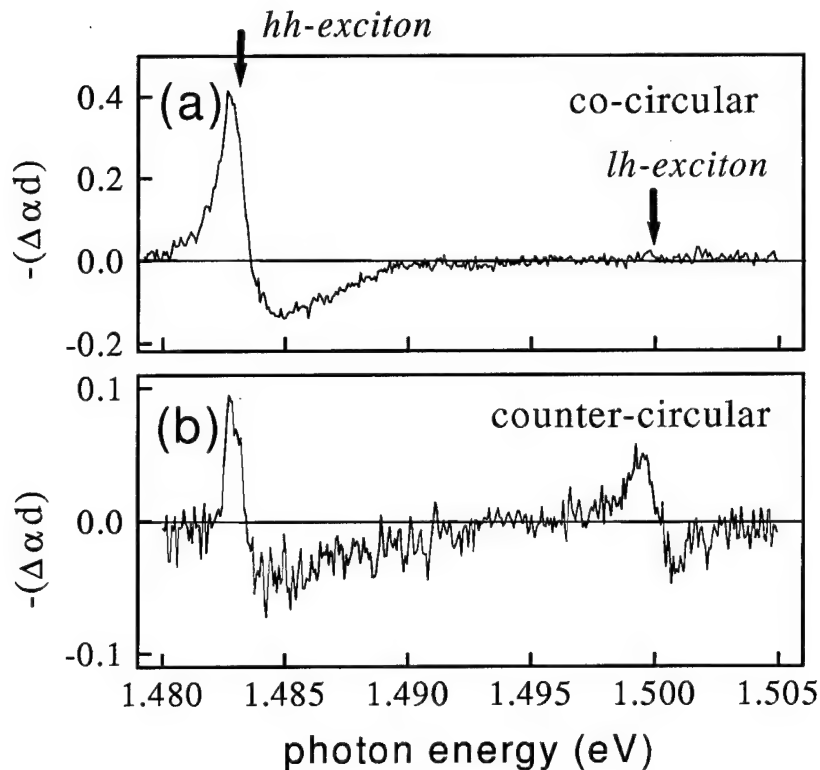
Figure 7.4: Differential absorption spectra showing the sample response at 21 MW/cm^2 intensity and 8.5 meV pump detuning (as in Figure 7.1). Part (a) shows a change in absorption due to the shift of the hh-exciton transition that includes the $m_s = 1/2$ conduction band, while part (b) shows a change due to the shift of the lh-exciton resonance that shares the same conduction band. A hh shift is also seen in part (b) which is due to imperfect probe polarization at the hh position due to quarter waveplate dispersion.

the exciton, and from this data one can determine the center frequency, standard deviation, and total pulse absorption. For some detunings, we observed transient changes in all three variables, corresponding to a Stark shift, broadening, and bleaching respectively, but the latter two changes were too small for meaningful analysis. At the lh-exciton position (1.500 eV) nothing is visible since the lh-exciton state that is being probed is not the one coupled to the Stark shifted hh-exciton. The *change* in absorption is zero. The lower graph shows data for counter-circular polarization. In this case the probe is being absorbed by the same lh-exciton state that is coupled to the hh-exciton. The characteristic differential absorption spectrum for

Stark shifting is visible at both the *lh*-exciton position and the *hh*-exciton position. The probe is made to be perfectly circularly polarized at the *lh*-excition position, so the dispersion of the quarterwave plate leaves some co-circularly polarized light at the *hh*-exciton energy, which accounts for the *hh*-exciton blueshift. A comparison of the Stark shift of the *hh*-exciton, measured with co-circularly-polarized light, to the Stark shift of the *lh*-exciton, measured with counter-circularly-polarized light, gives us insight into the three-state coupling.

7.3.2 Temporal features
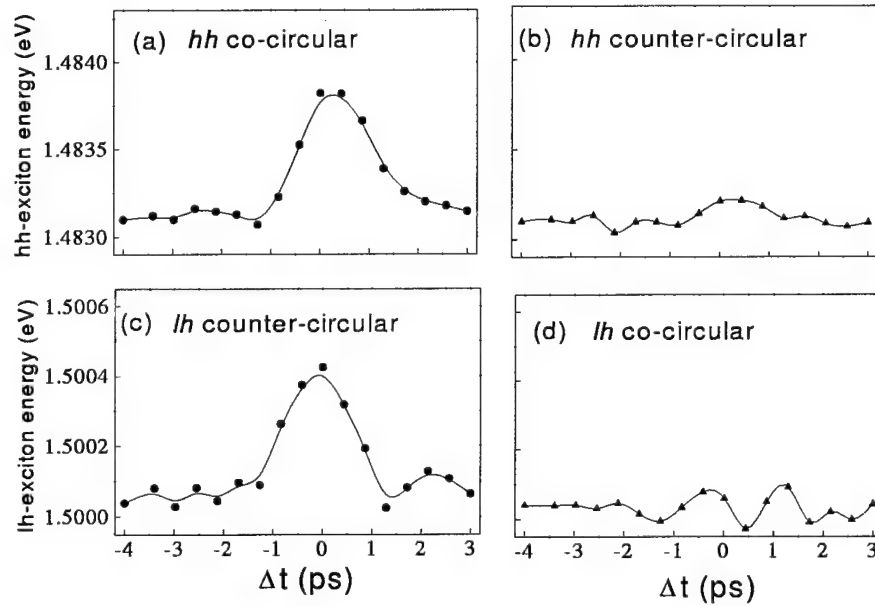
Figure 7.5: Stark shifting as a function of time delay. The left two graphs (a and c) show the exciton resonance shifts for the three-state system in which the *hh*-exciton is dipole coupled to the pump pulse. Note that both the *hh*- and *lh*-exciton Stark shifts are transient and coupled. Graphs (b) and (d) are for the uncoupled three-state system, where the shifts are either small or nonexistant.

The transient Stark shifts lasted for about 2 ps (FWHM), consistent with an adiabatic shift that follows pump intensity. This behavior is clearly evident in Figure 7.5, which shows the shifts of both the *hh*-exciton and the *lh*-exciton with respect to time delay. One can see that both shifts have a similar time behavior,

peaking close to zero time delay. These observations are consistent with a numerical $\chi^{(3)}$ dynamics controlled truncation (DCT) analysis [95]. For the smaller detunings, one could also see a transient broadening and bleaching of the hh-exciton, as shown in Figure 7.6, but these features were not clear enough for unambiguous analysis and did not seem to be coupled to the lh-exciton.
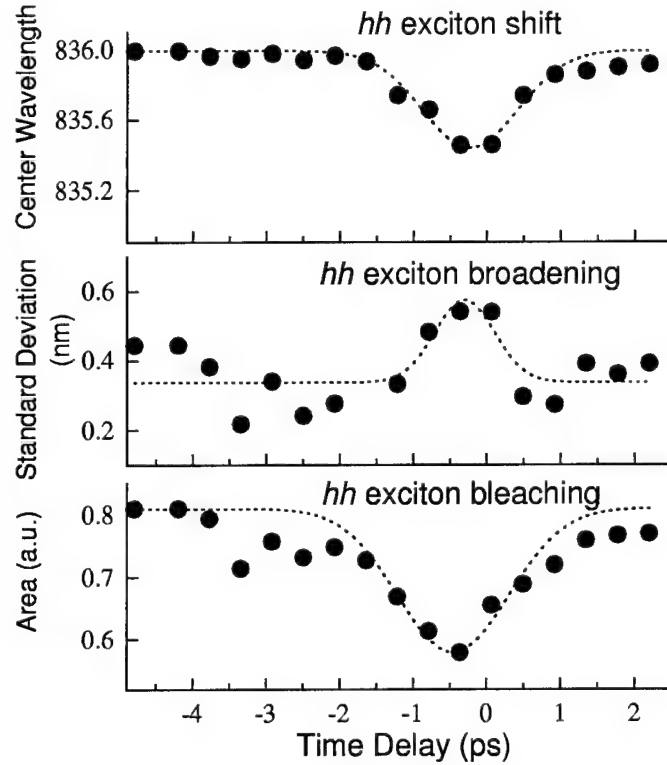

Figure 7.6: In addition to the dynamic Stark shift, transient broadening and bleaching were also present at the hh-exciton resonance for 3.5 meV pump pulse detuning, as shown here. Gaussian fits are included (dotted lines) only as guides to the eye. Transient bleaching was also seen for 5.3 meV pump detuning. We did not measure any corresponding broadening or bleaching of the lh-exciton.

At the two smallest detunings used in this analysis we saw a reshift of the lh-exciton resonance for co-circularly polarized pump and probe. Figure 7.7 shows one such measurement. A corresponding measurement was just reported recently in *Physical Review Letters* by Sieh *et al.* [93]. They reported a redshift of the hh-exciton for counter-circularly-polarized degenerate pump and probe. Thus the probe was interacting with the hh-exciton state which was not dipole coupled to the pump

pulse. The interaction was convincingly attributed to Coulombic memory affects (Coulomb correlations) not present in the Hartree-Fock approximation. In our case, a redshift of the non-dipole coupled *hh*-exciton should correspond to a redshift of the *lh*-exciton that shares the same conduction band; i.e. the one probed by a pulse co-circular with the pump. At least qualitatively, this is what we saw.
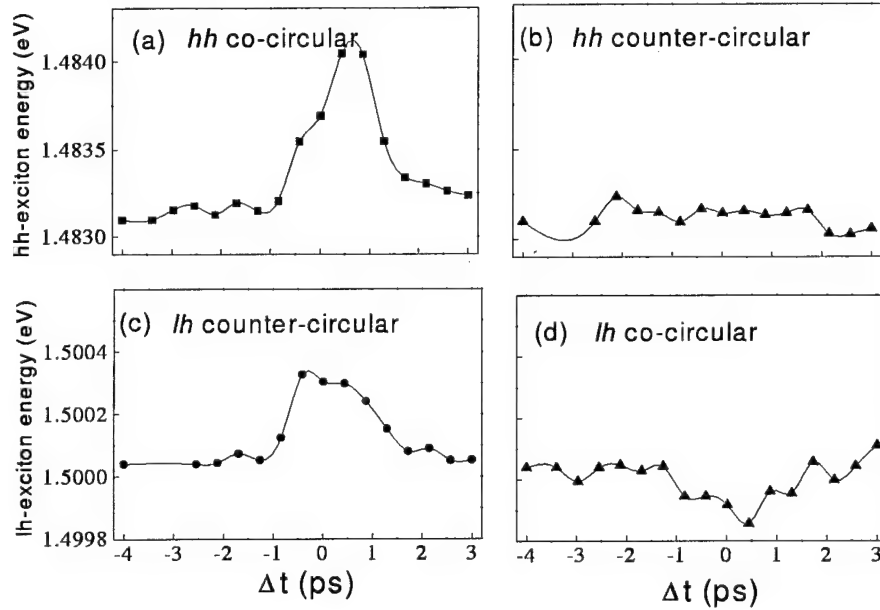

Figure 7.7: Time resolved data for the smallest pump detuning used in this analysis, 3.5 meV. A redshift is observable in the *lh*-exciton resonance (part d of this figure) that is not part of the three-state system under investigation (parts a and c). This redshift is related to Coulombic memory effects not included in the Hartree-Fock approximation.

7.3.3   Shifts as a function of detuning

The magnitude of the dynamic Stark shift as a function of pump detuning is shown in figure 7.8. For the four lowest detunings, the magnitude of the shift decreases with detuning as expected. At a detuning of 8.8 meV, we took two measurements, the second with more intensity since the signal was very small at this point. As expected, a larger Stark shift occurs with a larger pump intensity. For the final data point, at 10.6 meV detuning, the intensity is also at the larger value and the shift
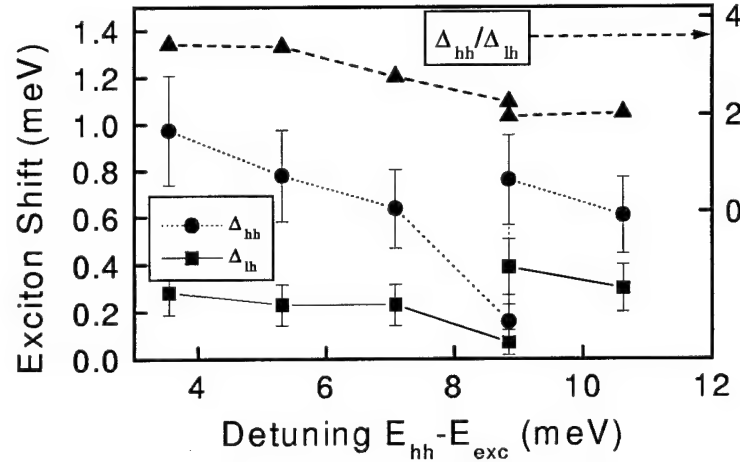
Figure 7.8: Zero delay *lh*- and *hh*-exciton Stark shifts versus detuning. The ratio of *hh*-exciton shift to *lh*-exciton shift, which is 2:1 in pure three-state theory, is plotted as triangles. The ratio very close to this for the largest detunings, but the influence of many-body affects is evident for smaller detunings. The observed increase in the ratio is not present in Hartree-Fock calculations.

is less than for the same intensity with 8.8 meV detuning.

In an analogous atomic three-state system, the probed shift is expected to be half of the pump shift since one energy level is shifted rather than both. At the largest two detunings, where higher order interactions should be the least important, we see a ratio of *hh* to *lh* shift very close to 2:1. As the pump gets closer in energy, however, to the *hh*-exciton resonance, the ratio is seen to increase. This behavior is consistent with recent calculations on many-body effects in the coherent $\chi^{(5)}$ limit [94], assuming that the shift of the *hh*-exciton resonance to higher energies from these effects does not affect the *lh*-exciton absorption. Due to the relatively large experimental uncertainty of the shifts, the shift ratios we have calculated could potentially be inaccurate.

7.4 Conclusions

The measurements presented in this chapter are the first made specifically to study the coupled Stark shifts of two excitons whose interaction can be explained by three-state dynamics. Data included herein shows that the shifts are clearly cou-

pled coherent transients. The ratio of hh-exciton shift to lh-exciton shift appears consistent with many-body calculations, and is consistent with a simple three-state model for larger detunings. A careful numerical analysis is being made by Prof. Binder's group which will be published along with these results [95].

The next step in exploring three-state semiconductor dynamics is to strongly pump both transitions to achieve a significant intervalence-band coherence. This coherence leads to a dressed set of eigenstates which includes a non-interacting "dark" state, as explained earlier in this dissertation. In semiconductors, many interesting effects are expected because of the intervalence-band coherence, including adiabatic population transfer, gain without inversion, and three-band Rabi oscillations [96, 97]. We have made some initial pump-pump-probe measurements which remain to be analyzed, while our unsuccessful pump-pump measurements to observe dark states are described in the next chapter.

CHAPTER 8

DARK STATES MEASUREMENTS

8.1   Overview

Pump-pump and pump-pump-probe measurements are direct attempts to observe three-state dynamics in the strongly-dressed regime. They differ only in the inclusion of a third pulse to probe the material response; in the absence of this third pulse, one or both of the pump pulses double as probes. The advantages of adding the probe pulse are that the probe-pump delay need no longer be the same as the pump-pump delay, and the material response at both exciton resonances can be probed with differential transmission. We have only recently added the probe pulse capability, so our previous attempts have been pump-pump measurements.

In June and July of 1998 we made collinear pump-pump transmission measurements with 150 fs pulses resonant with widely separated lh- and hh-excitons. We went to a non-collinear arrangement and added a pulse-shaper in August, enabling us to make differential transmission (DTS) measurements. Our initial measurements with this setup were the Rabi oscillations measurements described in Chapter 6, where only one pulse was intense. In September 1998 we added a second pulse shaper and changed to a sample with more a more pronounced lh-exciton resonance in hopes of resolving the absorption change expected from formation of the dark state. Meanwhile, Prof. Binder made some theoretical calculations that highlighted the difficulty of observing the expected decrease in absorption with our samples, so we shifted our emphasis to capitalizing on our Rabi oscillations results and other experiments. In the spring of 2000 we added a broad-band probe to the pump-pump setup. This added capability may eventually enable the observation of dark states, either through a decrease in absorption or through some other indicator.

In this chapter, I present the results of the 1998 dark-states experiments along with results of corresponding numerical computations. The experiments were consistent with the computations; however, the decrease in absorption we expected from previous computations (Ref. [35]) was theoretically absent for our first sample, and too small to resolve for our second sample. Consistent with the theoretical analysis, we did not see evidence of a dark state. In the near future, we will be analyzing newly acquired non-resonant two-color pump-pump-probe data for evidence of dark states.

8.2   Previous work on three-state nonradiative coherences

The earliest experimental evidence of the three-state coherences that give rise to dark states comes from W. E. Bell and A. L. Bloom in 1961 [98]. Their experiments studied population trapping achieved by optically driving r. f. transitions between magnetic sublevels. The early atomic experiments primarily used sodium vapor and cw dye lasers, observing the flourescence which is proportional to excited state density [99, 100]. Fluorescence is a useful probe in atomic systems (gasses or beams) since the atomic lifetime can exceed the decoherence time. The signature of population trapping, as reported by Arimondo and Orriols, is that "the fluorescent light disappears when the hyperfine splitting matches the frequency separation between the laser modes." [12] This is the dark state condition where the destructive interference between the uncoupled (ground) states is manifest.

K.-J. Boller, A. Imamoğlu and S. E. Harris were the first to observe electromagnetically induced transparency when, in 1991, they used dye lasers to excite three-state Sr vapor transitions in the ultraviolet [101]. They reduced absorption in the vapor from e^{-20} to an amazing e^{-1}.

Lasing (actually amplification) without inversion was achieved nearly simultaneously by two groups in 1993. A. Nottelman, C. Peters, and W. Lange used a train of picosecond pulses to induce a coherence between Zeeman levels in a vapor of atomic samarium [102]. W. E. van der Veer et $al.$ applied a two step process to cadmium-112 isotopes in a vapor cell subject to a magnetic field [32]. Their experiment used

two dye lasers pumped by a Q-switched Nd:YAG laser. The first laser (doubled to 326 nm) pumped the Cd to a coherent superposition of two ground-state levels, while the second laser (479 nm) served to pump both transitions in the three level system.

8.3   Theoretical predictions and dark-state experiments

In *Physical Review Letters*, 14 August 1995, M. Lindberg and R. Binder predicted that a decrease in absorption due to the creation of dark states could be observed in ultrafast pump-pump experiments [35]. Numerical SBE computations showed that a minimum in absorption at the *hh*-exciton energy should occur when the equal detuning condition allows for the existance of dark eigenstates. The computations modeled two counter-circularly-polarized 200 fs optical pulses, near-resonant with GaAs quantum well *lh*- and *hh*-excitons respectively. The *lh-hh* splitting was 38.5 meV. Detuning of the σ_+ pulse from the *lh*-exciton resonance was fixed at 5, 7.5, and 10 meV, while the σ_- pulse was scanned on either side of the equal detuning condition. Changes in absorption were about 4% for 10 meV detuning and 10% for 5 meV detuning.

In 1992, J. B. Stark, W. H. Knox, and D. S. Chemla had done absorption measurements similar to the dark-states experiments proposed by Lindberg and Binder. They used magnetoexcitons in quantum wells to create a three-band system [103], but they used a weak, broad-band probe on one of the transitions, so they could not expect to induce a significant coherence. No experimental evidence for semiconductor dark states has surfaced to date.

8.4   Collinear broad pump experiments

Figure 8.1 shows the sample spectrum, pulse spectra, and selected results from our first pump-pump experiments. We chose the InGaAs MQW sample that we used because of its large *lh-hh* splitting of 31 meV (18.5 nm), which is nonetheless smaller than that used in the Lindberg and Binder paper. At about 150 fs, our
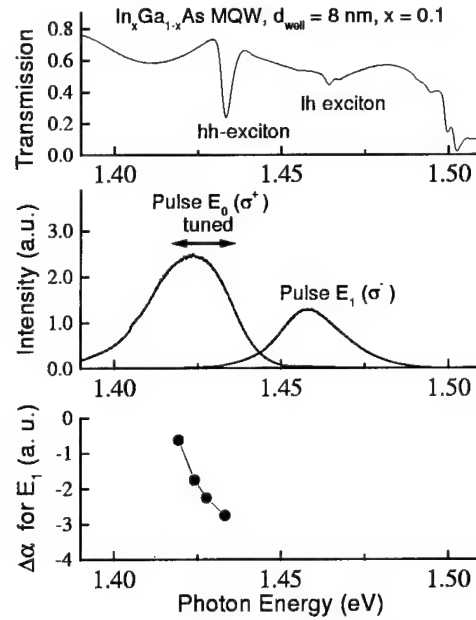
Figure 8.1: Sample and pulse parameters and experimental results for dark states measurements with unshaped pulses. The top graph shows sample transmission characteristics. The sample is the same as for the Rabi oscillation measurements described in Chapter 6. Next are the spectra for the two pump pulses. Finally, each of the four data points in the bottom graph represent the change in absorption of pulse E_1 when pulse E_0 is centered at the corresponding photon energy.

pulses were also somewhat shorter (and spectrally broader) than those used for the numerical calculations. As one can see from the graph of the pulse spectra, there is some overlap at the spectral wings. The bottom graph in Fig. 8.1 shows differential absorption versus the spectral position of the σ_+ pulse that was near resonant with the hh-exciton. No local minimum is seen when detuning is equal; instead, bleaching is seen to increase with σ_+ photon energy. Since an increase in σ_+ photon energy corresponds to increasingly more electrons excited into the hh-exciton continuum, this result is not surprising. Any local minimum due to formation of dark states was unresolvable. This result held for all of our measurements at various detunings of the σ_- pulse and at various pump intensities.

Prof. Binder made theoretical computations closer to our sample parameters and got the results of Fig. 8.2. His computations were consistent with our measurements. It appears that the sample and pulse characteristics of this particular experiment
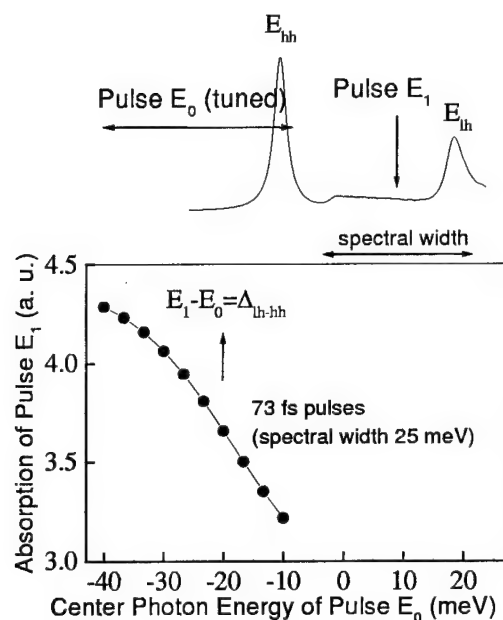
Figure 8.2: Theoretical absorption for conditions similar to those of Fig. 8.1. This graph can be compared directly with the bottom graph of that figure, and the trends are identical in both. Photon energies are given relative to the band edge.

were inadequate to see changes in absorption due to dark state formation regardless of signal-to-noise ratio. Therefor we looked for a more promising sample and took measures to spectrally and temporally shape the pulses.

8.5 Collinear shaped pump experiments

With the addition of two pulse shapers, we spectrally narrowed the pump pulses to achieve better spectral separation while switching to a sample with larger lh-exciton absorption. The absorption spectra of the new sample (the same as used in the Stark shifting measurements) and the shaped pulses are shown in Fig. 8.3.

Theoretical calculations made to match the new pulse and sample conditions are shown in Fig. 8.4. Pulse E_1 is made near resonant with the lh-exciton and sits in the hh-continuum. The detuning is selected to be favorable for dark-state formation. The flat lines at the top show the baseline absorption of pulse E_1 (no hh pump). The scale at the right is for a lower intensity lh pump pulse (E_1) while the left scale is for a higher intensity lh pump pulse. The difference is due to the amount of
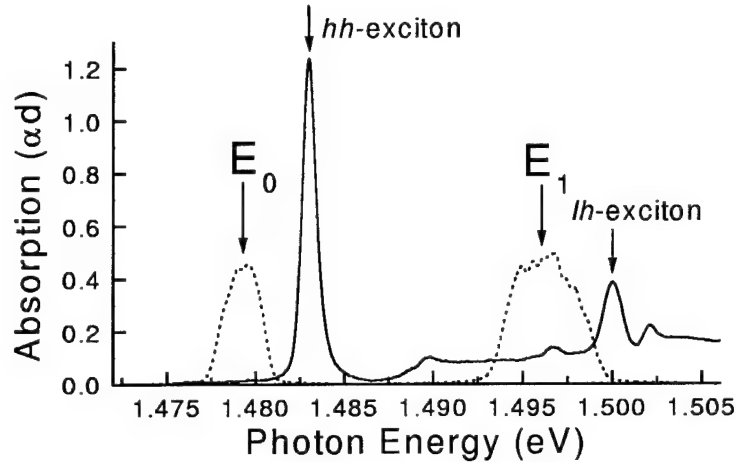
Figure 8.3: Sample absorption and shaped pulse spectra. The sample whose spectrum is shown is the same as used in the Stark shifting experiments explained in Chapter 7. Both pulses shown are shaped by pulse shapers to spectral widths of 2.6 meV and 4.9 meV respectively. They are oppositely-circularly-polarized.

spectral hole burning. In the case of the lower intensity lh pump, an equal intensity hh pump causes a monotonic decrease in absorption with detuning over the range shown, similar to our previous measurements. For higher intensity pumps, however, we see the characteristic absorption minimum at equal pump detunings. The dip observed, however, is less than 1% of the initial absorption, which was definitely too small for us to measure. These results prompted us to introduce the CCD camera with which we could compensate for shot-to-shot light energy fluctuations.

8.6   Future Direction

Even with the CCD camera, a sub-1% change in absorption is probably just beyond our ability to measure. Unless the dark-state effect has been underestimated in theory, we will probably need to explore other pump and/or sample conditions. A higher repetition rate laser system would allow better signal-to-noise, but creates additional problems with incomplete sample recovery from local heating between pulses. However, with the addition of the super-continuum probe, we can now time-resolve the pump-pump interaction. This allows us to explore new dynamics and perhaps other dark-state signatures. Other coherent three-state interactions like
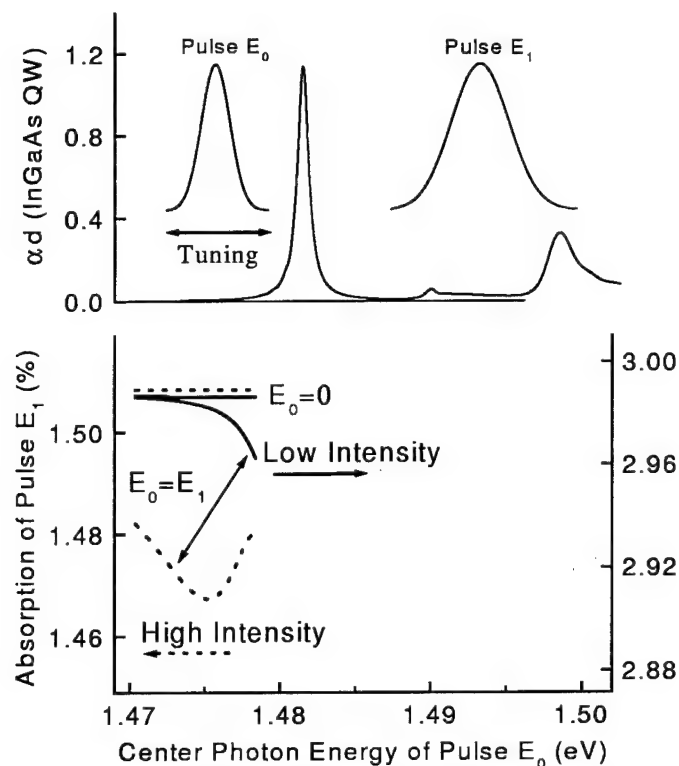
Figure 8.4: Theoretical absorption for the conditions of Fig. 8.3. The solid lines correspond to a lower intensity set of pump pulses and should be associated with the axis scale on the right side, while the dashed lines correspond to a higher intensity set of pulses and the left axis scale. Both flat lines show the absorption of E_1 when E_0 is absent. The curved lines show absorption of pulse E_1 with two pumps of equal intensity.

three-band Rabi oscillations [97] may also be possible with the pump-pump-probe setup. We have already made our first pump-pump-probe measurements, and are currently analyzing the data.

APPENDIX A

THE BEREK COMPENSATOR AND PHASE MATCHING

In general, the linear dielectric tensor for a homogeneous, lossless, non-magnetic medium is symmetric ($\epsilon_{ij} = \epsilon_{ji}$). This is a consequence of conservation of engergy [39, p. 666]. This symmetry guarantees that we can diagonalize the dielectric tensor by transforming to the principal axes [104, pp. 201–201]. In this system of axes, we can write the electrical energy density of a light wave transitting the medium as

$$u_{elec} = \frac{1}{2}\mathbf{E} \cdot \mathbf{D} \tag{A.1}$$

$$= \frac{1}{2}\left(\frac{D_x^2}{\epsilon_{xx}} + \frac{D_y^2}{\epsilon_{yy}} + \frac{D_z^2}{\epsilon_{zz}}\right). \tag{A.2}$$

Defining Cartesian coordinates $X \equiv D_x/\sqrt{2\epsilon_0 u_{elec}}$, $Y \equiv D_y/\sqrt{2\epsilon_0 u_{elec}}$, $Z \equiv D_z/\sqrt{2\epsilon_0 u_{elec}}$ and using principal refractive indices $n_i^2 = \epsilon_{ii}/\epsilon_0$ $(i = x, y, z)$, we have the equation of the ellipsoid of wave normals (index ellipsoid)

$$\frac{X^2}{n_x^2} + \frac{Y^2}{n_y^2} + \frac{Z^2}{n_z^2} = 1, \tag{A.3}$$

which is equivalent to the energy density equation and represents the locus of allowed values of the components of the electric diplacement vector $\mathbf{D}$.

For a uniaxial crystal, as are used in the Berek Compensator and in the OPAs, two of the principal refractive indices are identical, customarily $n_x = n_y = n_o$ (for ordinary) and $n_z = n_e$ (for extraordinary). The ellipsoid of wave normals must then be axially symmetric about the Z axis (an ellipsoid of revolution). For a light wave travelling in the Z direction, [1] symmetry requires the phase velocity be the

---

[1]The wavefront travels normal to $\mathbf{D}$, thus the crossing points of the wavevector and the ellipsoid are allowed wave normals. Energy travels in yet another direction normal to the electric field $\mathbf{E}$, which limits the interaction length of initially collinear beams.

same for both components of **D**. The direction of the Z axis is called the optic axis. The crystal plate used in the Berek Compensator is cut perpendicular to this axis, which does not change with dispersion. [2] If the plate is tilted relative to the light beam, this symmetry is broken, and two orthogonal components of **D** travel at different phase velocities; we say that one component is retarded relative to the other. Without loss of generality we can define the X and Y axes anywhere in the X–Y plane, so we make $D_y \propto Y = 0$ for a particular light wave passing through the compensator, leaving

$$\frac{X^2}{n_o^2} + \frac{Z^2}{n_e^2} = 1 \tag{A.4}$$

(see Figure A.1). The refractive index of the component that is always normal

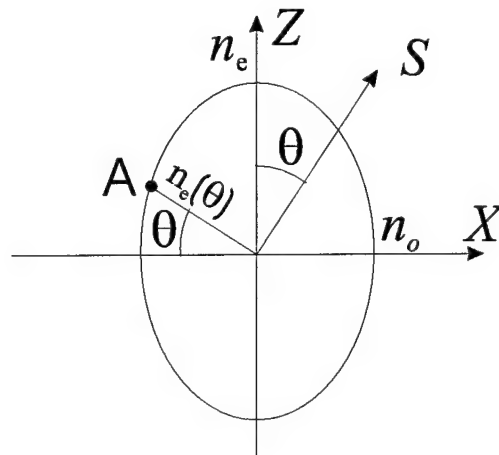Figure A.1: Ellipse of wave normals, which allows the calculation of the extraordinary index of refraction versus tilt angle θ. **S** is the Poynting vector.

to the optic (Z) axis, D_y, is not determined by this equation (since we assumed it away), but it must be n_o since D_y remains the same for any value of θ, and is n_o when $\theta = 0$ (symmetric situation with both components the same). This component is called the o-wave, and

$$n_o(\theta) = n_o. \tag{A.5}$$

---

[2] In monoclinic and triclinic crystals, the direction of the principal axes do change [39, p. 667]

Point A on Figure A.1 shows the allowed values of $X = D_x/\sqrt{2\epsilon_0 u_{elec}}$ and $Z = D_z/\sqrt{2\epsilon_0 u_{elec}}$. From the figure

$$X = n_e(\theta)\cos(\theta) \tag{A.6}$$

$$Z = n_e(\theta)\sin(\theta) \tag{A.7}$$

$$\frac{1}{n_e^2(\theta)} = \frac{\cos^2(\theta)}{n_o^2} + \frac{\sin^2(\theta)}{n_e^2}. \tag{A.8}$$

The tilt angle of the Berek compensator corresponds to θ in the above equations. We have shown that the refractive index of the component shown in Figure A.1 (the e-wave) varies with the tilt angle, so this component has variable retardance. We tilt the crystal so that the difference in indices causes one quarter wave delay over the length of the crystal. Then, when we rotate the crystal to a $\pm 45°$ angle with respect to the Y axis as defined above, we get circularly polarized light. Due to the finite bandwith of the input light wave and the dispersion of the crystal, we cannot even in principle get perfect circular polarization, but the Berek compensator works quite well, as tests detailed in the next subsection show.

The angle tuning in the OPAs is collinear, so the analysis above applies directly. There are two inputs, a broadband (supercontinuum) seed and the 800 nm ($\omega_3 = 3.75 \times 10^{14}$ Hz) pump. There are two orthogonal outputs,[3] called the signal and the idler, at angular frequencies ω_1 and ω_2. Conservation of energy requires

$$\omega_3 = \omega_1 + \omega_2, \tag{A.9}$$

while conservation of momentum (phase matching condition) requires[4]

$$\mathbf{k}_3 = \mathbf{k}_1 + \mathbf{k}_2 \tag{A.10}$$

$$\omega_3 n(\omega_3) = \omega_1 n(\omega_1) + \omega_2 n(\omega_2) \tag{A.11}$$

The broadband seed is horzontally polarized, an o-wave, with an angle independent (but frequency dependent) refractive index. The pump, however, is polarized as an

---

[3]Two orthogonal outputs (or inputs) constitutes Type II phase matching; the parallel case is called Type I.

[4]Momentum conservation is not strict, as can be seen in the results of Subsection 5.3.1.

e-wave, so that the index depends on the angle. Only a narrow band of frequencies within the seed continuum is amplified, i.e. those that can conserve both energy and momentum in conjunction with the idler. By rotating the BBO crystal, we are frequency selecting by using the tilt dependent extraordinary index of refraction.

A similar situation exists in the sum frequency generation and second harmonic generation that we use for cross-correlation and autocorrelation respectively. In these cases, however, the inputs are parallel (Type I phase matching). Since refractive index increases with frequency away from absorption resonances, the inputs must be o-waves for a negative uniaxial crystal like BBO.[5] This just means we have to use a crystal that tilts in the plane normal to our input polarization, and we are tilting the crystal to change the sum frequency or second harmonic refractive index to the phase matching condition.

---

[5]In our experiments, ω_1 and ω_2 are close, so roughly we need $n_e(\omega_3) = n_o(\omega_1)$. In a negative uniaxial, $n_o(\Omega) > n_e(\Omega)$

APPENDIX B

ESTIMATION OF PULSE CHIRP

Ultrashort pulses are created by the superposition of Fourier components across a wide spectral bandwidth. The shortest pulses for a given spectral bandwidth occur when all of the Fourier components have a common phase at one point in space, and these pulses are called bandwidth limited, Fourier limited, or unchirped. Mode-locking produces bandwidth limited pulses by creating a condition in which only those laser modes with a common phase at one point in space are amplified in the laser cavity. Once our mode-locked seed pulses leave the laser, however, they are chirped by travelling through glass, by reflecting off mirrors, and by focusing. We will briefly examine the affect of each of these.[1]

First we will consider the propagation of our pulses through the glass used in the pulse shapers and focusing lenses. From Maxwell's equations we can derive a wave equation for the electric field

$$\left(\nabla^2 - \frac{1}{c^2} \frac{\partial^2}{\partial t^2} \right) \mathbf{E}(\mathbf{r}, t) = \mu_0 \frac{\partial^2}{\partial t^2} \mathbf{P}^{(1)}(\mathbf{r}, t), \tag{B.1}$$

where we have included only the polarization $\mathbf{P}^{(1)}$ that varies linearly with the electric field $\mathbf{E}$ (i.e. nonlinear optical processes are ignored). We will ignore transverse field variations, which amounts to ignoring diffraction in the linear regime. Since glass is isotropic and homogeneous, we can write a scalar wave equation

$$\left(\frac{\partial^2}{\partial z^2} - \frac{1}{c^2} \frac{\partial^2}{\partial t^2} \right) E(z, t) = \mu_0 \frac{\partial^2}{\partial t^2} P^{(1)}(z, t). \tag{B.2}$$

---

[1]These concepts are covered in much more detail in Reference [49, pp. 1–40, 50–99].

Fourier transforming this equation from t to Ω, we can write

$$\left(\frac{\partial^2}{\partial z^2} + \frac{\Omega^2}{c^2}\right)\tilde{E}(z,\Omega) = -\mu_0\Omega^2\tilde{P}^{(1)}(z,\Omega) \tag{B.3}$$

$$= -\mu_0\Omega^2\epsilon_0\chi^{(1)}(\Omega)\tilde{E}(z,\Omega) \tag{B.4}$$

$$\left(\frac{\partial^2}{\partial z^2} + \frac{\Omega^2}{c^2}n^2(\Omega)\right)\tilde{E}(z,\Omega) = 0, \tag{B.5}$$

where we used $\tilde{P}^{(1)}(z,\Omega) = \epsilon_0\chi^{(1)}(\Omega)\tilde{E}(z,\Omega)$ and $n^2(\Omega) = 1 + \chi^{(1)}(\Omega)$. The solution to this equation yields:

$$\tilde{E}(z,\Omega) = \tilde{E}(0,\Omega)e^{ik(\Omega)z} \tag{B.6}$$

with the dispersion relation

$$k(\Omega) = \frac{\Omega}{c}n(\Omega). \tag{B.7}$$

We expand the propagation constant $k(\Omega)$ in a Taylor's Series about a carrier frequency ω_c:[2]

$$k(\Omega) = k(\omega_c) + (\Omega - \omega_c)\left.\frac{\partial k}{\partial\Omega}\right|_{\omega_c} + \frac{1}{2}(\Omega - \omega_c)^2\left.\frac{\partial^2 k}{\partial\Omega^2}\right|_{\omega_c} + \cdots. \tag{B.8}$$

We can identify $\partial k/\partial\Omega|_{\omega_c}$ as the inverse of the group velocity evaluated at the carrier frequency, $1/v_g$, and write the solution for the electric field as:

$$\tilde{E}(z,\Omega) = \tilde{E}(0,\Omega)e^{ik_c z}e^{i(\Omega-\omega_c)\frac{1}{v_g}z}e^{i(\Omega-\omega_c)^2\frac{-1}{2v_g^2}v_g'z}, \tag{B.9}$$

where we have used the abbreviations $k_c \equiv k(\omega_c)$ and $v_g' \equiv \partial v_g/\partial\Omega|_{\omega_c}$ The first phase factor corresponds to a dispersionless wave, where all Fourier components travel at the phase velocity $v_\phi = \omega_c/k_c = c/n(\omega_c)$. Clearly a wave envelope with only this phase factor maintains its shape at all points in space and travels at the phase velocity.

---

[2]We can advantageously introduce a carrier frequency if the carrier frequency is much larger than the pulse bandwidth. We have $\omega_c/\Delta\omega_p \approx 85$. This is equivalent in the time domain to the requirement that the pulse envelope contain many optical cycles, where we have $\Delta\tau_p/T_c \approx 37$. These requirements are connected by the bandwidth limited Gaussian pulse relationship $(\Delta\tau_p)(\Delta\omega_p) = 2\pi(0.44) = 2\pi(37)/(85)$.

To understand the affect of the second phase factor, imagine moving in a reference frame at the group velocity ($t' = t - z/v_g$). In such a frame, the frequency dependence of the second phase factor vanishes.[3] Although all of the Fourier components move at different phase velocities, they all maintain the same phase in the group velocity frame as long as the derivative of the propagation constant (or refractive index) is constant. The pulse moves at the group velocity and does not change shape.

Finally we get to chirp. The third phase factor (and higher order ones) depend on the change of the group velocity with respect to frequency. With more than one group velocity, the pulse must spread. This effect is called group velocity dispersion, GVD. In effect, the red Fourier components travel faster than the blue.

Now we can estimate the effect of the glass in our system on pulse chirp. This difference in group velocities contained in our pulses can be estimated as:

$$\Delta v_g = \left. \frac{\partial v_g}{\partial \Omega} \right|_{\omega_c} \Delta \omega_p = k_c'' v_g^2 \Delta \omega_p, \tag{B.10}$$

where we have written k_c'' for $\partial^2 k / \partial \Omega^2 |_{\omega_c}$. Traversing a distance L, the spread becomes

$$\Delta \tau_p = \Delta \left(\frac{L}{v_g} \right) = L \frac{\Delta v_g}{v_g^2} = L k_c'' \Delta \omega_p. \tag{B.11}$$

Using values applicable to our experiments, $L \approx 1$ cm, $k_c'' \approx 4.5 \times 10^{-26} \mathrm{s}^2/\mathrm{m}$ for BK7 glass at 800 nm wavelength, [4] and $\Delta \omega_p \approx 2\pi c \Delta \lambda / \lambda^2 \approx 3 \times 10^{13}$ rad/s, we calculate a pulse spread of about 15 fs due to glass (lenses and filters).

Next we consider mirrors. Mirrors are generally a problem when used in an oscillator, where the cavity photon lifetime can equate to many round trips [49, p. 51]. Multilayer dielectric mirrors are generally used for oscillators because they can have much higher reflectivities and lower losses than metal mirrors. We use dielectric mirrors within the Ti:Sapphire laser, between the Ti:Sapphire laser and the regenerative amplifier, and between the regenerative amplifier and the OPAs

---

[3]According to the shift theorem of Fourier transform theory, $\mathcal{F}\{E(t - z/v_g)\} = \mathcal{F}\{E(t)\} \exp(i\Omega z/v_g)$.

[4]The value for k_c'' is calculated from $n''(\lambda_c)$ given in Reference [49, p. 44].

and for the same reasons. After the OPAs, however, all of our mirrors are either silver or gold coated.[5]

We can ignore the chirp generated within the Ti:Sapphire laser based on laser design. The mode locking mechanism ensures that all modes are nearly phased together, which means a nearly bandwidth limited pulse. Furthermore, to get short pulses, the GVD generated by the glass and mirrors in the laser is already compensated for by a prism arrangement which creates GVD opposite to the optical elements.

Within the regenerative amplifier we can also ignore chirp. As explained in Appendix E this amplifier intentionally chirps the pulse, amplifies it linearly, and recompresses the pulse to near bandwidth limited. Since some of the bandwidth is lost, the amplified pulse is usually 20% longer than the input.

The OPAs and the mirrors inbetween the elements just considered are a little more complicated. The optical parametric amplification process determines pulse bandwidth in a complicated way, which depends on phase mismatching, pump beam divergence, pump bandwidth, power broadening, and temperature broadening [106, pp. 14–16, 43–47]. Dielectric mirrors can be multilayer quarterwave stacks or more complicated structures based on the interference of light reflected from each of the layers, [107, pp. 5-14] which generates a wavelength dependent phase response [49, p. 51]. If the pulse length is comparable to the multilayer thickness, it is possible to have significant pulse reshaping [108]. Our pulse length is around 100 fs, corresponding to 30 μm in air or 150 quarter-wavelengths at 800 nm. This is many more layers than a typical dielectric coating [107, p. 5–13]. While it is possible to measure the chirp of individual elements in our laser-amplifier system, it does not seem useful at this point.

The last possible source of chirp we will consider here is focusing. It is well known from lens design that the dispersion of glass in a lens creates a wavelength dependent focal plane. This deviation from ray optics is known as chromatic aberration; it

---

[5]We need not consider chirp for gold or silver mirrors since both are excellent conductors with skin depths on the order of 10 nm at wavelengths of 800 nm [105, p. 377].

derives from the index variation and hence the phase velocity. The result of this aberration is that broadband light, such as an ultrashort pulse, cannot be focused as tightly as more monochromatic light. This is a transverse broading, and thus it is not chirp. It is explained in detail in Section 5.4 (Pulse focusing and overlap) and mentioned here because it is the spatial analog of temporal broadening. In the limit that the broadening is much more than the original width, the fractional broadening, both spatial and temporal, is given by the same equation to within a constant of order unity for Gaussian beams [49, pp. 61–62].

For pulses (wave packets), the energy front travels at the group velocity and the phase front travels at the phase velocity, so the pulse energy does not arrive from different lens radii simultaneously at the focus.[6] The energy fronts from the beam at radius r arrive earlier than those from the center of the beam (radius r_0) due to a difference in travel distance through the glass of the lens. Using v_ϕ and v_g for the phase and group velocities respectively, and $L(r)$ for the lens thickness at radius r, we can write the time difference as:

$$\Delta T(r) = \left(\frac{1}{v_g} - \frac{1}{v_\phi} \right) (L(r_0) - L(r)) \tag{B.12}$$

$$= \left(\frac{1}{v_g} - \frac{1}{v_\phi} \right) \frac{r^2}{2} \left(\frac{1}{R_1} - \frac{1}{R_2} \right). \tag{B.13}$$

The substitutions made in equation B.13 are based on the geometry of Figure B.1 and the assumption of a thin lens. Using the identities[7] $1/v_\phi = n/c$ and $1/v_g = (n - \lambda dn/d\lambda)$ we can express the time difference as:

$$\Delta T(r) = -\frac{r^2}{2} \frac{\lambda}{c} \frac{dn}{d\lambda} \left(\frac{1}{R_1} - \frac{1}{R_2} \right). \tag{B.14}$$

If we further recognize that the power of a thin lens is given by

$$\frac{1}{f} = (n - 1) \left(\frac{1}{R_1} - \frac{1}{R_2} \right), \tag{B.15}$$

---

[6]By Fermat's Principle the phase fronts arrive simultaneously at the focus. Since the amount of glass traversed by a ray depends on its radial distance from the lens center, and the phase and group velocities differ (appreciably) only in the glass, the pulse energy, which travels at the group velocity, is delayed more in the center of the lens than toward the edge of the lens.

[7]The second equation can be derived using $1/v_g = \partial k/\partial \Omega$ and $k = n\Omega/c = 2\pi/\lambda$.

$$L(r) = \delta_1 - \delta_2$$

$$\delta_1 = R_1 - \sqrt{R_1^2 - r^2} \approx \frac{r^2}{2R_1}$$

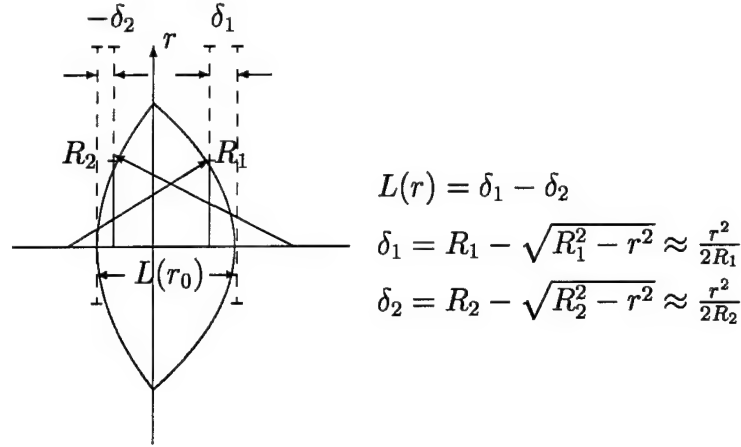$$\delta_2 = R_2 - \sqrt{R_2^2 - r^2} \approx \frac{r^2}{2R_2}$$

Figure B.1: The geometry relating equation B.12 to equation B.13. The lens is drawn as a thick lens for clarity, although the approximation applies only to a thin lens. The sign convention used has $R_1 > 0$ and $R_2 < 0$.

we can express the time diffence as:

$$\Delta T(r) = -\frac{r^2\lambda}{2c}\left(\frac{1}{f(n-1)}\right)\frac{dn}{d\lambda} \qquad (B.16)$$

$$= \frac{r^2\lambda}{2c}\frac{d}{d\lambda}\left(\frac{1}{f}\right). \qquad (B.17)$$

The final expression shows how the time difference is related to the chromaticity of the lens, $d(1/f)/d\lambda$. Equation B.16 can be compared to equation D.2 which relates the focal point spread to the chromaticity. Inserting numbers into equation B.16 that approximate the focusing on the sample, $r = 2$ mm, $\lambda = 800$ nm, $f = 15$ cm, $n = 1.5$, and $dn/d\lambda = -2.0 \times 10^{-2}$ μm^{-1}, we get a negligable pulse spreading of 1.4 fs. Note that, unlike the chirp due to the glass itself, this spreading is due to the first derivative of the refractive index (or propagation number) with respect to frequency (or wavelength) and is independent of the pulse's initial temporal and spectral widths.

APPENDIX C

THE PHYSICS BEHIND THE AUTOCORRELATOR

This appendix examines the physics behind the second harmonic generation autocorrelator and its phase matching requirement using an electromagnetic wave approach.[1] We start with extending equation B.1 to second order polarization and allowing the medium to be anisotropic:

$$\left(\nabla^2 - \frac{1}{c^2}\frac{\partial^2}{\partial t^2}\right)\mathbf{E}(\mathbf{r}, t) - \nabla\left(\nabla \cdot \mathbf{E}(\mathbf{r}, t)\right) = \mu_0 \frac{\partial^2}{\partial t^2}\mathbf{P}(\mathbf{r}, t) \qquad \text{(C.1)}$$

where $\mathbf{P}(\mathbf{r}, t) = \mathbf{P}^{(1)}(\mathbf{r}, t) + \mathbf{P}^{(2)}(\mathbf{r}, t)$. This equation applies to all of the Fourier components of the electric field, and we will apply it to the second harmonic signal generated by the combined pulse trains of both arms of the interferometer. We will consider the pulses as quasimonochromatic plane waves with slowly varying envelopes, as labeled in part (b) of Figure 5.8.

$$\mathbf{E}_1(\mathbf{r}, t) = \mathcal{E}_1(\mathbf{r}, t)e^{i(\mathbf{k}_1 \cdot \mathbf{r} - \omega t)}\hat{\mathbf{e}}_1 + c.c. \qquad \text{(C.2)}$$

$$\mathbf{E}_2(\mathbf{r}, t - \tau) = \mathcal{E}_2(\mathbf{r}, t - \tau)e^{i[\mathbf{k}_2 \cdot \mathbf{r} - \omega(t-\tau)]}\hat{\mathbf{e}}_2 + c.c. \qquad \text{(C.3)}$$

where τ corresponds to the time delay introduced by the moving arm of the interferometer and $\hat{\mathbf{e}}_i$, $i = 1, 2, 3$, are the field polarizations of $\mathbf{E}_i$. Furthermore we will assume the input electromagnetic fields to be negligably attenuated by the BBO crystal (so as to ignore coupled waves) and concentrate only on the polarization at

---

[1]The general technique used here follows Y. R. Shen in Reference [46], but he considers monochromatic (cw) plane waves, works in c.g.s. units, and does not address autocorrelation.

the second harmonic frequency that is derived from both interferometer arms.[2]

$$
\begin{aligned}
\mathbf{P}_3(\mathbf{r},t,\tau) &= \epsilon_0 \overline{\overline{\chi}}^{(1)}(2\omega) \cdot \mathbf{E}_3(\mathbf{r},t,\tau) + \epsilon_0 \overline{\overline{\chi}}^{(2)}(-2\omega,\omega,\omega) : \mathbf{E}_1(\mathbf{r},t)\mathbf{E}_2(\mathbf{r},t-\tau) \\
&= \mathbf{P}_3^{(1)}(\mathbf{r},t,\tau) + \left\{ \left[\epsilon_0 \overline{\overline{\chi}}^{(2)}(-2\omega,\omega,\omega) : \hat{\mathbf{e}}_1\hat{\mathbf{e}}_2 \mathcal{E}_1(\mathbf{r},t)\mathcal{E}_2(\mathbf{r},t-\tau) \right] \right. \\
&\qquad \left. \times\, e^{i[(\mathbf{k}_1+\mathbf{k}_2)\cdot\mathbf{r}-2\omega t-\omega\tau]} + c.c. \right\} \qquad\qquad\qquad\qquad \text{(C.4)} \\
&= \mathbf{P}_3^{(1)}(\mathbf{r},t,\tau) + \left\{ \mathcal{P}_3^{(2)}(\mathbf{r},t,\tau) e^{i[(\mathbf{k}_1+\mathbf{k}_2)\cdot\mathbf{r}-2\omega t-\omega\tau]}\hat{\mathbf{e}}_3 + c.c. \right\} \qquad \text{(C.5)}
\end{aligned}
$$

where we have introduced a slowly varying polarization envelope $\mathcal{P}_3^{(2)}(\mathbf{r},t,\tau)$ in equation C.5. We can write the electric field resulting from this polarization, which is what we are interested in, as $\mathbf{E}_3(\mathbf{r},t,\tau) = \mathcal{E}_3(z,t,\tau)\exp[i(\mathbf{k}_3\cdot\mathbf{r}-2\omega t-\omega\tau)]\hat{\mathbf{e}}_3 + c.c.$ where $\mathcal{E}_3$ is the slowly varying field envelope and $\hat{\mathbf{e}}_3$ is the field polarization. We have also defined the z direction through this last definition. The wave equation for the transverse components of the resultant second harmonic electric field is

$$
e^{i(\mathbf{k}_3\cdot\mathbf{r}-2\omega t-\omega\tau)} \left\{ \frac{\partial^2}{\partial z^2} + 2ik_{3,z}\frac{\partial}{\partial z} - \frac{(\overline{\overline{\epsilon_\perp}}(2\omega)\cdot\hat{\mathbf{e}}_3)}{c^2}\left(\frac{\partial^2}{\partial t^2} - 2i(2\omega)\frac{\partial}{\partial t} \right) \right\} \mathcal{E}_{3,\perp}(z,t,\tau)
$$
$$
= e^{i[(\mathbf{k}_1+\mathbf{k}_2)\cdot\mathbf{r}-2\omega t-\omega\tau]}\mu_0\left(\frac{\partial^2}{\partial t^2} - 2i(2\omega)\frac{\partial}{\partial t} - (2\omega)^2 \right) \mathcal{P}_{3,\perp}^{(2)}(\mathbf{r},t,\tau). \quad \text{(C.6)}
$$

We have used $-|\mathbf{k}_3|^2 + (2\omega/c)^2(\overline{\overline{\epsilon_\perp}}(2\omega)\cdot\hat{\mathbf{e}}_3) = 0$ with the definitions $\overline{\overline{\epsilon_\perp}}(2\omega) = \epsilon_0(1+\overline{\overline{\chi}}_\perp^{(1)}(2\omega))$ and $\overline{\overline{\chi}}_\perp^{(1)}(2\omega) = \hat{\mathbf{e}}_\perp\cdot\overline{\overline{\chi}}^{(1)}(2\omega)$.

The longitudinal wave derives from the Maxwell equation $\nabla\cdot\mathbf{D} = 0$ and the constitutive relation $\mathbf{D} = \mathbf{D}_3(\mathbf{r},t,\tau) = \epsilon_0\mathbf{E}_3(\mathbf{r},t,\tau) + \mathbf{P}_3^{(1)}(\mathbf{r},t,\tau) + \mathbf{P}_3^{(2)}(\mathbf{r},t,\tau)$. In terms of the envelope functions, this becomes

$$
\frac{\partial}{\partial z}\left[\left(\overline{\overline{\epsilon_\parallel}}(2\omega)\cdot\hat{\mathbf{e}}_3\right)\mathcal{E}_{3,\parallel}(z,t,\tau)e^{i\mathbf{k}_3\cdot\mathbf{r}} + \mathcal{P}_{3,\parallel}^{(2)}(z,t,\tau)e^{i(\mathbf{k}_1+\mathbf{k}_2)\cdot\mathbf{r}} \right] e^{-i2\omega t}e^{-i\omega\tau} = 0 \quad \text{(C.7)}
$$

where $\overline{\overline{\epsilon_\parallel}}(2\omega)$ is defined analogous to $\overline{\overline{\epsilon_\perp}}(2\omega)$ Using the slowly varying envelope approximations

$$
\left| \frac{\partial^2\mathcal{E}}{\partial z^2} \right| \ll k\left| \frac{\partial\mathcal{E}}{\partial z} \right|, \quad \left| \frac{\partial^2\mathcal{P}}{\partial t^2} \right| \ll \omega^2|\mathcal{P}|, \quad \left| \frac{\partial^2\mathcal{E}}{\partial t^2} \right| \ll \omega^2|\mathcal{P}|, \quad \left| \frac{\partial\mathcal{E}}{\partial t} \right| \ll \omega|\mathcal{P}|, \quad \left| \frac{\partial\mathcal{P}}{\partial t} \right| \ll \omega|\mathcal{P}|
$$
$$
\text{(C.8)}
$$

---

[2]The development that follows, starting with the polarization expression written in the time domain, implies an instantaneous response of the medium. In the transparency region of the BBO crystal, this is a reasonable assumption.

we have solvable equations for both components

$$\frac{\partial}{\partial z}\mathcal{E}_{3,\perp}(z,t,\tau) = i\frac{\mu_0(2\omega)^2}{2k_{3,z}}\mathcal{P}_{3,\perp}^{(2)}(\mathbf{r},t,\tau)e^{i\Delta kz} \qquad (C.9)$$

$$\frac{\partial}{\partial z}\left[\left(\overline{\overline{\epsilon_{\parallel}}}(2\omega)\cdot\hat{\mathbf{e}}_3\right)\ \mathcal{E}_{3,\parallel}(z,t,\tau) + \mathcal{P}_{3,\parallel}^{(2)}e^{i\Delta kz}\right] = 0, \qquad (C.10)$$

with $\Delta\mathbf{k} = \hat{z}\Delta k = \mathbf{k}_1 + \mathbf{k}_2 - \mathbf{k}_3$ being the phase mismatch.[3] Solving these equation for beams entering at $z = 0$ and exiting at $z = L$ we get

$$\mathcal{E}_{3,\perp}(L,t,\tau) = \mathcal{E}_{3,\perp}(0,t,\tau) + \frac{\mu_0(2\omega)^2}{2k_{3,z}\Delta k}\mathcal{P}_{3,\perp}^{(2)}(\mathbf{r},t,\tau)\left(e^{i\Delta kL} - 1\right) \qquad (C.11)$$

$$\mathcal{E}_{3,\parallel}(L,t,\tau) = \mathcal{E}_{3,\parallel}(0,t,\tau) + \frac{\mathcal{P}_{3,\parallel}^{(2)}(\mathbf{r},t,\tau)}{\overline{\overline{\epsilon_{\parallel}}}(2\omega)\cdot\hat{\mathbf{e}}_3}\left(e^{i\Delta kL} - 1\right). \qquad (C.12)$$

Since we have no input at the second harmonic frequency, $\mathcal{E}_{3,\perp}(0,t,\tau) = 0$ and $\mathcal{E}_{3,\parallel}(0,t,\tau) = 0$. At the output of the autocorrelators we measure a detector output proportional to the average intensity (irradiance) of the second harmonic signal while varying τ. First let us calculate the intensity as a function of time t and delay τ by averaging over an optical cycle. The envelopes are nearly constant over the integration leading to a time dependent intensity

$$I_3(L,t,\tau) = 2c\epsilon_0 n_3^{2\omega}\left|\mathcal{E}_3(L,t,\tau)\right|^2 \qquad (C.13)$$

$$= 2c\epsilon_0 n_3^{2\omega}\left\{\frac{\mu_0^2(2\omega)^4}{4k_{3,z}^2(\Delta k)^2}\left|\mathcal{P}_{3,\perp}^{(2)}(\mathbf{r},t,\tau)\right|^2 + \frac{\left|\mathcal{P}_{3,\parallel}^{(2)}(\mathbf{r},t,\tau)\right|^2}{\left(\overline{\overline{\epsilon_{\parallel}}}(2\omega)\cdot\hat{\mathbf{e}}_3\right)^2}\right\}4\sin^2\left[\frac{\Delta kL}{2}\right] \qquad (C.14)$$

If we are near the phase matching condition of $\Delta k \approx 0$ then the transverse component dominates. We then have

$$I_3(L,t,\tau) = \frac{2\epsilon_0 d_{eff}^2(2\omega)^2}{cn_3^{2\omega}\cos^2\theta}\left|\mathcal{E}_1(\mathbf{r},t)\right|^2\left|\mathcal{E}_2(\mathbf{r},t-\tau)\right|^2 L^2\text{sinc}^2\left[\frac{\Delta kL}{2\pi}\right] \qquad (C.15)$$

where we have defined $d_{eff} \equiv (1/2)\epsilon_0\hat{\mathbf{e}}_3 \cdot \overline{\overline{\chi}}^{(2)}(-2\omega,\omega,\omega) : \hat{\mathbf{e}}_1\hat{\mathbf{e}}_2$ in conformance with the usual convention.

---

[3]Although we have not proved it here, $\Delta\mathbf{k}$ is in the $\hat{z}$ direction. See Reference [46].

Writing this in terms of input intensities, which does not depend on our definition of the pulse envelope, we have

$$I_3(L, t, \tau) = \frac{d_{eff}^2 (2\omega)^2}{\epsilon_0 c^3 n_1^\omega n_2^\omega n_3^{2\omega} \cos^2 \theta} I_1(\mathbf{r}, t) I_2(\mathbf{r}, t - \tau) L^2 \mathrm{sinc}^2 \left[\frac{\Delta k L}{2\pi} \right]. \qquad (C.16)$$

What do these mathematical results show so far? We see that the maximum second harmonic generation efficiency decreases as we stray from the phase matching condition $\Delta k = 0$, and have learned functionally how phase mismatch decreases efficiency in the limit of small Δk. We see that this "sum" type of second harmonic generation depends on the overlap of the two pulse trains in space and time. When we measure the output of our autocorrelators, we are integrating over times long compared to the pulse duration, giving measurements proportional to pulse fluence which can be calculated as (assuming phase matching and suppressing spatial dependence)

$$\mathcal{F}_3^{2\omega}(\tau) = \int_{-\infty}^{\infty} dt' I_3(L, t', \tau) = \frac{d_{eff}^2 (2\omega)^2 L^2}{\epsilon_0 c^3 n_1^\omega n_2^\omega n_3^{2\omega} \cos^2 \theta} \int_{-\infty}^{\infty} dt' I_1(t') I_2(t' - \tau) \qquad (C.17)$$

which is proportional to the first order intensity autocorrelation of the pulse.

APPENDIX D

DIFFRACTION AND ABERRATION LIMITED SPOT SIZES

In this appendix, we examine the theoretical limits to the cross-sectional area of our light beams on the sample so that we may gain some assurance that our measurements are reasonable and as a basis for possible improvements. We make estimates of the diffraction limit, chromatic aberration, and spherical aberration. As for the monochromatic aberrations, spherical aberration is likely the most important one as long as we remain near the center of the lens.[1]

If we consider the beams to be point sources, we can estimate the diffraction limited spot size by the first zero of the point spread function, the Airy disk diameter $D = 2.44\lambda f/\#$. Estimating a 2 mm diameter input beam, a 20 cm focal length lens, and a $\lambda = 800$ nm wavelength, we get an effective $f/\#$ of 100 and a spot diameter of about 200 μm.

For (perhaps) a better estimate, we can use Gaussian beam theory. We can estimate the diffraction angle as $\theta \approx w(z)/z = 1$ mm/20 cm $= 5$ mrad. The beam waist (radius) is $w_0 = \lambda/(\pi\theta) = 50$ μm. The beam waist is defined as the smallest radius at which the intensity has fallen by a factor of $1/e^2$, so it is (conceptually) comparable to the zero of the Airy disk previously considered, although giving a smaller diameter of about 100 μm. This is to be expected since collimation was not considered in the previous estimate.

Now we will consider the blur induced by the chromatic aberration. When considering chirp in Section B we saw that the chromaticity was the cause of the chirp as well as the chromatic aberration. In fact, in the limit that the effect is large,

---

[1]The other four Seidel aberrations, coma, astigmatism, field curvature, and distortion are off-axis aberrations [57, pp. 540–544].

it can be shown that the fractional increase in both is identical up to constants of order unity for Gaussian beams [49, pp. 61–62]. We will not show this, but merely note that the affect of the aberration should be small. We begin by calculating from equation B.15 the change in the focal length of a thin lens with repect to wavelength

$$-\frac{1}{f^2}\frac{df}{d\lambda} = \frac{1}{f(n-1)}\frac{dn}{d\lambda} \tag{D.1}$$

$$\Delta f \approx -\frac{f}{(n-1)}\frac{dn}{d\lambda}\Delta\lambda \tag{D.2}$$

Using values appropriate for our focusing lenses, $f = 20$ cm, $n = 1.5$, $dn/d\lambda = -2.0 \times 10^{-2}$ μm^{-1}, and $\Delta\lambda = 8$ nm, results in $\Delta f = 64$ μm. This is much less than the Rayleigh range of our (assumed) Gaussian beam, $z_0 = \pi w_0^2/\lambda \sim 10$ mm, so we can conclude that the chromatic aberration only slightly spatially broadens the beam. We can estimate the broadening through Gaussian beam theory [2] which relates the beam radius to the beam waist:

$$\frac{w(z)}{w_0} = \sqrt{1 + \frac{z^2}{z_0^2}}. \tag{D.3}$$

In this expression, $w(z)$ is the beam radius, w_0 is the beam waist, z is the distance from the waist, and z_0 is the Rayleigh range, where the radius has increased by a factor of $\sqrt{2}$ and the spreading can begin to be described by the divergence angle θ. For the chromatically aberrated focus, the beam waist can be estimated to be no less than the Gaussian beam radius at half the spread in focus (see Figure D.1):

$$\frac{w(z)_{min}}{w_0} \approx \frac{w(\Delta f/2)}{w_0} = \sqrt{1 + \frac{(\Delta f/2)^2}{z_0^2}} \tag{D.4}$$

$$= \sqrt{1 + \frac{(32 \ \mu\text{m})^2}{(10 \ \text{mm})^2}} \tag{D.5}$$

$$\approx 1 + 5 \times 10^{-6},$$

which is utterly negligable.

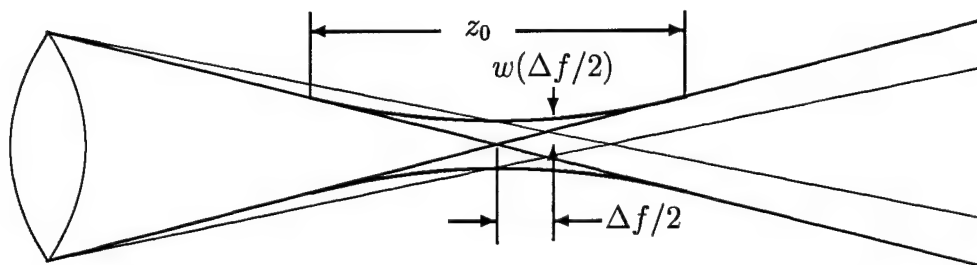[2] See, for example, Reference [2, pp. 484–490].

Figure D.1: The geometry of chromatic aberration. Dispersion in the glass of the lens causes a longitudinal spread in focus. The minimum transverse spread occurs midway between the extreme focal planes. For a Gaussian beam, the beam radius at $\Delta f/2$ is a good estimate of the smallest achievable radius.

So we can ignore chromatic aberration, but what about achromatic aberration? Born and Wolf [39, pp. 203–232] develop a theory of aberrations that is too involved to detail here. They apply the theory to the spherical aberration of a thin lens, and we use their results for a symmetric thin lens of 15 cm focal length, object at negative infinity, and image at the focal point. We again get negligable aberration, this time on the order of 0.6 μm.[3]

From these estimates, it is clear that we do not gain by getting better lenses, but would add chirp by adding glass. The spot diameters we obtain are close to the estimated diffraction limits.

---

[3]Calculations are made from Reference [39], equation 5.6.14 (U) with parameters $\beta = 0$ (bending parameter), $n = 1.5$ (refractive index), $\mathcal{P} = (1/15)$ cm^{-1} (lens power), $\mathcal{K} = (-1/30)$ cm^{-1} (Abbe invariant), and $\sigma = 0$ (related to relative surface curvatures). The aberration must be scaled using equation 5.2.8, $D_1 = 15$ cm (image distance), $n_1 = 1$ (index of air), and $\lambda_1 = 1$ (length scaling factor).

APPENDIX E

LASERS AND AMPLIFIERS

This appendix contains useful information about the lasers and amplifiers in our system. It is not meant to replace the system manuals, but contains more detail on the commercial systems than included in the text, and especially gives operating tips for users that we have discovered while using the system. The information given in Section 5.1.1, which is primarily about system concepts, is generally not repeated here. The last three appendices included in this dissertation are not integral to understanding the experiments, but are included primarily for those that will follow in the laboratory.

E.1 Millenia V cw Nd:YVO$_4$ laser

The Millenia V is a continuous wave, diode pumped, frequency doubled, neodymium yttrium vanadate (Nd : YVO$_4$) laser used solely to pump the Ti:Sapphire laser. There is very little user interface and almost no adjustments that can be made. In addition to the laser head, there is a power supply, chiller (shared with the Ti:Sapphire laser and regenerative amplifier), and control module, as shown in Figure E.1.

A Nd : YVO$_4$ laser is the same as a Nd : YAG or Nd : YLF laser except for the matrix which holds the active medium of Nd^{+3} ions. There are several possible lasing transitions, but the Millenia is set up for the most common, which is a 1064 nm transition in a four level scheme. A portion of the beam is doubled within the cavity by a temperature tuned LBO crystal; although it is possible to adjust the temperature, it is not recommended, and we have had no reason to consider doing so. The cw 532 nm output is TEM$_{00}$ and adjustable up to 5.00 W, but we have always operated at 4.20 W.
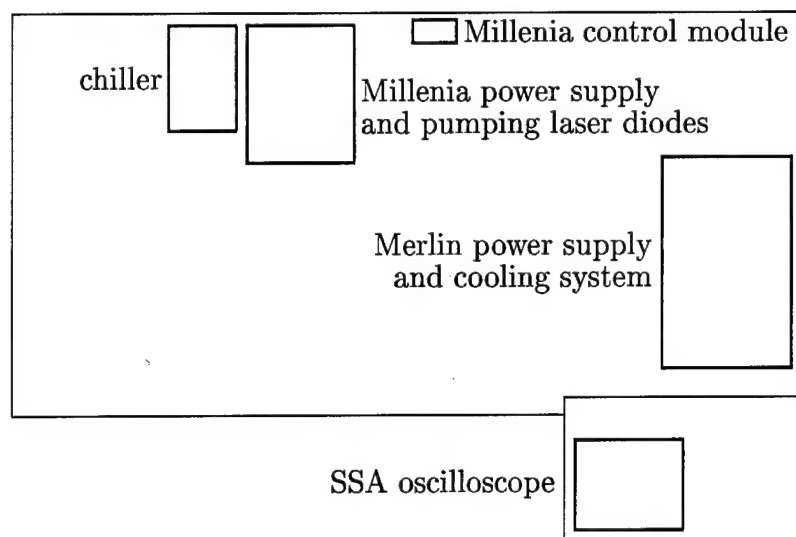
Figure E.1: Laser and amplifier components kept under the optical table. The Millenia control module is actually on the table. The chiller services the Millenia, Tsunami, and Spitfire. Laser diode light is piped through optical fiber bundles to the Millenia. The Merlin cooling system exchanges heat in a closed deionized water loop with externally supplied chilled water.

The first step in operating the entire laser/amplifier system is to turn on the chiller and warm up the diodes that pump the Millenia. The diodes are on two diode bars inside the power supply, and coupled into the laser cavity through nonadjustable optical fiber bundles. If the Millenia power supply is left on, the diodes take about four minutes to warm up. From a cold start, the process takes about 30 minutes according to the manual, but we have not turned off the power supply since it was installed. The temperature stabilization of the laser diode bars is initiated by pushing the power button on the control module. An LCD panel on the control module displays a message that the diodes are ready, and the user must hold the power button for several seconds to initiate lasing. As a precaution against putting cw light into the Spitfire, we recommend putting the power meter in position to measure the Tsunami ouput before starting the Millenia.

The chiller uses distilled (not deionized) water. The water level should be monitored at least weekly and refilled as needed, maybe once a month. It cools the

Millenia first, and then the Tsunami Ti:Sapphire laser, and then the Ti:Sapphire crystal in the Spitfire regenerative amplifier, all in a single loop.

E.2 Tsunami Ti:Sapphire laser

The Tsunami is pumped by the Millenia and actively mode-locked by an acousto-optic modulator (AOM). Other than the chiller described above and the mode-locker, there are no ancillary components. However, we do use an autocorrelator to measure the pulse width. The autocorrelator should always be used to ensure the Tsunami is mode-locking before putting the beam into the Spitfire, since cw input can damage the regenerative amplifier when its Ti:Sapphire crystal is being pumped.

Our use of the Tsunami is greatly simplified by the fact that we always use it at 800 nm wavelength and about 10–12 nm bandwidth. Usually it is only necessary to adjust the last steering mirrors from the Millenia to optimize Tsunami cw output power and then to switch on the mode-locker. The cw power should be 450–500 mW, and the mode-locked average power will be about 420–470 mW. The Tsunami is only a seed for the regenerative amplifier, so the amplified output is nearly independent of the input power for a wide range of inputs; we have seen little change in amplified power down to around 200 mW Tsunami output. The Tsunami seems to be more stable, however, if operating near its peak power for a given pump.

It may be necessary from time to time to adjust the input and output coupling mirrors to maximize the output power. The horizontal position is adjusted by the green knobs (green for grass) and the vertical position is adjusted with the blue knobs (blue for sky). Over time, these adjustments can walk the beam away from its optimum position. If fewer of the "photodiode" LEDs light up on the mode-locking box than previously, the beam position has changed. The Tsunami manual explains how to walk the beam back to a maximum power output (pages 7-3 through 7-4) if it becomes necessary.

The pulse wavelength and bandwidth are tuned with two tall knobs and a screw near the center of the Tsunami laser head. The knob nearest the edge of the table

shifts a slit inbetween the central group velocity dispersion (GVD) compensation prisms (see Figure E.2) which selects a band of wavelengths. The width of the slit (and the laser bandwidth) is controlled with a screw that requires the removal of the laser cover. The far knob shifts the GVD prisms to include more or less glass in the laser cavity to minimize GVD. Two points to keep in mind when adjusting bandwidth: (1) in making the spectrum wider and the pulse shorter, at some point one gets cw breakthrough characterized by a narrow line in the autocorrelation spectrum—keep away from this or risk damaging the amplifier, (2) the useable bandwidth is limited by the large gold mirror in the regenerative amplifier—it is a good guide as to the optimum bandwidth.
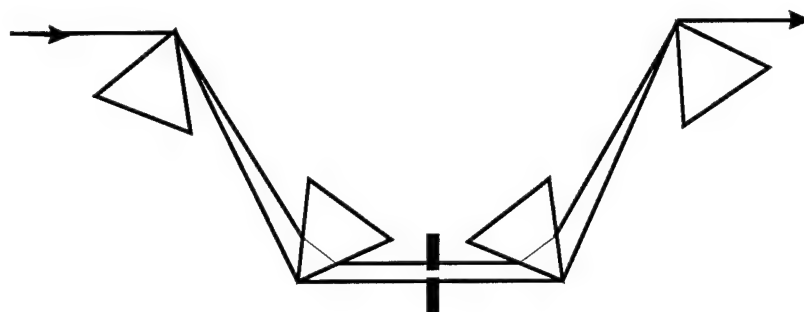
Figure E.2: Tsunami wavelength and bandwidth selection. The spectrum of the laser cavity is dispersed by the GVD compensation prisms. A slit in the middle of the prisms determines the central wavelength and bandwidth of the laser. The prisms can be moved in and out of the cavity beam to optimize GVD compensation.

E.3 Merlin Nd : YLF laser

One should turn on the external cooling water and the Merlin power supply (Figure E.1) just after turning on the Millenia/Tsunami/Spitfire chiller. If this becomes a habit, it is less likely that one will forget the external cooling water. The Merlin power supply includes a closed cooling system that uses distilled (not deionized) water. This water is cooled by the external cooling water by means of a heat exchanger, afterwhich it passes through a particle filter and deionizing filter. These filters should be changed quarterly by the book, but together they cost about $500.

A window on the back of the power supply shows the internal water level, which must be kept above the minimum water level mark. The object of all this cooling is the laser head and Q-switch of the Merlin. Turning on the Merlin power supply the same time as starting the chiller gives time for the deionization filter to reach an equilibrium before starting the Merlin.

The Merlin itself is a frequency doubled, 1 kHz Q-switched, neodymium-doped yttrium lithium fluoride (Nd : LiYF$_4$ or Nd : YLF) laser. It is optically pumped by a krypton arc lamp at one focus of an elliptic reflector with the gain medium at the other. The arc lamps last from 300 to 600 hours; the power supply counts the hours whenever it is turned on. The power to the arc lamp is controlled by a remote control box on the shelf above the laser (see Figure E.3). A new arc lamp uses about 3.3 to 3.4 kW of electrical power, which is indicated on the control box. The useful life of the arc lamp can be stretched by increasing its electrical power when the Merlin output starts to drop. When the arc lamp is changed or the Merlin is not operating satisfactorily, the end mirrors should be tweaked, for which the cover must be removed.

The Merlin is intracavity doubled to 526 nm to pump the Ti:Sapphire rod in the Spitfire. The frequency doubling is done in a temperature tuned LBO crystal. Whenever the arc lamp is changed, the output beam quality is poor, or the output power is low, the LBO should be temperature tuned in a range of about $\pm 1°$ C to get the best beam quality (a circular profile).

E.4   Spitfire regenerative amplifier

As a World War II historian would tell you, the Merlin is the engine of the Spitfire. The average power of the amplified Tsunami seed when it exits the Spitfire is determined almost entirely by the gain in the amplifier cavity. The Spitfire has a pulse stretcher and a pulse compressor in addition to the regenerative amplifier cavity. These affect the pulse duration, but not the power.

When the regenerative amplifier is being aligned, the amplifier cavity is made to operate like a laser. The procedure, which is described in the manual, essentially
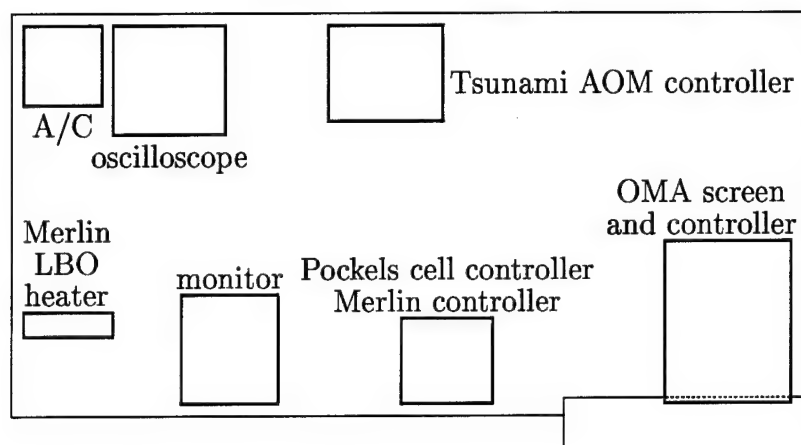
Figure E.3: Laser and amplifier components kept above the optical table. A/C stands for the power supply and signal generator used with the autocorrelator. The oscilloscope and monitor read out the autocorrelator and the Spitfire photodiode. The LBO (doubling crystal) heater is controlled with a device on the Merlin case. The Pockels cell controller, also called the SDG, controls the timing of the Pockels cells. The Merlin controller controls the flashlamp and Q-switch.

maximizes the laser output to optimize the cavity. If the cavity ever gets misaligned enough to stop lasing, it can be roughly aligned with either a He-Ne laser or the Tsunami input. It is generally a good idea, however, not to touch the amplifier cavity except in the lasing mode while it is being pumped by the Merlin. Then it should never become severly misaligned. The Merlin beam quality and focus (mode matching) are crucial to good amplified power.

The key difference between a laser and a regenerative amplifier is that the amplifier has two Pockels cells and a quarter-wave plate to switch a seed pulse in and out. The quarter-wave plate rotates the polarization of the seed after two passes so that it is is reflected out of the cavity by a polarizing beamsplitter. The cavity is made to operate as a laser by deactivating the Pockels cells and removing the quarter-wave plate. The polarizing beamsplitter passes light that has the polarization of the Merlin light, so the beamsplitter does nothing in the lasing configuration. Behind one of the cavity mirrors is a photodiode which we use to optimize the lasing by using light that leaks through.

When the half-wave plate is replaced, the cavity cannot lase. The amplifier traps a single seed pulse by applying a voltage to the first Pockels cell just after the seed passes. This Pockels cell acts as a quarter-wave plate, negating the effect of the original quarter-wave plate for the pulses that follow. The trapped pulse has been rotated from vertical to horizontal polarization while those that follow it emerge with the original vertical polarization. These unwanted vertically polarized pulses are ejected by the beamsplitter while the trapped pulse is repeatedly amplified by the Ti:Sapphire rod. The photodiode that was used to optimize lasing now monitors the pulse energy buildup.

After about 14 passes, a quarter-wave voltage is applied to the other Pockels cell so that the amplified pulse is ejected by the polarizing beamsplitter. The timing of this is controlled with a "synchronization and delay generator" (SDG). It is generally best to time the second Pockels cell to eject the pulse one pass after the photodiode shows the gain to be saturated. The power output of the unseeded amplifier should be about 1.3 to 1.5 W, which will be about the same as the seeded power output.

Little should be done to the regenerative amplifier on a daily basis. It is best not to touch the cavity mirrors unless maximizing the output in the laser configuration. It is sometimes useful to tweak the last Merlin beam input mirror.

What is usually done daily is to align the Tsunami seed through the apertures in the stretcher, and to tweak up the first and last seed input mirrors to get maximum gain for early pulses. One should not pump the regenerative amplifier with the last stretcher aperture in place since it cuts off some of the seed spectrum. A check to make before activating the Pockels cells ("output enable" switch) is that the red "sync error" light is not on, as it will be if the Tsunami is not mode-locked. It is also advisable to look at the stretcher grating and gold mirror through the I.R. viewer to see that the spectrum is dispersed as it should be.

Infrequently, it may be necessary to adjust the Pockel cell voltages, to align the Pockels cells, to adjust the stretcher and compressor, or to realign the Ti:Sapphire rod. The Ti:Sapphire rod can be burned and/or pitted if the amplifier operates with an unstretched seed. The optics should be cleaned occasionally. The gold mirror

and gratings will likely be ruined if you try to clean them.

E.5 Optical parametric amplifiers

Once the OPAs are aligned for a given wavelength, they can usually be tweaked up using the input mirrors. If this can bring the OPA up to the operating power of the previous day, then it is ready to go. If not, first optimally compress the Spitfire output using the single shot autocorrelator (SSA) as a diagnostic and ensure the white light (continuum) generation is good. If a major realignment is needed, follow the procedure provided by Spectra Physics.

The OPAs divide the input pulse train into three paths: continuum generation, pre-amplifier, and power-amplifier (see Figure E.4). The continuum is adjusted first and determines the path of both amplifier passes through the BBO crystal in which the optical parametric amplification occurs. A bluish white disk with a red ring is the optimal appearance of the continuum spot. The continuum generation is sensitive to the pulse duration and is the best diagnostic for the Spitfire.
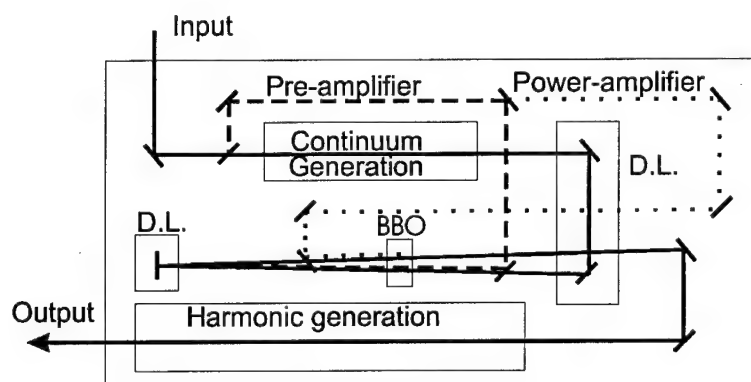
Figure E.4: A simplified diagram of the optical parametric amplifiers (OPA) showing the three pulse trains (continuum, pre-amplifier, and power-amplifier). BBO represents the $\chi^{(2)}$ crystal in which the optical parametric amplification occurs. D.L. stands for the delay lines to overlap the pulse trains.

Once the continuum path is aligned, the pre-amplifier path is overlapped with the continuum path along the entire overlap region and through the BBO crystal. The continuum path is adjusted with a delay line until both the continuum pulses

and the pre-amplifier pulses overlap and generate optical parametric amplification. The delay line was aligned at the factory and should not be touched! If it becomes necessary to adjust the pre-amplifier telescope, be very careful as it the focused beam can burn the optics or BBO crystal. A focus that is too tight can also create undesirable optical parametric generation (OPG) without the continuum pulses present. If the power output of the OPA is low, however, it may be necessary to adjust the telescope. Be careful: it is very sensitive.

The same procedure is followed for the power-amplifier and the same comments apply about adjusting the telescope. The methods for overlapping the amplifier beams with the continuum beam require blocking and unblocking beams to determine the overlap. This can be tricky to do without accidently blocking the continuum beam path on the pre-amplifier leg. The combined signal and idler output before the final line of optics is generally the best place to measure and optimize the output power until it is at least 60 mW or so. The power obtainable from each of these outputs varies with wavelength and can be roughly determined using the chart from Spectra Physics. We have usually had the most output power with the white light focussed near the power-amplifier delay line.

The wavelength is changed by rotating the BBO crystal. This is fairly easy to do if one follows the wavelength change on the OMA. When the intensity begins to get low, the time delays should be readjusted and the second harmonic generation should be tweaked up (if used). If it is necessary to switch from signal to idler or vice versa, or if doubling elements must be added, then it is better to add the elements first, get a good signal, and then shift the wavelength.

APPENDIX F

OPTICAL DELAYS AND ATTENUATION OF NEUTRAL DENSITY FILTERS

This appendix gives data on the neutral density filters available in Room 215 of the Optical Sciences Center. The information is of value primarily to those that need to use the Room 215 filters in time resolved measurements. The graphs enable a user to estimate the accuracy of the delay measurements, which is around 100 fs. The measurement techniques are fairly standard in ultrafast time-resolved spectroscopy, but are explained here for the uninitiated.

The optical delays were measured using cross-correlation techniques based on sum frequency generation as described in Subsection 5.3.2. First the sum frequency signal of the two pulses was measured without filters (Figure F.1). The resonance of this signal with respect to relative pulse delay shows which delay line position corresponds to maximum pulse overlap. Then the n.d. filter is added and the measurement is repeated. The additional delay is that which is due to the filter. For these measurements, the pulse wavelengths were around 825 nm and 835 nm repectively, and the wavelength associated with the sum-frequency was around 415 nm. For a given filter, the delay varies with wavelength due to dispersion, so the values contained here are only useful for near infrared radiation.

The transmission measurements were made by Jason Auxier on a Cary spectrophotometer. In this instrument, a thermal light source is filtered with a monochromator, which is scanned through a user designated range of wavelengths. The light is detected by one or more photodiodes, each detector used within its range of effectiveness. The transmission values agree with independent photodiode measurements made with 860 nm wavelength OPA pulses.
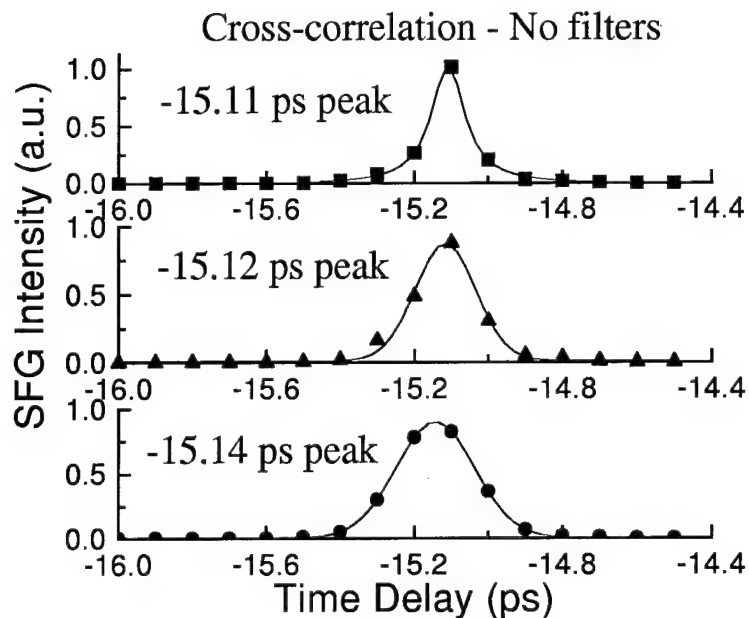
Figure F.1: Three trials showing the zero point of the relative pulse delay. This is the reference for the delays of all the filters that follow. The solid lines are curve fits done to determine the peaks. The symbols correspond to actual data.
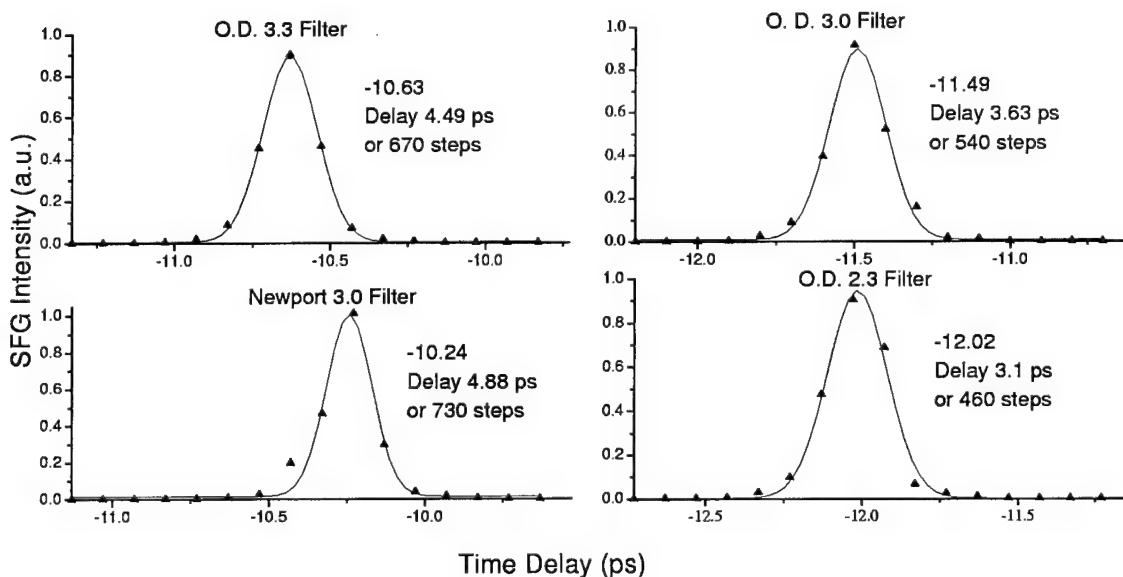

Figure F.2: Filter Delays. The Newport filters are labeled as such. The other filters in the lab are labeled O.D. Peaks are determined by Gaussian fits to the data. "Steps" refers to the Klinger delay line.
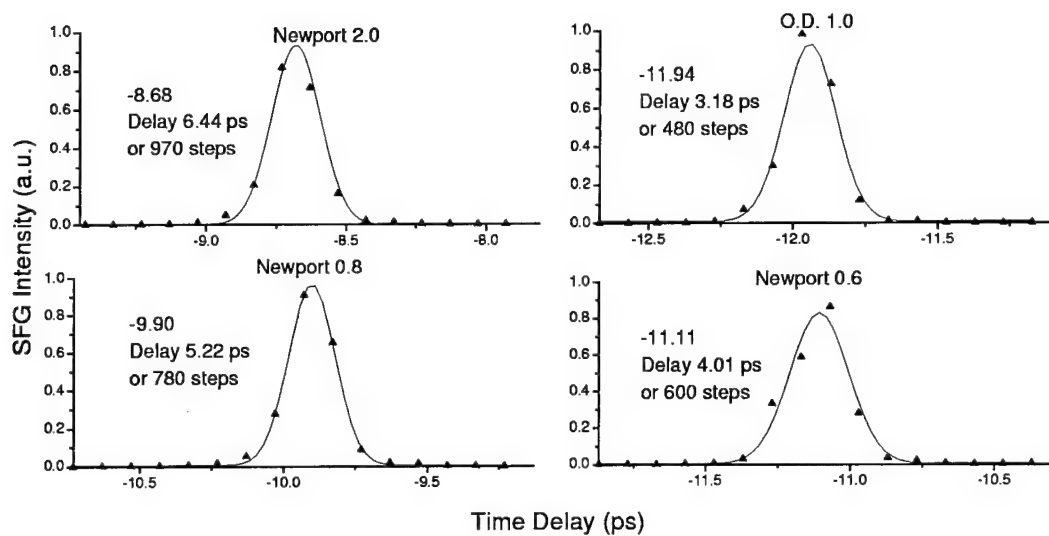
Figure F.3: More optical density filters. See Figure F.2 for notes.
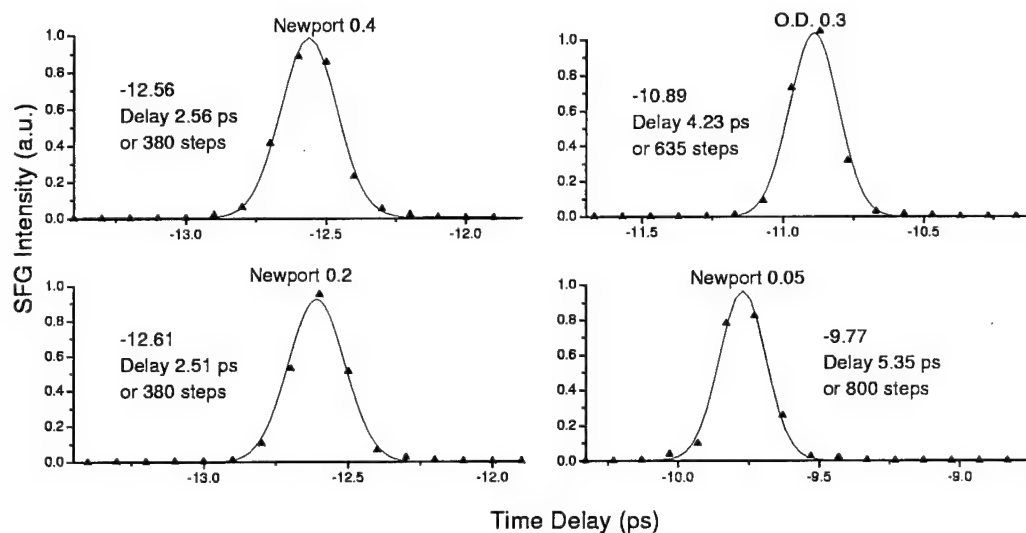
Figure F.4: More optical density filters. See Figure F.2 for notes.
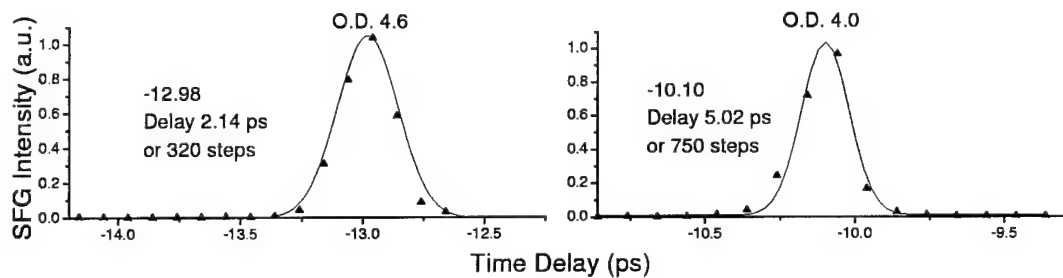
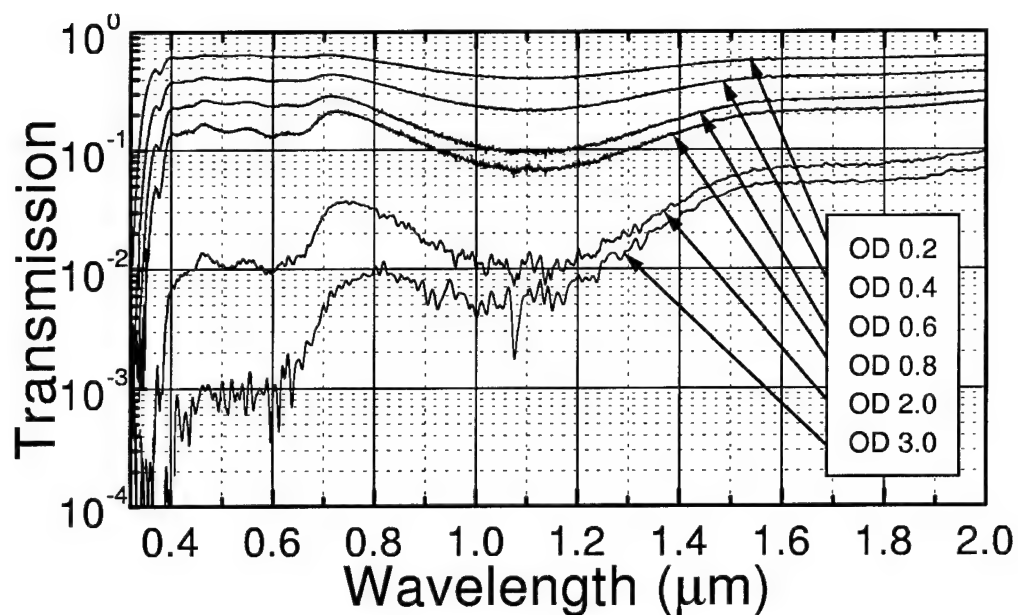Figure F.5: More optical density filters. See Figure F.2 for notes.

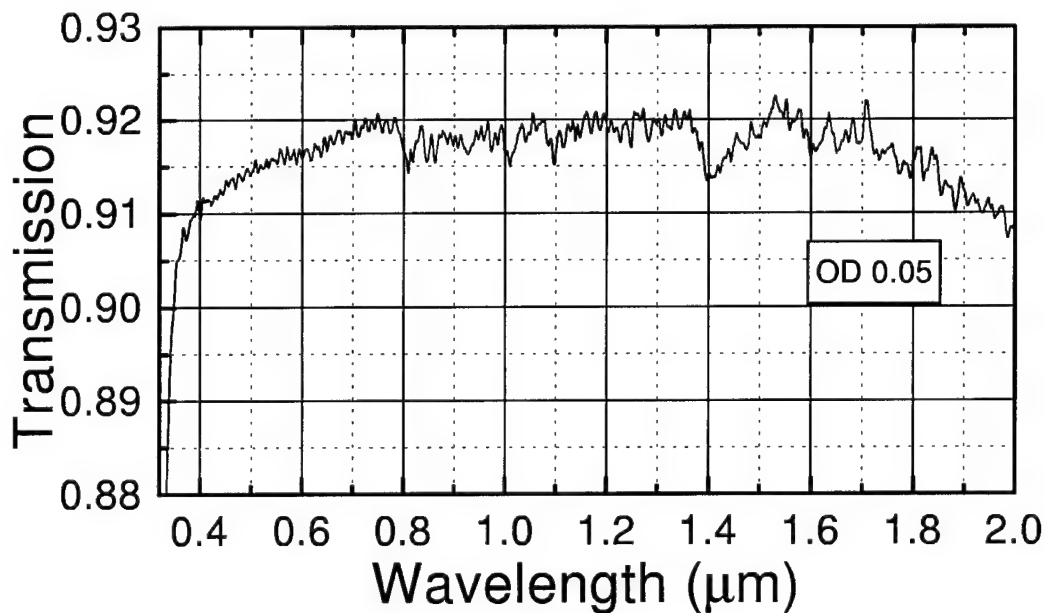Figure F.6: Transmission of the Newport filters as measured by J. Auxier.

Figure F.7: Transmission of the Newport 0.05 filters.

APPENDIX G

PULSE SHAPER MASK CHARACTERISTICS

Figures G.1 through G.6 give the shaped pulse spectra and cross-correlations for the various masks used in our experiments. The relative pulse intensities scale as the values shown, although the units are arbitrary.
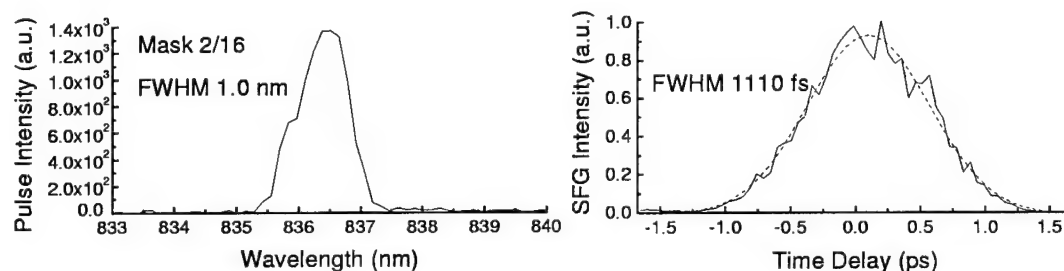

Figure G.1: Time and frequency domain properties of the pump pulse while using Mask 2/16 in the pulse shaper. The time domain figure is a cross-correlation with a 150 fs probe pulse. We therefore estimate the cross-correlation width to be about 150 fs wider than the pump-pulse duration. The dashed line is a gaussian fit to the cross-correlation to get an accurate width. The time-bandwidth product is calculated to be 0.41 as compared to 0.44 for the bandwidth limited gaussian pulse.
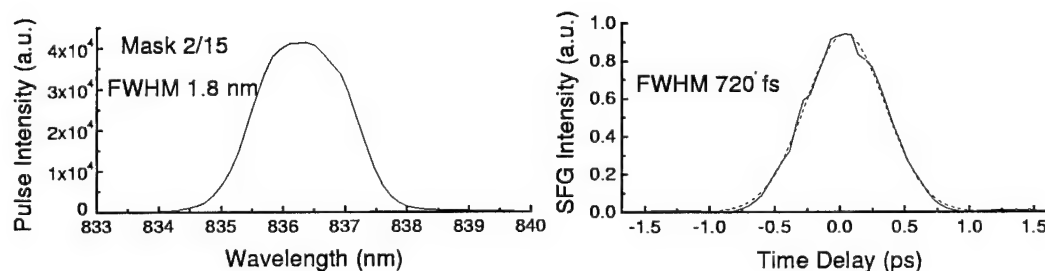

Figure G.2: Properties for Mask 2/15. The same comments apply as for Figure G.1. The time-bandwidth product is 0.55.
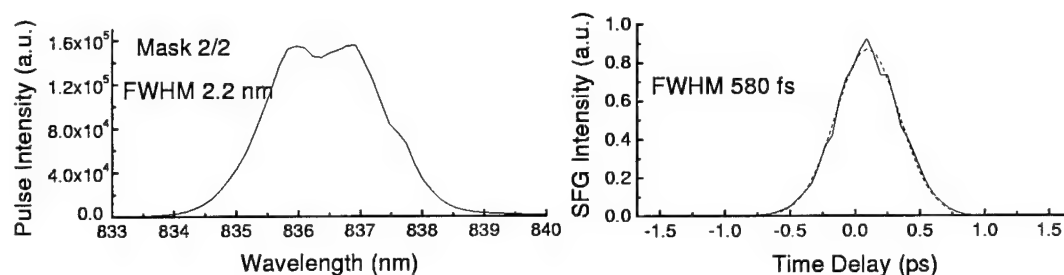
Figure G.3: Properties for Mask 2/2. The same comments apply as for Figure G.1, although the estimate of a 150 fs difference between the cross-correlation width and pulse duration is not as good. A deconvolution is necessary for a more accurate result. With our estimates, the time-bandwidth product is 0.41.
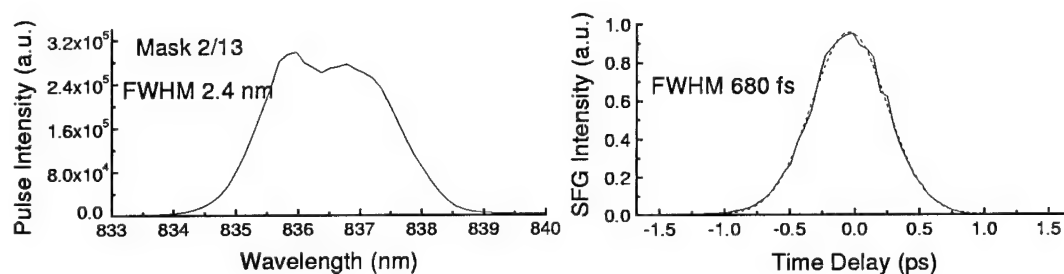

Figure G.4: Properties for Mask 2/13. The same comments apply as to Figure G.3. The time-bandwidth product is 0.55.
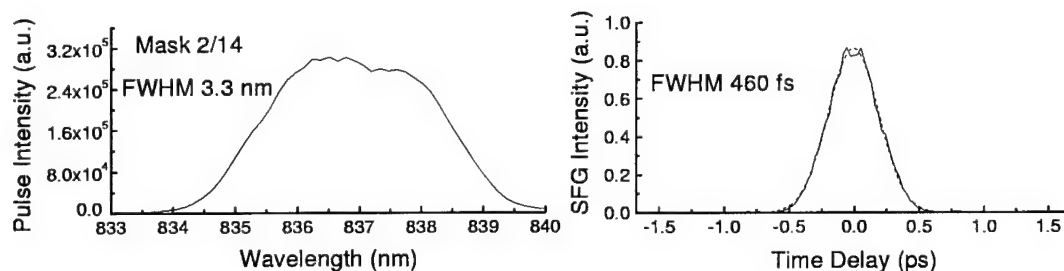

Figure G.5: Properties for Mask 2/14. The same comments apply as to Figure G.3. The time-bandwidth product is 0.44.
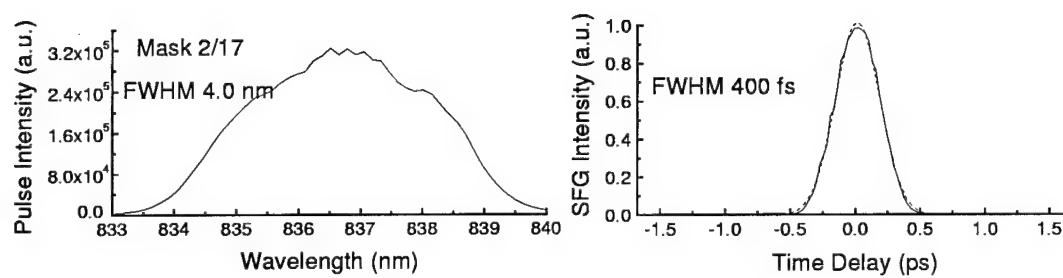
Figure G.6: Properties for Mask 2/17. The same comments apply as to Figure G.3. The time-bandwidth product is 0.43.

REFERENCES

[1] Murray Sargent III, Marlan O. Scully, and Willis E. Lamb, Jr. *Laser Physics.* Addison-Wesley, Redwood City, California, 1974.

[2] Peter W. Milonni and Joseph H. Eberly. *Lasers.* John Wiley & Sons, New York, 1988.

[3] Hans C. Ohanian. *Principles of Quantum Mechanics.* Prentice Hall, Englewood Cliffs, New Jersey, 1990.

[4] Nasser Peyghambarian, Stephan W. Koch, and Andre Mysyrowicz. *Introduction to Semiconductor Optics.* Prentice Hall, Englewood Cliffs, New Jersey, 1993.

[5] B. Sapoval and C. Hermann. *Physics of Semiconductors.* Springer-Verlag, New York, 1995.

[6] Neil W. Ashcroft and N. David Mermin. *Solid State Physics.* Saunders College Publishing, Harcourt Brace, Fort Worth, 1976.

[7] Hartmut Haug and Stephan W. Koch. *Quantum Theory of the Optical and Electronic Properties of Semiconductors.* World Scientific, Singapore, third edition, 1994.

[8] I. I. Rabi. Space quantization in a gyrating magnetic field. *Physical Review*, 51:652–654, 1937.

[9] I. I. Rabi, S. Millman, P. Kusch, and J. R. Zacharias. The molecular beam resonance method for measuring nuclear magnetic moments: The magnetic moments of $_3\text{Li}^6$, $_3\text{Li}^7$, and $_9\text{F}^{19}$. *Physical Review*, 55:526–535, 1939.

[10] Marlan O. Scully and M. Suhail Zubairy. *Quantum Optics.* Cambridge University Press, Cambridge, 1997.

[11] J. H. Eberly, M. L. Pons, and H. R. Haq. Dressed field pulses in an absorbing medium. *Physical Review Letters*, 72(1):56–59, 1994.

[12] E. Arimondo and G. Orriols. Nonabsorbing atomic coherences by coherent two-photon transitions in a three-level optical pumping. *Lettere Al Nuovo Cimento*, 17(10):333–338, 1976.

[13] R. M. Whitley and C. R. Stroud, Jr. Double optical resonance. *Physical Review A*, 14(4):1498–1513, 1976.

[14] B. W. Shore. *The Theory of Coherent Atomic Excitation.* Wiley, New York, 1990. pp. 824–837.

[15] S. E. Harris, J. E. Field, and A. Imamoğlu. Nonlinear optical processes using electromagnetically induced transparency. *Physical Review Letters*, 64(10):1107–1110, 1990.

[16] S. E. Harris. Lasers without inversion: Interference of lifetime-broadened resonances. *Physical Review Letters*, 62(9):1033–1036, 1989.

[17] Marlan O. Scully, Shi-Yao Zhu, and Athanasios Gavrielides. Degenerate quantum-beat laser: Lasing without inversion and inversion without lasing. *Physical Review Letters*, 62(24):2813–2816, 1989.

[18] Marlan O. Scully. Enhancement of the index of refraction via quantum coherence. *Physical Review Letters*, 67(14):1855–1858, 1991.

[19] J. J. Sakurai. *Modern Quantum Mechanics.* Addison-Wesley, Redwood City, California, 1985.

[20] Richard P. Feynman, Robert B. Leighton, and Matthew Sands. *The Feynman Lectures on Physics*, volume III. Addison-Wesley, Reading, Massachusetts, 1965.

[21] L. Allen and J. H. Eberly. *Optical Resonance and Two-Level Atoms.* Dover, New York, 1987.

[22] Raymond A. Serway. *Physics for Scientists and Engineers.* Saunders College Publishing, Philadelphia, second edition, 1990.

[23] R. Binder and S. W. Koch. Nonequilibrium semiconductor dynamics. *Progress in Quantum Electronics*, 19:307–460, 1995.

[24] Claude Cohen-Tannoudji, Jacques Dupont-Roc, and Gilbert Grynberg. *Photons and Atoms: Introduction to Quantum Electrodynamics.* John Wiley & Sons, New York, second edition, 1989.

[25] R. P. Feynman, F. L. Vernon, Jr., and R. W. Hellwarth. Geometrical representation for maser problems. *Journal of Applied Physics*, 28:49–52, 1957.

[26] I. I. Rabi, N. Ramsey, and J. Schwinger. *Review of Modern Physics*, 26:167, 1954.

[27] Herbert Goldstein. *Classical Mechanics.* Addison-Wesley, Reading, Massachusetts, second edition, 1980.

[28] Alan Corney. *Atomic and Laser Spectroscopy.* Clarendon Press, Oxford, 1977.

[29] M. Lindberg and S. W. Koch. Effective Bloch equations for semiconductors. *Physical Review B*, 38:3342, 1988.

[30] R. Binder, D. Scott, A. E. Paul, M. Lindberg, K. Henneberger, and S. W. Koch. Carrier-carrier scattering and optical dephasing in highly excited semiconductors. *Physical Review B*, 45:1107, 1992.

[31] C. F. Klingshirn. *Semiconductor Optics.* Springer-Verlag, Berlin, 1997.

[32] W. E. van der Veer, R. J. J. van Diest, A. Dönszelmann, and H. B. van Linden van den Heuvell. Experimental demonstration of light amplification without population inversion. *Physical Review Letters*, 70(21):3243–3246, 1993.

[33] Jacques I. Pankove. *Optical Processes in Semiconductors.* Dover, New York, 1971.

[34] Pierre Meystre and Murray Sargent III. *Elements of Quantum Optics.* Springer, Berlin, third edition, 1999.

[35] M. Lindberg and R. Binder. Dark states in coherent semiconductor spectroscopy. *Physical Review Letters*, 75(7):1403–1406, 1995.

[36] Robert W. Boyd. *Nonlinear Optics.* Academic Press, San Diego, 1992.

[37] K. B. Ferrio and D. G. Steel. Raman quantum beats of interaction excitons. *Physical Review Letters*, 80(4):786–789, 1998.

[38] R. Binder, M. Lindberg, A. Schülzgen, M. E. Donovan, K. Wundke, H. M. Gibbs, G. Khitrova, and N. Peyghambarian. Many-body aspects of excitonic Rabi oscillations in semiconductors. In P. Blood, A. Ishibashi, and M. Osinski, editors, *Physics and Simulation of Optoelectronic Devices VII*, Proceedings of the SPIE 3625, 1999. (invited paper), Photonics West, San Jose, January 23–29, 1999.

[39] Max Born and Emil Wolf. *Principles of Optics: Electromagnetic Theory of Propagation Interference and Diffraction of Light.* Pergamon Press, Oxford, sixth edition, 1980.

[40] D. Frölich, A. Nöthe, and K. Reimann. Observation of the resonant optical Stark effect in a semiconductor. *Physical Review Letters*, 55(12):1335–1337, 1985.

[41] C. Fürst, A. Leitenstorfer, A. Nutsch, G. Tränkle, and A. Zrenner. Ultrafast Rabi oscillations of free-carrier transitions in InP. *physica status solidi (b)*, 204(20):20–22, 1997.

[42] Eugene Hecht. *Optics*. Addison-Wesley, Reading, Massachusetts, second edition, 1987.

[43] John P. McKelvey. *Solid State and Semiconductor Physics*. Robert E. Krieger Publishing, Malabar, Florida, 1966.

[44] A. V. Kavokin et al. Quantum wells with zero valence-band offset: Drastic enhancement of forbidden excitonic transitions. *Physical Review B*, 54(16):R 11 078–R11 081, 1996.

[45] Amnon Yariv. *Quantum Electronics*. John Wiley & Sons, New York, third edition, 1989.

[46] Y. R. Shen. *The Principles of Nonlinear Optics*. John Wiley & Sons, New York, 1984.

[47] Orazio Svelto. *Principles of Lasers*. Plenum Press, New York, second edition, 1989.

[48] William T. Silfvast. *Laser Fundamentals*. Cambridge University, Cambridge, 1996.

[49] Jean-Claude Diels and Wolfgang Rudolph. *Ultrashort Laser Pulse Phenomena: Fundamentals, Techniques, and Applications on a Femtosecond Time Scale*. Academic Press, San Diego, 1996.

[50] Robert R. Alfano, editor. *The Supercontinuum Laser Source*. Springer-Verlag, New York, 1989.

[51] Harald W. Giessen. *Ultrafast Carrier and Gain Dynamics in Strongly Confined Semiconductor Quantum Dots*. dissertation, University of Arizona, 1995.

[52] J. Jansky, G. Corradi, and R. N. Gyuzalian. On a possibility of analyzing the temporal characteristics of short light pulses. *Optics Communications*, 23:293–298, 1977.

[53] F. Salin, P. Georges, G. Roger, and A. Brun. Single-shot measurement of a 52-fs pulse. *Applied Optics*, 26:4528–4531, 1987.

[54] C. Rempel and W. Rudolph. Single shot autocorrelator for femtosecond pulses. *Experimentell Technik der Physik*, 37:381–385, 1989.

[55] K. W. DeLong, Rick Trebino, and Daniel J. Kane. Comparison of ultrashort-pulse frequency-resolved-optical-gating traces for three common beam geometries. *Journal of the Optical Society of America B*, 11(9):1595–1608, 1994.

[56] D. J. Kane and R. Trebino. Characterization of arbitrary femtosecond pulses using frequency-resolved optical gating. *IEEE Journal of Quantum Electronics*, 29:571–579, 1993.

[57] Jack D. Gaskill. *Linear Systems, Fourier Transforms, and Optics*. John Wiley & Sons, New York, 1978.

[58] S. T. Cundiff, A. Knorr, J. Feldmann, S. W. Koch, E. O. Göbel, and H. Nickel. Optically induced excitation density flops in semiconductors. *physica status solidi (b)*, 188(1):307–319, 1995.

[59] S. T. Cundiff, A. Knorr, J. Feldmann, S. W. Koch, E. O. Göbel, and H. Nickel. Rabi flopping in semiconductors. *Physical Review Letters*, 73(8):1178–1181, 1995.

[60] H. Giessen, A. Knorr, S. Haas, S. W. Koch, S. Linden, J. Kuhl, M. Hetterich, M. Grün, and C. Klingshirn. Self-induced transmission on a free exciton resonance in a semiconductor. *Physical Review Letters*, 81(19):4260–4263, 1998.

[61] A. Schülzgen, R. Binder, M. E. Donovan, M. Lindberg, K. Wundke, H. M. Gibbs, G. Khitrova, and N. Peyghambarian. Direct observation of excitonic Rabi oscillations in semiconductors. *Physical Review Letters*, 82(11):2346–2349, 1999.

[62] M. E. Donovan, A. Schülzgen, K. Wundke, R. Binder, M. Lindberg, H. M. Gibbs, G. Khitrova, and N. Peyghambarian. Experimental observation of multiple excitonic optical Rabi oscillations in a semiconductor. In K. T. Tsen, editor, *Ultrafast Phenomena in Semiconductors III*, Proceedings of the SPIE 3624, 1999. (invited paper), Photonics West, San Jose, January 23–29, 1999.

[63] A. Schülzgen, R. Binder, M. Donovan, M. Lindberg, K. Wundke, H. Gibbs, G. Khitrova, and N. Peyghambarian. Laser induced Rabi oscillations in semiconductors. In *IIV Quantum Electronics and Laser Science Conference*, 1999 OSA Technical Digest Series, Washington, D.C., 1999. Optical Society of America. (invited paper), IIV Quantum Electronics and Laser Science Conference, Baltimore, May 23–28, 1999.

[64] I. I. Rabi, S. Millman, P. Kusch, and J. R. Zacharias. A new method of measuring nuclear magnetic moment. *Physical Review*, 53:318, 1938.

[65] I. I. Rabi, S. Millman, P. Kusch, and J. R. Zacharias. The magnetic moments of $_3Li^6$, $_3Li^7$, and $_9F^{19}$. *Physical Review*, 53:495, 1939.

[66] Richard P. Feynman, Robert B. Leighton, and Matthew Sands. *The Feynman Lectures on Physics*, volume II. Addison-Wesley, Reading, Massachusetts, 1965.

[67] C. L. Tang and H. Statz. Optical analog of the transient nutation effect. *Applied Physics Letters*, 10:145–147, 1968.

[68] G. B. Hocker and C. L. Tang. Observation of the transient nutation effect. *Physical Review Letters*, 21:591–594, 1969.

[69] R. G. Brewer and R. L. Shoemaker. Photon echo and optical nutation in molecules. *Physical Review Letters*, 27:631–634, 1971.

[70] H. M. Gibbs. Incoherent resonance fluorescense for a Rb atomic beam excited by a short coherent optical pulse. *Physical Review A*, 8:446, 1973.

[71] S. Schmitt-Rink, D. S. Chemla, and H. Haug. Nonequilibrium theory of the optical Stark effect and spectral hole burning in semiconductors. *Physical Review B*, 37:941, 1988.

[72] I. Balslev, R. Zimmermann, and A. Stahl. Two-band density-matrix approach to nonlinear optics of excitons. *Physical Review B*, 40:4095, 1989.

[73] Personal discussion with H. M. Gibbs and C. Ell.

[74] R. Binder, S. W. Koch, M. Lindberg, N. Peyghambarian, and W. Schäfer. Ultrafast adiabatic following in semiconductors. *Physical Review Letters*, 65(7):899–902, 1990.

[75] D. Frölich, R. Willie, W. Schlapp, and G. Weimann. Optical quantum-confined Stark effect in GaAs quantum wells. *Physical Review Letters*, 59(15):1748–1751, 1987.

[76] A. Mysyrowicz, D. Hulin, A. Antonetti, A. Migus, W. T. Masselink, and H. Morkoç. "Dressed excitons" in a multiple-quantum-well structure: Evidence for an optical Stark effect with femtosecond response time. *Physical Review Letters*, 56(25):2748–2751, 1986.

[77] A. Von Lehmen, J. E. Zucker, J. P. Heritage, and D. S. Chemla. Optical Stark effect on excitons in GaAs quantum wells. *Optics Letters*, 11(10):609–612, 1986.

[78] S. G. Lee, P. A. Harten, J. P. Sokoloff, R. Jin, B. Fluegel, K. E. Meissner, C. L. Chuang, R. Binder, S. W. Koch, G. Khitrova, H. M. Gibbs, N. Peyghambarian, J. N. Polky, and G. A. Pubanz. Femtosecond excitonic bleaching recovery in the optical Stark effect of GaAs/Al$_x$Ga$_{1-x}$As multiple quantum wells and directional couplers. *Physical Review B*, 43(2):1719–1725, 1991.

[79] N. Peyghambarian, S. W. Koch, M. Lindberg, B. Fluegel, and M. Joffre. Dynamic Stark effect of exciton and continuum states in CdS. *Physical Review Letters*, 62(10):1185–1188, 1989.

[80] Sérgio Tsuda and Carlos H. Brito Cruz. Femtosecond dynamics of the optical Stark effect in semiconductor-doped glass. *Applied Physics Letters*, 68(8):1093–1095, 1996.

[81] B. Fluegel, N. Peyghambarian, G. Olbright, M. Lindberg, S. W. Koch, M. Joffre, D. Hulin, A. Migus, and A. Antonetti. Femtosecond studies of coherent transients in semiconductors. *Physical Review Letters*, 59(22):2588–2591, 1987.

[82] M. Joffre, D. Hulin, A. Migus, A. Antonetti, C. Benoit à la Guillaume, N. Peyghambarian, M. Lindberg, and S. W. Koch. Coherent effects in pump-probe spectroscopy of excitons. *Optics Letters*, 13(4):276–278, 1988.

[83] S. Schmitt-Rink and D. S. Chemla. Collective excitations and the dynamical Stark effect in a coherently driven exciton system. *Physical Review Letters*, 57(21):2752–2755, 1986.

[84] M. Lindberg and S. W. Koch. Transient oscillations and dynamic Stark effect in semiconductors. *Physical Review B*, 38(11):7607–7614, 1988.

[85] S. Schmitt-Rink, D. S. Chemla, and H. Haug. Nonequilibrium theory of the optical Stark effect and spectral hole burning in semiconductors. *Physical Review B*, 37(2):941–955, 1988.

[86] M. Combescot and R. Combescot. Excitonic Stark shift: A coupling to "semivirtual" biexcitons. *Physical Review Letters*, 61(1):117–120, 1988.

[87] W. H. Knox, D. S. Chemla, D. A. B. Miller, J. B. Stark, and S. Schmitt-Rink. Femtosecond ac Stark effect in semiconductor quantum wells: Extreme low- and high-intensity limits. *Physical Review Letters*, 62(10):1189–1192, 1989.

[88] M. Joffre, D. Hulin, A. Migus, and M. Combescot. Laser-inducted exciton splitting. *Physical Review Letters*, 62(1):74–77, 1989.

[89] C. Ell, J. F. Müller, K. El Sayed, and H. Haug. Influence of many-body interactions on the excitonic optical Stark effect. *Physical Review Letters*, 62(3):304–307, 1989.

[90] R. Binder, S. W. Koch, M. Lindberg, W. Schäfer, and F. Jahnke. Transient many-body effects in the semiconductor optical Stark effect: A numerical study. *Physical Review B*, 43(8):6520–6529, 1991.

[91] M. Combescot and R. Combescot. Optical Stark effect of the exciton: Biexcitonic origin of the shift. *Physical Review B*, 40(6):3788–3801, 1989.

[92] D. Hulin and M. Joffre. Excitonic optical Stark redshift: The biexciton signature. *Physical Review Letters*, 65(27):3425–3428, 1990.

[93] C. Sieh, T. Meier, F. Jahnke, A. Knorr, S. W. Koch, P. Brick, M. Hübner, C. Ell, J. Prineas, G. Khitrova, and H. M. Gibbs. Coulomb memory signatures in the excitonic optical Stark effect. *Physical Review Letters*, 82(15):3112–3115, 1999.

[94] T. Meier, S. W. Koch, P. Brick, C. Ell, G. Khitrova, and H. M. Gibbs. Signatures of correlations in intensity-dependent excitonic absorption changes. *Physical Review B*, 62(7):4218–4221, 2000.

[95] M. E. Donovan, A. Schülzgen, J. Lee, R. Binder, and N. Peyghambarian. Coherently coupled optical Stark shifts in a semiconductor three-state system. Submitted for publication to *Physical Review B*, October 2000.

[96] Dong S. Lee and Kevin J. Malloy. Gain without inversion in interband transitions of semiconductor quantum wells from a single-particle perspective. *Physical Review B*, 53(23):15749–15755, 1996.

[97] R. Binder and M. Lindberg. Three-band excitonic Rabi oscillations in semiconductor quantum wells. *Physical Review B*, 61(4):2830–2836, 2000.

[98] W. E. Bell and A. L. Bloom. Observation of forbidden resonances in optically driven systems. *Physical Review Letters*, 6:623, 1961.

[99] G. Alzetta, L. Moi, and G. Orriols. Nonabsorbtion hyperfine resonances in a sodium vapor irradiated by a multimode dye laser. *Nuovo Cimento B*, 52:209–218, 1979.

[100] H. R. Gray, R. M. Whitley, and C. R. Stroud, Jr. Coherent trapping of atomic populations. *Optics Letters*, 3(6):218–220, 1978.

[101] K.-J. Boller, A. Imamoğlu, and S. E. Harris. Observation of electromagnetically induced transparency. *Physical Review Letters*, 66(20):2593–2596, 1991.

[102] A. Nottelmann, C. Peters, and W. Lange. Inversionless amplification of picosecond pulses due to Zeeman coherence. *Physical Review Letters*, 70(12):1783–1786, 1993.

[103] J. B. Stark, W. H. Knox, and D. S. Chemla. Spin-resolved femtosecond magnetoexciton interactions in GaAs quantum wells. *Physical Review B*, 46(12):7919–7922, 1992.

[104] George B. Arfken and Hans J. Weber. *Mathematical Methods for Physicists*. Academic Press, San Diego, fourth edition, 1995.

[105] David J. Griffiths. *Introduction to Electrodynamics*. Prentice Hall, Englewood Cliffs, New Jersey, second edition, 1989.

[106] Jing-yuan Zhang, Jung Y. Huang, and Y. R. Shen. *Optical Parametric Generation and Amplification*. Laser Science and Technology. Harwood Academic, Luxembourg, 1995.

[107] Angus Macleod. Optics of thin films class notes. Optical Sciences Center (U. of Arizona) and Thin Films Center, Inc., 1997.

[108] A. M. Weiner, J. G. Fujimoto, and E. P. Ippen. Femtosecond time-resolved reflectometry measurements of multiple-layer dielectric mirrors. *Optics Letters*, 10:71–73, 1985.